MARKUS AICHHORN

Ordering Phenomena in Strongly-Correlated Systems:

Cluster Perturbation Theory Approaches

DISSERTATION

zur Erlangung des Doktorgrades der technischen Wissenschaften

TUG
Technische Universität Graz
Erzherzog-Johann-Universität

Begutachter:

O.Univ.-Prof. Dr. Wolfgang von der Linden
Institut für Theoretische Physik - Computational Physics
Technische Universität Graz

Priv.-Doz. Dr. Michael Potthoff
Institut für Theoretische Physik und Astrophysik
Universität Würzburg

September 2004

for Julia

Abstract

In this thesis we apply the variational cluster perturbation theory (V-CPT) for the investigation of ordering phenomena in strongly-correlated systems. For this purpose, we first introduce the V-CPT, which is an extension of the cluster perturbation theory (CPT), that allows to study symmetry-broken phases. The connection of this very flexible cluster approach to the cellular dynamical mean-field theory is discussed.

After a brief glimpse on finite-temperature applications of CPT and V-CPT we investigate the long-range antiferromagnetic ground state of the two-dimensional Hubbard model. Different to CPT, the V-CPT is able to give a correct description of the low-energy magnetic super-exchange driven features of spectral functions.

For the application to extended long-range Hubbard models, a modification of the V-CPT is necessary. We show that a consistent cluster approach can be constructed by a mean-field decoupling of inter-cluster interaction bonds. For the one-dimensional model we find good agreement with results obtained by other methods. For the two-dimensional case, where other numerical methods fail, our calculations suggest a first-order phase transition for onsite interaction $U \geq 3t$. In addition we calculate the spectral function, which deviates significantly from the Hartree-Fock prediction, especially in the spin-density-wave phase.

Moreover we apply the developed methods to the compound $\mathrm{NaV_2O_5}$, a quarter-filled ladder system. We investigate the influence of lattice degrees of freedom by exact diagonalisation and V-CPT, and show that they have a strong impact on the charge-ordering transition. Spin and charge suszeptibilities do rather depend on the value of the order parameter and not on the driving force of the transition. The dependence of the single-particle spectral function is much more pronounced, and by comparing to infrared measurements one can conclude, that the coupling to the lattice must not be neglected. Within V-CPT it is possible to study the effect of inter-ladder couplings, and the calculated spectral functions along and perpendicular to the ladder direction agrees very well with experimental results.

Kurzfassung

In dieser Arbeit werden Ordnungsphänomene in stark korrelierten Vielteilchensystemen im Rahmen der variationellen Cluster-Störungstheorie (V-CPT) untersucht. Diese Theorie stellt eine Erweiterung der konventienellen Cluster-Störungstheorie dar, die es auch erlaubt, symmetriegebrochene Zustände zu beschreiben.

Nach einem kurzen Exkurs zu Anwendungen auf endliche Temperaturen untersuchen wir die langreichweitige antiferromagentische Ordnung im zweidimensionalen Hubbardmodell. Die V-CPT ist in der Lage, die niederenergetischen Eigenschaften der Spektralfunktion, die durch den magnetischen Superaustausch verursacht werden, korrekt zu beschreiben.

Um die Methode auf das erweiterten Hubbardmodell anwenden und Ladungsordnungen studieren zu können, konstruieren wir durch eine Molekularfeldnäherung eine konsistente Clustermethode. Für das eindimensionale Modell finden wir gute Übereinstimmung mit Ergebnissen anderer Methoden. Für den zweidimensionalen Fall, wo andere Methoden versagen, zeigt unsere Methode einen Übergang erster Ordnung. Zusätzlich können wir die Spektralfunktion berechnen, die wesentlich von der Hartree-Fock Vorhersage abweicht.

Wir wenden die Methoden auch auf das viertelgefüllte Leitersystem Natriumvanadat an. Wir zeigen, dass Gitterfreiheitsgrade eine starke Auswirkung auf den Ladungsordnungsübergang haben. Spin- und Ladungs-Suszeptibilitäten hängen vor allem von der Größe des Ordnungsparameters ab, während die Einteilchen-Spektraldichte auch von der treibenden Kraft des Phasenübergangs abhängt. Die berechneten Spektren parallel und normal zu den Leiterrichtungen stimmen sehr gut mit experimentellen Daten überein.

Contents

List of Figures

1. Introduction

Many strongly-correlated systems are at the forefront of experimental and theoretical research in condensed matter physics because of their fascinating properties. The spectrum reaches from one-dimensional conductors, quasi two-dimensional cuprates exhibiting high temperature superconductivity, to three dimensional heavy fermion materials such as uranium compounds. Other interesting classes of strongly-correlated materials are the manganites with its very rich phase diagram, or the vanadates with their intriguing low-dimensional properties.

The *cuprate family* of strongly-correlated systems has seen intense research for the last twenty years, following the discovery of high-temperature superconductivity. These studies have been able to bring clarity to some of the unusual features in, e.g., photo-emission spectra and spin response. Yet many questions, most of all the nature of the pairing mechanism and, thus, the microscopic foundation for the high transition temperatures are not answered in a satisfactory way. Hence, there is need for further theoretical investigations that take into account, e.g., longer-range Coulomb repulsion at sufficiently low temperatures.

A particularly interesting class of compounds widely investigated at present, experimentally and theoretically, is represented by the *low-dimensional vanadates*, where the active spins are located at the vanadium sites. They can be realized in a variety of crystal structures having quite different magnetic and electronic properties. The vanadium-based low-dimensional compounds are a class of systems which demonstrate coupling of charge, spin, and lattice degrees of freedom, and nevertheless can be described with relatively simple theoretical models. However, despite of their simplicity, solutions of these models are not available, especially for realistic parameters. For this reason the investigation of these compounds within basic solid state physics models and comparison with the results to experiment presents a problem of fundamental scientific interest and a challenge for solid state theorists and experimentalists.

Experimentally, a wealth of information has been obtained on strongly-correlated systems by powerful techniques including angle-resolved photo-emission spectroscopy (ARPES), inverse photo-emission, Raman scattering, Neutron scattering, and electron-energy loss spectroscopy (EELS).

On the theoretical side, strongly-correlated materials are described by simplified theoretical models that in general contain an interaction term of the same order of magnitude as the kinetic energy or even larger. This interplay of kinetic and interaction

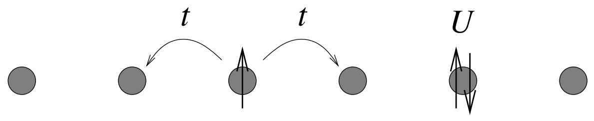

Figure 1.1.: Schematic representation of the one-dimensional Hubbard model. The gray circles denote the lattice sites, up and down arrows indicate electrons with up and down spin, respectively.

energy may give rise to rich phase diagrams with several different competing types of short-range correlations and with different symmetry-broken phases, such as long-range magnetic ordering, charge ordering, superconducting phases, and many others.

One of the most simple models that can be constructed under these assumptions is the tight-binding Hubbard model. It consists of a kinetic energy part, where the electrons can only hop between nearest-neighbor sites, and the Coulomb interaction U which acts only locally on every site. A schematic representation of this one-band tight-binding Hubbard model is shown in Fig. 1.1. The system gains energy t by the hopping of the electrons between neighboring sites, and double occupied sites are punished with an energy cost of U. Although this model looks quite simple, an exact analytic solution is only known for the one-dimensional case by the Bethe ansatz [1].

There are some general problems that one has to face when treating models for strongly-correlated systems. First of all the finding of analytic solutions is very difficult, since in general the kinetic part of the Hamiltonian is an operator diagonal in momentum space, whereas the interacting part is diagonal in real space. Moreover for the interesting case where the Coulomb interaction U is of the same order of magnitude as the bandwidth W, the conventional perturbative approach must fail. This is expected for weak-coupling perturbation theory as well as for the complementary approach with exact treatment of the interaction part and perturbative treatment of the kinetic energy. For this reason the application of numerical methods for the investigation of strongly-correlated system has attracted more and more attention in recent years.

In this thesis we use the so-called *Variational Cluster Perturbation Theory* [2] in order to study ordering phenomena in strongly-correlated systems that arise due to the interplay of kinetic and interaction energy. Simply speaking, this method combines the exact treatment of short-range correlations on a finite length scale with long-range ordering on a mean-field level.

In chapter 2 we first introduce the cluster perturbation theory (CPT) of Sénéchal *et al.* [3, 4]. It provides an approximation for the single-particle Green's function in the thermodynamic limit by coupling clusters of finite size within strong-coupling perturbation theory. But since it does not involve any self-consistent procedure it can *not* account for true long-range order patterns, different to, e.g., the dynamical mean-field theory. Nevertheless it is very powerful for the calculation of spectral properties of homogeneous systems, and the advantages compared to calculations based on the exact diagonalisation of systems of finite sizes is shown in detail in chapter 2.

The shortcoming of CPT concerning symmetry-broken phases can be overcome by a recently proposed extension of CPT, the variational CPT (V-CPT). As said above, it does not only include short-range correlations like CPT, but in addition long-range effects are incorporated.The main difference to the standard CPT is that the single-particle parameters of the finite-size clusters are not taken to be fixed, but are determined by a general variational principle. This can be achieved by putting the (V-)CPT into a wider framework of cluster approaches, based on the self-energy-functional approach (SFA) [5, 6]. We will show in chapter 2 that this V-CPT is indeed superior to CPT, and it allows for a very flexible construction of thermodynamically consistent cluster approaches.

The second part of chapter 2 is subject to numerical exact diagonalisation methods, since they are needed for the cluster approaches presented in this thesis. After a detailed discussion of the ground-state Lanczos algorithm, we also introduce two finite-temperature methods. To be specific we will show that a combination of the finite-temperature Lanczos method (FTLM) [7] and the recently proposed low-temperature Lanczos method (LTLM) [8] allows to calculate static and dynamical properties in the whole temperature range with reasonable numerical effort. These algorithms are then used in chapter 3 for the investigation of the spectral function of the Hubbard model at finite temperatures.

In chapter 4 we investigate the long-range antiferromagnetic phase of the two-dimensional Hubbard model at zero temperature. For this purpose we introduce an fictitious symmetry-breaking field as variational parameter in V-CPT, and the optimal strength of this field is determined by the general variational principle. We will show that the V-CPT gives a long-range antiferromagnetic solution for the 2D system, but not for 1D, where the system has a paramagnetic ground state. In addition we will compare our results with some other previous studies in order to determine the quality of the V-CPT approximations.

Chapter 5 deals with the application of the V-CPT method to models with non-local interactions. After a short derivation of the necessary modifications of the V-CPT for the investigation of such models, we study the charge-ordering transition in the 1D and 2D extended Hubbard model at zero temperature as function of the nearest-neighbor repulsion. Although many results are known for the 1D model, V-CPT allowed for the first time to calculate the spectral function of this system for both the charge-ordered and charge-disordered phase. Different to other numerical methods, the application of V-CPT to the 2D model is straightforward.

After chapter 4 and 5, where we have investigated model Hamiltonians for strongly-correlated systems, we apply the developed methods to the compound NaV_2O_5 in chapter 6. To be specific, we study the effects of the lattice degrees of freedom on the charge-ordering transition that occurs in this quarter-filled ladder system by means of exact diagonalisation and V-CPT. We will show that this coupling has a significant effect on both static and dynamical quantities such as charge order parameter, charge and spin susceptibilities, or the single-particle spectral function. Whereas exact diagonalisation is only used for the investigation of single ladders, we study the implications of the inter-ladder coupling on the spectral function by V-CPT. We will show that the numerical results agree very well with experimental data.

At the end of this thesis we sum up the main results in chapter 7.

2. Methods

In recent years many numerical methods have been suggested and gradually improved for the investigation of strongly-correlated electron systems, such as quantum Monte Carlo (QMC) [9], exact diagonalisation (ED), and density-matrix renormalization-group (DMRG) [10, 11]. They are able to give essentially exact results – at least for limited system sizes or (DMRG) for the one dimensional case. Another non-perturbative approach is the mean-field method and, in the context of the Hubbard model, the dynamical mean field theory (DMFT) [12], in particular. While DMFT directly works in the thermodynamic limit of infinite system size and is exact in the case of infinite dimension, it must be regarded as a strong approximation for low-dimensional systems since spatial correlations are neglected altogether. Cluster generalizations of DMFT include at least short-range correlations via the exact treatment of a small cluster instead of considering a single impurity only. Both, a reciprocal-space (dynamical cluster approximation, DCA [13]) and a real-space construction (cellular dynamical mean field theory, C-DMFT [14–16]) have been suggested. These approaches improve results for $D = 1, 2, 3$, but they are no longer exact in the $D = \infty$ limit.

Essentially the same idea is followed with the cluster perturbation theory (CPT) [3, 4, 17], which is a cluster extension of the strong-coupling expansion for the Hubbard model. It has been successfully used to describe spectral properties of the high-T_c materials [18–21]. Moreover an extension of the original CPT, the variational CPT, is presented, which allows to put the CPT in the context of a wider class of cluster approaches. With this generalization the investigation of symmetry-broken phases is possible, contrary to the original CPT.

2.1. Cluster Perturbation Theory

The CPT is a technique for calculating the single-particle Green's function of strongly-correlated electron systems. It takes into account short-range correlations on the length scale of the cluster, and correlations beyond the cluster size are neglected. By coupling of the clusters within strong-coupling perturbation theory[1] at leading order, the Green's function in the thermodynamic limit is recovered. In the following this theory is discussed in detail.

---

[1] For the strong-coupling perturbation theory see App. A

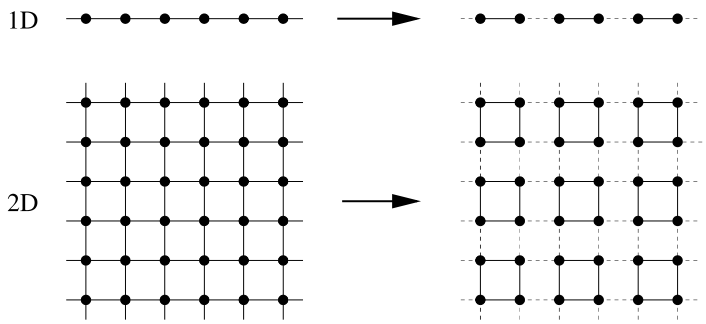

Figure 2.1.: Dividing the lattice into clusters of finite size in one dimension (top) and two dimensions (bottom). The solid lines indicate intra-cluster bonds treated exactly, and the dashed lines are inter-cluster bonds.

2.1.1. Basic ideas

The basic steps of CPT can be summed up in the following way:

(i) Divide the original lattice into disconnected clusters of finite size.

(ii) Calculate the Green's function on such a finite cluster.

(iii) Recover the Green's function of the original lattice problem by treating the hopping between clusters in strong-coupling perturbation theory.

A possible division of the lattice into clusters of finite size, step (i), is shown in Fig. 2.1. For one dimension, the division is straightforward, and several possible clusters differ only in the number of sites within the cluster. In two dimensions the situation is more complicated, because not only the number of sites, but also the shape of the cluster can be chosen arbitrarily. In Fig. 2.1 only the simplest tiling with 2 × 2 clusters is shown, but in general many other tilings including more sites are possible. It seems quite natural that open boundary conditions (obc) are advantageous for the clusters, but CPT cannot provide a proof for the advantage of this choice over, e.g., periodic boundary conditions. We will see later in Sec. 2.2.3 that this question of boundary conditions can be answered in a unique way by the variational CPT.

After division of the lattice the Hamiltonian can be written as

$$H = \sum_{\boldsymbol{R}} \left[H_0^{(\mathrm{c})}(\boldsymbol{R}) + H_1(\boldsymbol{R}) \right] + \sum_{\boldsymbol{R},\boldsymbol{R}'} H_0^{(\mathrm{i})}(\boldsymbol{R},\boldsymbol{R}'), \tag{2.1}$$

where $\boldsymbol{R}$ denotes the individual clusters, $H_0^{(\mathrm{c})}(\boldsymbol{R})$ is the part of the single-particle term that acts only inside a single cluster, $H_1(\boldsymbol{R})$ is the interaction part inside the cluster, and the inter-cluster hopping is given by

$$H_0^{(\mathrm{i})}(\boldsymbol{R},\boldsymbol{R}') = \sum_{a,b} T_{a,b}^{\boldsymbol{R},\boldsymbol{R}'} c^\dagger_{\boldsymbol{R},a} c_{\boldsymbol{R}',b}, \tag{2.2}$$

where the hopping matrix $T_{a,b}^{\boldsymbol{R},\boldsymbol{R}'}$ is non-zero only for hopping processes across the cluster boundaries. The indices a and b are general quantum numbers within a cluster, e.g., position and spin index, and $c_{\boldsymbol{R},a}^{\dagger}$ creates an electron with quantum number a in cluster $\boldsymbol{R}$. Note that it is of crucial importance for the applicability of the method that the clusters are connected by one-particle operators only.

The quantity of interest is the single-particle Green's function

$$G_{\boldsymbol{R},a,\boldsymbol{R}',b}(\omega) = \langle\langle c_{\boldsymbol{R},a}; c_{\boldsymbol{R}',b}^{\dagger}\rangle\rangle_{\omega}.$$

By decoupling the clusters, i.e., neglecting the second sum in Eq. (2.1), we have

$$G_{\boldsymbol{R},a,\boldsymbol{R}',b}(\omega) = \delta_{\boldsymbol{R},\boldsymbol{R}'} G'_{\boldsymbol{R},a,b}(\omega),$$

which means that the Green's function is diagonal in the cluster indices, and $G'_{\boldsymbol{R},a,b}(\omega)$ is the cluster Green's function. According to step (ii) this property is evaluated by exact diagonalisation, which will be described in detail in Sec. 2.3.

The hopping between the clusters is then treated perturbatively. Using Eq. (2.2) as perturbation, the strong-coupling perturbation theory yields for the Green's function in lowest order, Eq. (A.6),

$$\boldsymbol{G}^{-1}(\omega) = \boldsymbol{G'}^{-1}(\omega) - \boldsymbol{T}, \tag{2.3}$$

where the bold symbols denote matrices with indices $(\boldsymbol{R}, a)$ and $(\boldsymbol{R}', b)$, respectively.

The above central expression of the CPT method can be derived in another non-perturbative way [17]: Recall that the self-energy $\boldsymbol{\Sigma}$ of a system is defined by Dyson's equation

$$\boldsymbol{G}^{-1}(\omega) = \boldsymbol{G}_0^{-1}(\omega) - \boldsymbol{\Sigma}(\omega), \tag{2.4}$$

where $\boldsymbol{G}_0(\omega)$ is the non-interacting Green's function ($U = 0$)

$$\boldsymbol{G}_0^{-1}(\omega) = \omega - \boldsymbol{t} = \omega - \boldsymbol{t}' - \boldsymbol{T}, \tag{2.5}$$

with $\boldsymbol{t}$ the hopping matrix of the infinite system, and $\boldsymbol{t}'$ the intra-cluster hopping matrix. Applying Dyson's equation to the exact cluster Green's function and using Eq. (2.5) gives

$$\boldsymbol{G'}^{-1}(\omega) = \omega - \boldsymbol{t}' - \boldsymbol{\Sigma}'(\omega) = \boldsymbol{G}_0^{-1}(\omega) + \boldsymbol{T} - \boldsymbol{\Sigma}'(\omega) \tag{2.6}$$

with the cluster self-energy $\boldsymbol{\Sigma}'(\omega)$. A substitution of $\boldsymbol{G}_0^{-1}(\omega)$ in Eq. (2.4) by Eq. (2.6) yields

$$\boldsymbol{G}^{-1}(\omega) = \boldsymbol{G'}^{-1}(\omega) - \boldsymbol{T} - (\boldsymbol{\Sigma}(\omega) - \boldsymbol{\Sigma}'(\omega)). \tag{2.7}$$

Above equation is equivalent to Eq. (2.3) if and only if $\boldsymbol{\Sigma}(\omega) = \boldsymbol{\Sigma}'(\omega)$. Thus the CPT formalism is equivalent to an approximation of the full self-energy by the self-energy of a finite cluster, and Eq. (2.3) can also be written as

$$\boldsymbol{G}^{-1}(\omega) = \boldsymbol{G}_0^{-1}(\omega) - \boldsymbol{\Sigma}'(\omega). \tag{2.8}$$

2.1.2. Restoring translational invariance

First of all it is obvious that the division into clusters breaks the translational symmetry of the lattice. However, translational invariance is preserved on a superlattice Γ produced by the clusters, with a reduced Brillouin zone BZ_Γ. Thus we can express the hopping matrix $T_{a,b}^{\boldsymbol{R},\boldsymbol{R}'}$ and the Green's function $G_{\boldsymbol{R},a,\boldsymbol{R}',b}(\omega)$, Eq. (2.3), in terms of a wave vector $\boldsymbol{k}$ belonging to BZ_Γ. For this purpose we start with the second term in Eq. (2.1), but write it in a different way

$$\begin{aligned}\mathcal{O} &= \sum_{\boldsymbol{R},\boldsymbol{R}'} H_0^{(\mathrm{i})}(\boldsymbol{R},\boldsymbol{R}') = \sum_{\boldsymbol{R},\boldsymbol{\Delta}} H_0^{(\mathrm{i})}(\boldsymbol{R},\boldsymbol{\Delta}) \\ &= \sum_{\boldsymbol{R},\boldsymbol{\Delta}} \sum_{a,b} T_{a,b}^{\boldsymbol{R},\boldsymbol{\Delta}} c_{\boldsymbol{R}+\boldsymbol{\Delta},a}^{\dagger} c_{\boldsymbol{R},b} = \sum_{\boldsymbol{R},\boldsymbol{\Delta}} \sum_{a,b} T_{a,b}(\boldsymbol{\Delta}) c_{\boldsymbol{R}+\boldsymbol{\Delta},a}^{\dagger} c_{\boldsymbol{R},b}.\end{aligned} \tag{2.9}$$

The last equation holds since the hopping matrix is translational invariant with respect to the superlattice Γ. The superlattice Fourier transformation is defined as

$$\begin{aligned} c_{\boldsymbol{R}+\boldsymbol{\Delta},a}^{\dagger} &= \frac{1}{\sqrt{L}} \sum_{\boldsymbol{k}} \mathrm{e}^{-\mathrm{i}\boldsymbol{k}(\boldsymbol{R}+\boldsymbol{\Delta})} c_{\boldsymbol{k},a}^{\dagger} \\ c_{\boldsymbol{R},b} &= \frac{1}{\sqrt{L}} \sum_{\boldsymbol{k}} \mathrm{e}^{\mathrm{i}\boldsymbol{k}\boldsymbol{R}} c_{\boldsymbol{k},b}, \end{aligned}$$

with L the number of clusters in Γ, and $\boldsymbol{k}$ belonging to BZ_Γ. Applying this transformation to Eq. (2.9) one gets after a short computation

$$\mathcal{O} = \sum_{\boldsymbol{k}} \sum_{a,b} \underbrace{\left[\sum_{\boldsymbol{\Delta}} T_{a,b}(\boldsymbol{\Delta}) \mathrm{e}^{-\mathrm{i}\boldsymbol{k}\boldsymbol{\Delta}} \right]}_{T_{a,b}(\boldsymbol{k})} c_{\boldsymbol{k},a}^{\dagger} c_{\boldsymbol{k},b}.$$

The term inside the brackets is the superlattice Fourier-transformed hopping term $T_{a,b}(\boldsymbol{k})$. Note that $\boldsymbol{\Delta}$ has to be given in units of the original lattice spacing and not of the superlattice Γ, for instance for a L-site chain one has $\boldsymbol{\Delta} = \pm L$ and not ± 1. With this transformation Eq. (2.3) reads as

$$G_{a,b}^{-1}(\boldsymbol{k},\omega) = G_{a,b}'^{-1}(\omega) - T_{a,b}(\boldsymbol{k}). \tag{2.10}$$

This equation is still in a mixed representation, quantum numbers a and b within a cluster and momentum vector $\boldsymbol{k}$ with respect to the superlattice. In order to get a fully momentum-dependent Green's function one has to apply Fourier transformation once more, but now within the cluster. Since translational symmetry is broken on this level, the resulting Green's function will not be diagonal in the momenta. More specifically, one has

$$\begin{aligned} G(\boldsymbol{k}+\boldsymbol{K},\boldsymbol{k}+\boldsymbol{K}',\omega) &= \frac{1}{N_{\mathrm{c}}}\sum_{\boldsymbol{r}_a,\boldsymbol{r}_b} \mathrm{e}^{\mathrm{i}(\boldsymbol{k}+\boldsymbol{K})\boldsymbol{r}_a}\mathrm{e}^{-\mathrm{i}(\boldsymbol{k}+\boldsymbol{K}')\boldsymbol{r}_b} G_{a,b}(\boldsymbol{k},\omega) \\ &= \frac{1}{N_{\mathrm{c}}}\sum_{\boldsymbol{r}_a,\boldsymbol{r}_b} \mathrm{e}^{\mathrm{i}\boldsymbol{k}(\boldsymbol{r}_a-\boldsymbol{r}_b)}\mathrm{e}^{\mathrm{i}\boldsymbol{K}\boldsymbol{r}_a-\mathrm{i}\boldsymbol{K}'\boldsymbol{r}_b} G_{a,b}(\boldsymbol{k},\omega), \end{aligned}$$

with N_{c} the number of sites in the cluster, and $\boldsymbol{r}_{a/b}$ the lattice coordinates according to quantum numbers a/b. The non-diagonal terms $\boldsymbol{K} \neq \boldsymbol{K}'$ arise due to the different treatment of inter-cluster and intra-cluster bonds. Within the CPT, these terms are neglected, and only the $\boldsymbol{K} = \boldsymbol{K}' = 0$ part of the Green's function is taken into account. Therefore one ends up with

$$G(\boldsymbol{k},\omega) = \frac{1}{N_{\mathrm{c}}}\sum_{\boldsymbol{r}_a,\boldsymbol{r}_b} \mathrm{e}^{\mathrm{i}\boldsymbol{k}(\boldsymbol{r}_a-\boldsymbol{r}_b)} G_{a,b}(\boldsymbol{k},\omega). \tag{2.11}$$

Eq. (2.11) together with Eq. (2.10) are the key ingredients of all CPT calculations.

2.1.3. Limiting cases of CPT

Obviously the CPT is exact in the limit $N_{\mathrm{c}} \to \infty$, i.e., for an infinitely large cluster. Moreover it is exact in the limit $\boldsymbol{T} \to 0$, since it is based on a strong-coupling expansion in the inter-cluster hopping terms.

But in addition to the strong-coupling limit, CPT is exact in the limit $U = 0$, too. At first sight this behavior looks paradoxical, but it follows straightforwardly from Eq. (2.8). For $U = 0$ the self-energy of the system is exactly zero, and Eq. (2.8) is the exact expression for the non-interacting Green's function.

The fact that CPT is exact in the limit $U = 0$ is a useful test that is carried out often in practice, since the spectrum in this limit is known.

2.1.4. Comparison with exact diagonalisation

At the end of this section on CPT, we want to demonstrate the capabilities of this method. Here we want to investigate the convergence behavior of results obtained from different cluster sizes, and compare them with results from exact diagonalisation of finite size systems with periodic boundary conditions (pbc). For this purpose we calculate the spectral function

$$A(\boldsymbol{k},\omega) = -\frac{1}{\pi}\lim_{\eta\to 0} \mathrm{Im}\ G(\boldsymbol{k},\omega+\mathrm{i}\eta), \tag{2.12}$$

with η a small real number. As toy model the Hubbard model in one dimension is used, with Hamiltonian

$$H = -t\sum_{i\sigma}(c^{\dagger}_{i\sigma}c_{i+1,\sigma} + \mathrm{H.c.}) + U\sum_{i} n_{i\uparrow}n_{i\downarrow} - \mu\sum_{i} n_i, \tag{2.13}$$

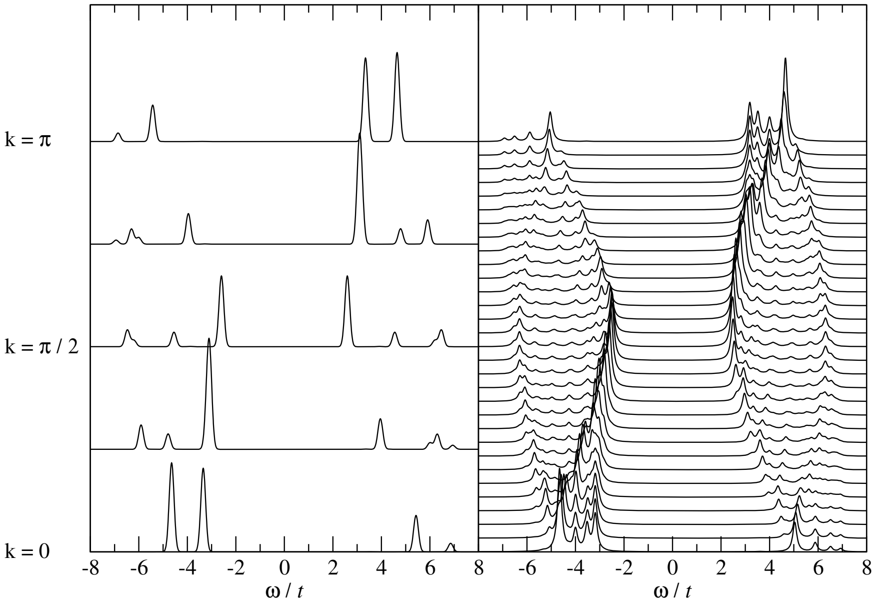

Figure 2.2.: Comparison of the spectral function of the Hubbard model at half filling and $U = 8t$. Left: ED results from an 8 site cluster with pbc. Right: Spectral function from CPT with $N_\mathrm{c} = 8$. A broadening of $\eta = 0.1$ was used to give the delta peaks a finite width.

with $n_{i\sigma} = c^\dagger_{i\sigma} c_{i\sigma}$ and $n_i = n_{i\uparrow} + n_{i\downarrow}$. At half filling, were the further calculations have been done, this model exhibits particle-hole symmetry, and therefore the chemical potential is set to $\mu = U/2$. We used $U = 8t$ for the Hubbard interaction.

In Fig. 2.2 we compare the possible $\boldsymbol{k}$-resolution of ED and CPT, when diagonalisations are done on an 8 site cluster. Whereas ED is restricted to a small number of momentum vectors, e.g., 5 independent vectors on the 8 site cluster, CPT can provide the spectral function for any momentum vector. In Fig. 2.2, 31 momenta are shown, but in general there is no limitation on the $\boldsymbol{k}$-resolution.

Another interesting question is the dependence of the results on the cluster size N_c. For this reason we calculated the spectral function at momentum $k = \pi/2$ for $N_\mathrm{c} = 4, 8$ and 12, and the parameters of the Hamiltonian were the same as given above. The CPT calculations would allow the momentum $\pi/2$ also for $N_\mathrm{c} = 6$ or $N_\mathrm{c} = 10$, but for these cluster sizes the momentum is not available in exact diagonalisation. The results of the calculations are shown in Fig. 2.3. As one can see, CPT converges rapidly with increasing cluster size, and already for $N_\mathrm{c} = 8$ one can get well converged results. In contrast the convergence of ED is rather poor.

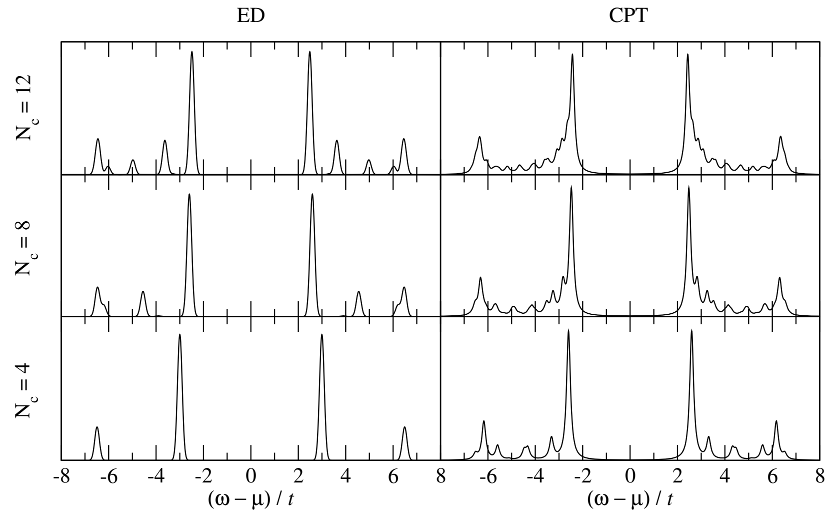

Figure 2.3.: Comparison of the dependence of the spectral function at $k = \pi/2$ on the cluster sizes. Left: ED results. Right: CPT results.

2.2. Variational Cluster Perturbation Theory

The CPT derived in the previous section is only one cluster approximation to strongly-correlated systems among many others, like the DCA [13] or the C-DMFT [14–16]. In contrast to these cluster extensions of the DMFT, CPT does not involve any self-consistency procedure, and thus does not allow for the occurrence of symmetry-broken phases. In this section it is shown that both, the CPT and the C-DMFT, can be considered as extreme limits of a more general cluster approach [2] which is based on the self-energy-functional approach (SFA) proposed recently [5, 6]. This answers an open question for the relation between the different cluster methods [4], and unifies two approaches which appear to be rather different at first sight. In the context of this more general approach, termed variational cluster perturbation theory (V-CPT), the investigation of symmetry broken phases is possible.

2.2.1. Self-energy-functional approach (SFA)

Consider a system of fermions on an infinite lattice with on-site Coulomb interactions at temperature T and chemical potential μ. Its Hamiltonian $H = H_0(\boldsymbol{t}) + H_1(\boldsymbol{U})$ consists of a one-particle part which depends on a set of hopping parameters $\boldsymbol{t}$ and an interaction part with Coulomb-interaction parameters $\boldsymbol{U}$. The grand potential Ω can be obtained from the stationary point of a self-energy functional

$$\Omega_{\boldsymbol{t}}[\boldsymbol{\Sigma}] \equiv \mathrm{Tr}\, \ln(-(\boldsymbol{G}_0^{-1} - \boldsymbol{\Sigma})^{-1}) + F[\boldsymbol{\Sigma}] \tag{2.14}$$

as has been discussed in Ref. [5]. Here $\boldsymbol{G}_0 = 1/(\omega + \mu - \boldsymbol{t})$ is the non-interacting Green's function, and $F[\boldsymbol{\Sigma}]$ is the Legendre transform of the Luttinger-Ward functional $\Phi[\boldsymbol{G}]$.

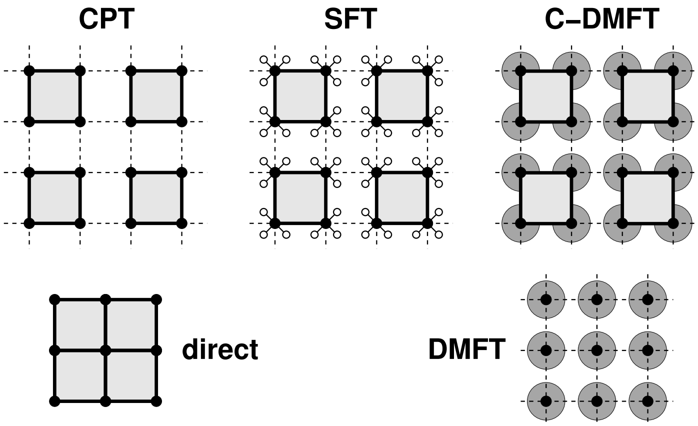

Figure 2.4.: Reference systems considered within various cluster approximations for the 2D Hubbard model. Filled circles: on-site interaction. Solid lines: intra-cluster hopping. Dashed lines: inter-cluster hopping. Open circles: additional n_b uncorrelated bath sites. Big circles: bath with $n_\mathrm{b} = \infty$. Common to all methods is (i) the numerical solution of the system of decoupled clusters and (ii) the subsequent coupling of the clusters via an RPA-like or Dyson equation. Bath parameters are determined self-consistently. The self-energy-functional approach (SFA) comprises the extreme limits CPT ($n_\mathrm{b} = 0$) and C-DMFT ($n_\mathrm{b} = \infty$).

As the latter is constructed as an infinite series of renormalized skeleton diagrams [22], the self-energy functional is not known explicitly. Nevertheless, the *exact* evaluation of $\Omega_{\boldsymbol{t}}[\boldsymbol{\Sigma}]$ and the determination of the stationary point is possible on a *restricted* space $\mathcal{S}$ of trial self-energies $\boldsymbol{\Sigma}(\boldsymbol{t}') \in \mathcal{S}$ [5]. Due to this restriction the procedure becomes approximative.

Generally, the space $\mathcal{S}$ consists of $\boldsymbol{t}'$ representable self-energies. $\boldsymbol{\Sigma}$ is termed $\boldsymbol{t}'$ representable if there are hopping parameters $\boldsymbol{t}'$ such that $\boldsymbol{\Sigma} = \boldsymbol{\Sigma}(\boldsymbol{t}')$ is the exact self-energy of the model $H' = H_0(\boldsymbol{t}') + H_1(\boldsymbol{U})$ ("reference system"). Note that both the original system H and the reference system H' must share the same interaction part. For any $\boldsymbol{\Sigma}$ parameterized as $\boldsymbol{\Sigma}(\boldsymbol{t}')$ we have [5]

$$\begin{aligned}\Omega(\boldsymbol{t}') = \Omega_{\boldsymbol{t}}[\boldsymbol{\Sigma}(\boldsymbol{t}')] &= \Omega' + \mathrm{Tr}\,\ln(-(\boldsymbol{G}_0^{-1} - \boldsymbol{\Sigma}(\boldsymbol{t}'))^{-1}) - \mathrm{Tr}\,\ln(-\boldsymbol{G}') \\ &= \Omega' + \mathrm{Tr}\,\ln(-\boldsymbol{G}) - \mathrm{Tr}\,\ln(-\boldsymbol{G}'),\end{aligned} \tag{2.15}$$

where Ω', $\boldsymbol{G}'$, and $\boldsymbol{\Sigma}(\boldsymbol{t}')$ are the grand potential, the Green's function and the self-energy of the reference system H', while $\boldsymbol{G}_0$ is the free Green's function of H, and $\boldsymbol{G}$ is the SFA approximation for the interacting Green's function of H. Note that $\boldsymbol{G}$ is given by the CPT formula Eq. (2.8). For a proper choice of $\boldsymbol{t}'$ (namely such that certain degrees of freedom in H', e.g., those in different clusters, are decoupled), a (numerically) exact computation of these quantities is possible. Hence, the self-energy functional (2.15) can be evaluated exactly for this $\boldsymbol{\Sigma} = \boldsymbol{\Sigma}(\boldsymbol{t}')$. A certain approximation is characterized by a choice for $\mathcal{S}$. As $\boldsymbol{\Sigma}$ is parameterized by $\boldsymbol{t}'$, this means to specify a space of variational parameters $\boldsymbol{t}'$. Any choice will lead by construction to a non-perturbative and thermodynamically consistent approach. For a further discussion of the general concepts of the SFA see Refs. [5, 6].

Fig. 2.4 illustrates the construction of cluster approximations within the SFA framework. To be specific, H is taken to be the Hubbard model with nearest-neighbor hopping. Subdividing the infinite lattice into identical clusters of finite size, H' is obtained from H by switching off the inter-cluster hopping and switching on the hopping to new uncorrelated ($U_{\text{bath}} = 0$) bath sites (Fig. 2.4, middle). Both operations merely change the one-particle part of the Hamiltonian, i.e. $\boldsymbol{t} \to \boldsymbol{t}'$, while the interaction part ($\boldsymbol{U}$) remains fixed – as required. To search for a stationary point on this space $\mathcal{S}$ of cluster-representable self-energies, one has to proceed as follows:

(i) Compute the self-energy $\boldsymbol{\Sigma}(\boldsymbol{t}')$ of the reference system for a given $\boldsymbol{t}'$.

(ii) Use Eq. (2.15)) to evaluate $\Omega_{\boldsymbol{t}}[\boldsymbol{\Sigma}]$ at $\boldsymbol{\Sigma} = \boldsymbol{\Sigma}(\boldsymbol{t}')$.

(iii) Repeat steps (i) and (ii) for different $\boldsymbol{t}'$ to compute the function $\Omega(\boldsymbol{t}') \equiv \Omega_{\boldsymbol{t}}[\boldsymbol{\Sigma}(\boldsymbol{t}')]$ and the stationary point $\boldsymbol{t}'_{\text{s}}$ given by $\partial\Omega(\boldsymbol{t}'_{\text{s}})/\partial\boldsymbol{t}' = 0$.

The proof of causality of this approach is given in Sec. B.

The variational adjustment of the intra-cluster one-particle parameters $\boldsymbol{t}'$ can be looked upon as a (partial) compensation for the error introduced by the finite cluster size. An inclusion of n_{b} bath sites per original correlated site enlarges the number of variational parameters and thereby the space $\mathcal{S}$. This is expected to (and does) improve the approximation (see results below). In the limit of infinite cluster size (number of correlated sites within a cluster $N_{\text{c}} \to \infty$), the *exact* self-energy becomes $\boldsymbol{t}'$ representable and therefore the cluster approximation itself becomes exact.

Evaluation of the grand potential

So far we did not discuss how the evaluation of Eq. (2.15) is done in practice. For zero temperature, the quantities of the reference system, Ω' and $\boldsymbol{G}'$, are obtained by the Lanczos algorithm discussed in Sec. 2.3.

More attention has to paid on the evaluation of the traces. In general the trace consists of a sum over a full set of quantum numbers α and Matsubara frequencies $\mathrm{i}\omega_n = \mathrm{i}(2n+1)\pi T$, i.e.,

$$\operatorname{Tr}\boldsymbol{X} = T\sum_{\omega_n,\alpha} X_{\alpha\alpha}(\mathrm{i}\omega_n)$$

for an arbitrary function $\boldsymbol{X}$ at temperature T. For our purposes it is now convenient to split the set of quantum numbers α into quantum numbers $\boldsymbol{k}$ according to the superlattice of the clusters, and quantum numbers a within a cluster. Therefore we can write for the second term in Eq. (2.15)

$$\mathrm{Tr}\ \ln(-\boldsymbol{G}) = T\sum_{\omega_n}\sum_{\boldsymbol{k}}\sum_{a}\left[\ln(-\boldsymbol{G}(\boldsymbol{k},\mathrm{i}\omega_n))\right]_{aa}, \tag{2.16}$$

where we used that $\boldsymbol{G}$ is diagonal in the super lattice quantum number $\boldsymbol{k}$. The third term in Eq. (2.15) can be further simplified, since $\boldsymbol{G}'$ does not depend on $\boldsymbol{k}$ and the summation is trivial, yielding

$$\mathrm{Tr}\ \ln(-\boldsymbol{G}') = TL\sum_{\omega_n}\sum_{a}\left[\ln(-\boldsymbol{G}'(\mathrm{i}\omega_n))\right]_{aa}, \tag{2.17}$$

with L the number of clusters (or $\boldsymbol{k}$-points, respectively). The sum over quantum numbers a, e.g. site indices, can be computed as

$$\sum_{a}[\ln(-\boldsymbol{G}^{(\prime)}(\mathrm{i}\omega_n))]_{aa} = \ln\det[-\boldsymbol{G}^{(\prime)}(\mathrm{i}\omega_n)]. \tag{2.18}$$

The sum over Matsubara frequencies can be evaluated by continuation to the real ω axis yielding

$$\begin{aligned} T\sum_{\omega_n} X(\mathrm{i}\omega_n) &= -\frac{1}{\pi}\lim_{\eta\to 0}\int_{-\infty}^{\infty}\mathrm{d}\omega f(\omega)\ \mathrm{Im}\ X(\omega+\mathrm{i}\eta) \\ &\overset{T\to 0}{=} -\frac{1}{\pi}\lim_{\eta\to 0}\int_{-\infty}^{0}\mathrm{d}\omega\ \mathrm{Im}\ X(\omega+\mathrm{i}\eta) \end{aligned} \tag{2.19}$$

with the Fermi function $f(\omega) = (\exp(\omega/T)+1)^{-1}$. By combining Eqs. (2.18) and (2.19) one can evaluate Eqs. (2.16) and (2.17).

Note that Eq. (2.19) holds only, if the chemical potential is included in the Hamiltonian, i.e. $\mathcal{H} = H - \mu N$. If it is not included, because it is for instance not known a priori, then the upper boundary of the integration is shifted, $0 \to \mu$. The actual value of μ can be determined from the condition for the electron density n

$$n = -\frac{2}{\pi L}\sum_{\boldsymbol{k}}\lim_{\eta\to 0}\int_{-\infty}^{\mu}\mathrm{d}\omega\ \mathrm{Im}\ G(\boldsymbol{k},\omega+\mathrm{i}\eta). \tag{2.20}$$

This means that for unknown μ one ends up with a self-consistent procedure, consisting of the following steps.

(i) Start with a certain (educated) guess for μ.

(ii) Determine the stationary point of Ω (Eqs. (2.15) to (2.19)) with this guess for μ and calculate the Green's function at this point.

(iii) Calculate a new value of μ from Eq. (2.20). Back to step (ii) until convergence.

We will see later on how this self-consistent cycle can be avoided in special cases.

2.2.2. CPT and C-DMFT

For a certain cluster approximation, it has to be specified which of the different intra-cluster one-particle parameters $\boldsymbol{t}'$ are treated as variational parameters. The simplest idea is to consider the intra-cluster hopping as fixed at the original values, $t'_{ij} = t_{ij}$ (for i, j in the same cluster), and not to switch on a hopping to bath sites (i.e., not to introduce any bath sites). In this case there is no variational parameter at all. $\boldsymbol{\Sigma}(\boldsymbol{t}')$ is calculated once, and the Green's function $\boldsymbol{G}$ for the original model is obtained by the (lattice) Dyson equation $\boldsymbol{G}^{-1} = \boldsymbol{G}_0^{-1} - \boldsymbol{\Sigma}(\boldsymbol{t}')$. By comparing this equation with Eq. (2.8) one can see that the CPT is recovered, and the reference system is simply a cluster of finite size.

The C-DMFT is obtained by introducing a hopping t'_{ir} to $n_\mathrm{b} = \infty$ bath sites $r = 1, ..., n_\mathrm{b}$ per correlated site $i = 1, ..., N_\mathrm{c}$ and taking this hopping ("hybridization") and the bath on-site energies $\epsilon'_{i,r}$ as variational parameters while for the correlated sites $t'_{ij} = t_{ij}$ is still fixed. Assume that bath parameters $\{t'_{ir}, \epsilon'_{i,r}\}$ can be found such that the C-DMFT self-consistency equation is fulfilled. In Ref. [14] this was given in $\boldsymbol{k}$-space representation ($\boldsymbol{k}$ from the reduced Brillouin zone). In the real-space representation the self-consistency equation reads

$$(\boldsymbol{G}_0^{-1} - \boldsymbol{\Sigma}(\{t'_{ir}, \epsilon'_{i,r}\}))^{-1}_{ij} = G'_{ij} \,, \tag{2.21}$$

where i, j must belong to the same cluster. This immediately implies that $\boldsymbol{\Sigma}(\{t'_{ir}, \epsilon'_{i,r}\})$ satisfies the SFA Euler equation $\partial\Omega(\boldsymbol{t}')/\partial\boldsymbol{t}' = 0$ or, calculating the derivative,

$$T \sum_\omega \sum_{ij} \left(\frac{1}{\boldsymbol{G}_0^{-1} - \boldsymbol{\Sigma}(\boldsymbol{t}')} - \boldsymbol{G}' \right)_{ji} \frac{\partial \Sigma_{ij}(\boldsymbol{t}')}{\partial \boldsymbol{t}'} = 0 \,. \tag{2.22}$$

This holds since the "projector" $\partial\Sigma_{ij}(\boldsymbol{t}')/\partial\boldsymbol{t}' = 0$ if i, j belong to different clusters as these are decoupled in the reference system. We conclude that the self-energy functional is stationary at the C-DMFT self-energy.

2.2.3. Intermediate approach, V-CPT

The C-DMFT self-consistency equation can generally be fulfilled for $n_\mathrm{b} = \infty$ only. Within a cluster approach based on the SFA there are no formal problems, however, if $n_\mathrm{b} < \infty$. A finite n_b yields an approximation *inferior* as compared to $n_\mathrm{b} = \infty$ (C-DMFT) and *superior* as compared to $n_\mathrm{b} = 0$ (CPT) as there are less or more variational parameters, respectively. For $0 < n_\mathrm{b} < \infty$ the parameters must be found to satisfy Eq. (2.22). Since the convergence with respect to n_b appears to be rapid for local physical quantities [5] and since the cluster Hilbert-space dimension increases exponentially with n_b, approximations with small n_b (or even $n_\mathrm{b} = 0$, CPT) appear advantageous. Anyway, the bath concept must become irrelevant in the limit $N_\mathrm{c} \to \infty$. On the other hand, there are good reasons to introduce bath sites: Depending on

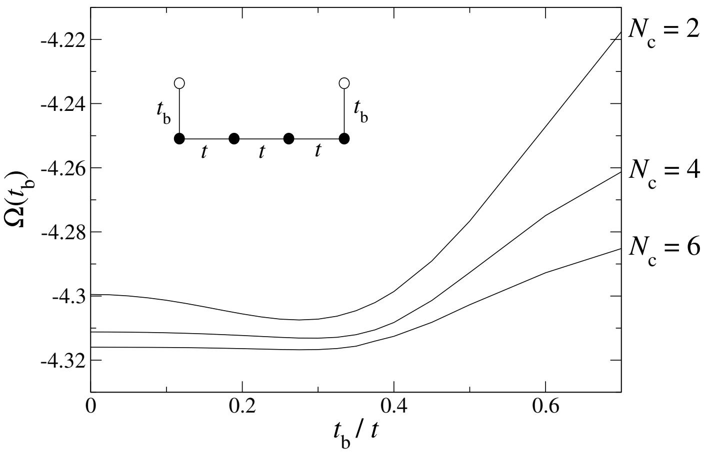

Figure 2.5.: Grand potential Ω vs. t_b, the hopping to uncorrelated bath sites at the cluster boundaries. Reference systems with N_c correlated sites and two bath sites, as shown in the inset for $N_c = 4$.

the dimensionality of the problem, it can be the description of the local (temporal) correlations that needs to be improved in first place. Note that for $N_c = 1$ and $n_b = \infty$ the DMFT is recovered which represents the *exact* solution for $D = \infty$ [12]. Furthermore, bath sites can serve as particle reservoirs which will be essential for a proper description of filling dependencies. Finally, the presence of bath sites may also facilitate practical calculations to treat the reference system, e.g., by an attenuation of the sign problem in the context of a Hirsch-Fye like QMC approach [23]. For any n_b, the SFA provides the framework for a consistent cluster approach.

It is now possible to construct such a cluster approach by attaching uncorrelated bath sites only at the boundaries of the respective cluster, in contrast to C-DMFT, where $n_b = \infty$ bath sites are attached to *all* correlated sites. This choice is motivated by the expectation that here bath degrees of freedom compensate for the finite-size errors most efficiently.

Fig. 2.5 shows results for the 1D Hubbard model, Eq. (2.13) at half filling. Because of particle-hole symmetry the chemical potential is $\mu = U/2$, and the onsite potential of the bath sites is fixed to $\epsilon_b = 0$. For this reason we have to deal only with one variational parameter, the hopping t_b between correlated sites and bath sites. Instead of solving the Euler equation, Eq. (2.22), the grand potential is calculated directly from Eq. (2.15). One can see that switching on t_b to two bath sites in fact lowers the grand potential (and the minimal energy $E_0 = \Omega + \mu\langle N\rangle'$). With increasing N_c the energy difference $E_0(t_b = t_b^{\min}) - E_0(0)$ decreases, and $E_0(t_b)$ becomes almost flat for small t_b, as expected. Note that the binding energy gain due to inclusion of two bath sites $|E_0(N_c, t_b^{\min}) - E_0(N_c, 0)|$ is always smaller than the gain $|E_0(N_c + 2, 0) - E_0(N_c, 0)|$ due to a larger cluster: Introducing bath sites is less efficient as increasing the cluster size, at least in one dimension.

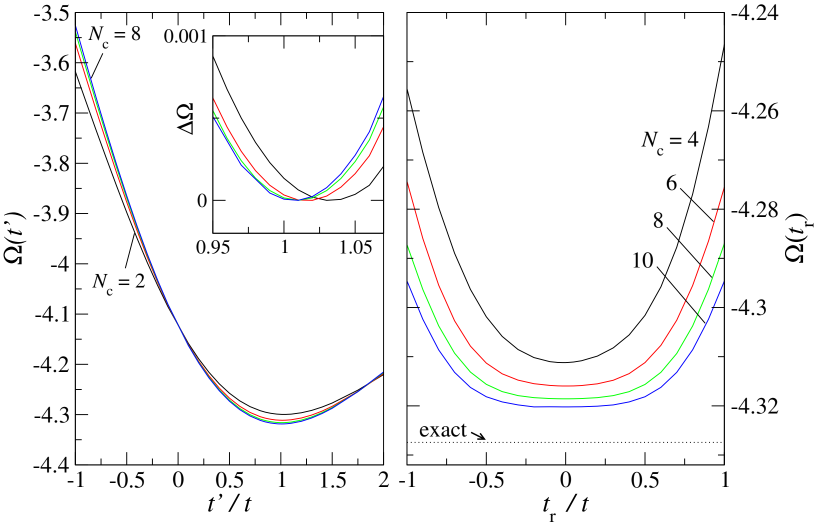

Figure 2.6.: Different hopping parameters as variational parameters. Left: Ω as function of the intra-cluster hopping t'. Results are shown for $N_c = 2, 4, 6$, and 8 (black, red, green, and blue line, resp.). The inset shows the deviation of Ω near $t' = t$. Right: Hopping across pbc t_r as variational parameter, for $N_c = 4, 6, 8$, and 10. The dotted line marks the exact result taken from Ref. [1].

Within the framework of the V-CPT it is now possible to investigate the quality of approximations done by CPT. For both the CPT and the C-DMFT the hopping between correlated sites is fixed at $t'_{ij} = t_{ij}$ (for the C-DMFT, this is even a necessary condition to satisfy Eq. (2.21) as can easily be seen from a high-frequency expansion). Contrary, within the SFA there is *a priori* no reason to fix t'_{ij}.

The left plot of Fig. 2.6 shows $\Omega(t')$ where t' is the nearest-neighbor hopping within the cluster, given in units of the original hopping t. Clearly, Ω is stationary for t' very close to t, but $t' \neq t$. The effect is most obvious for the smallest cluster size $N_c = 2$ (see inset). We conclude that a variational determination of the hopping between the correlated sites in fact improves the approximation. Surprisingly, however, the improvement is almost negligible for reasonable N_c. Note that the curves for different cluster sizes cross at exactly $t' = 0$. This is not surprising, since this case refers to the atomic limit, and thus the results are independent of N_c.

As mentioned in Sec. 2.1 CPT does not give a proof for the proper choice of boundary conditions. The question of the correct boundary conditions is decided *a posteriori* by inspection of the respective results for the spectral density [4]. Here we introduce a hopping parameter t_r between the edge sites and let the method “decide” by itself. As is seen in Fig. 2.6 (right), a minimum for Ω is obtained at $t_r = 0$ (obc) while there is no indication for a stationary point at $t_r = t$ (pbc).

2.2.4. Symmetry-broken phases

As discussed in the beginning of this chapter, the CPT cannot describe symmetry-broken phases, since no self-consistent procedure is involved. This limitation can be overcome by V-CPT, since in this framework we have a certain amount of freedom for the choice of the reference system H'. We want to motivate the approach by the following observation. Obviously the perturbation term in Eq. (2.1) need not necessarily be restricted to the inter-cluster hopping term but can be any one-particle operator. To be specific the decoupled Hamiltonian Eq. (2.1) is invariant under the transformation

$$\begin{aligned} H_0^{(\mathrm{c})}(\boldsymbol{R}) &\to H_0^{(\mathrm{c})}(\boldsymbol{R}) + \mathcal{O}(\boldsymbol{R}) \\ H_0^{(\mathrm{i})}(\boldsymbol{R},\boldsymbol{R}') &\to H_0^{(\mathrm{i})}(\boldsymbol{R},\boldsymbol{R}') - \delta_{\boldsymbol{R},\boldsymbol{R}'}\mathcal{O}(\boldsymbol{R}), \end{aligned} \tag{2.23}$$

with an arbitrary intra-cluster one-particle operator

$$\mathcal{O}(\boldsymbol{R}) = \sum_{a,b} \Delta_{a,b}\, c^\dagger_{\boldsymbol{R},a} c_{\boldsymbol{R},b}, \tag{2.24}$$

with a and b general quantum numbers in the cluster. In terms of CPT this means, that a one-particle operator is added to the cluster Hamiltonian, and subtracted again perturbatively. The SFA interpretation is that the Hamiltonian of the reference system H' includes additional one-particle terms with parameters $\boldsymbol{\Delta} = \Delta_{a,b}$, which are not present in the original lattice Hamiltonian, similar to the addition of bath sites.

The reason for this inclusion of additional terms is that one may think of choosing $\boldsymbol{\Delta}$ such that the single-particle dynamics of the cluster problem is "as close as possible" to the exact dynamics of the lattice. Depending on the problem under consideration, this one-particle operator, Eq. (2.24), can be chosen to represent a fictitious symmetry-breaking field, e.g., a staggered magnetic field. Thus, this approach allows for broken symmetry already on a finite system instead of only in the thermodynamic limit.

The question of what choice for $\boldsymbol{\Delta}$ will optimize the results can be answered by the SFA, because the elements of $\boldsymbol{\Delta}$ are nothing else than variational parameters in the SFA-optimization procedure.

Note that *all* variational parameters of H' can be written as elements of $\boldsymbol{\Delta}$, since Eq. (2.24) is a completely arbitrary one-particle operator. For instance let us assume that the hopping in the cluster t' is a variational parameter. Then it can easily be derived from Eq. (2.23) that the corresponding term in $\boldsymbol{\Delta}$ for the 1D Hubbard model would be $\Delta_{i,i+1} = \Delta_{i,i-1} = -(t' - t)$, the difference between hopping of the original model t and intra-cluster hopping t'. As a matter of convenience, we therefore parametrize the grand potential from now on as $\Omega \equiv \Omega(\boldsymbol{\Delta})$, where $\boldsymbol{\Delta}$ includes all variational parameters under consideration.

2.3. Exact diagonalisation

In the previous sections we introduced CPT and its extensions. Since one key element of these approaches is the exact evaluation of properties on clusters of finite size, we present the exact diagonalisation (ED) methods that we used for these purposes in this section. ED methods are based on a very simple idea: By choosing a suitable basis we can transfer the Hamiltonian of the systems into a Hamilton matrix, which can be diagonalized.

This shows already one of the big disadvantages of the ED, because if we enlarge the system the basis and Hamilton matrix will blow up in size. The number of basis states is given by $\binom{N}{n_\uparrow}\binom{N}{n_\downarrow}$ which yields for example 784 basis states for 2 spin up and 2 spin down electrons on 8 sites but already 3 312 400 basis states for 4 spin up and 4 spin down electrons on 16 sites. Therefore the ED is limited to rather small (up to 25 sites) systems. But even for treating these small systems we need powerful numerical algorithms like the Lanczos-method [24], which will be presented in the sequel.

2.3.1. Theoretical background, Krylov space

Let us assume we have chosen a basis and created the Hamilton matrix as matrix elements of the Hamiltonian within this special basis. To understand the way the Lanczos-method works we have to consider invariant subspaces of the Hamilton-matrix.

Assuming the Hamilton matrix is a $(N \times N)$-matrix H, then a M-dimensional subspace $\mathcal{G}$ defined as the linear span of the vectors $|\gamma_1\rangle, |\gamma_2\rangle, \ldots, |\gamma_M\rangle$ with $M < N$ is called an invariant subspace, if

$$|\phi\rangle \in \mathcal{G} \Longrightarrow H|\phi\rangle \in \mathcal{G}$$

for every element $|\phi\rangle$ of $\mathcal{G}$. This definition implies, that every eigenstate of H spans a one-dimensional invariant subspace. If we use an arbitrary basis $|\gamma_1\rangle, \ldots, |\gamma_M\rangle$ we can write $\mathcal{G}$ as a $(N \times M)$-matrix, where the columns $|\gamma_i\rangle$ of this matrix are the basis vectors of the subspace. If $\mathcal{G}$ is an invariant subspace of the Hamilton matrix H, then the matrix product $\mathcal{H}\mathcal{G}$ is again a $(N \times M)$-matrix, where the columns are linear combinations of the $|\gamma_i\rangle$. Now we can define a $(M \times M)$-matrix H_M by

$$\mathcal{H}\mathcal{G} = \mathcal{G}\mathcal{H}_M \tag{2.25}$$

Suppose we can find a solution of the eigenvalue problem

$$H_M|\psi\rangle = \varepsilon|\psi\rangle \tag{2.26}$$

of H_M, then a solution of the eigenvalue problem of H can be constructed. If we use Eq. (2.26) in Eq. (2.25) we get

$$H[\mathcal{G}|\psi\rangle] = \varepsilon[\mathcal{G}|\psi\rangle].$$

This means, that we can find eigenvectors and eigenvalues of the high-dimensional Hamilton matrix H by solving the eigenvalue problem of the smaller matrix H_M, if $\mathcal{G}$ is an invariant subspace.

As discussed below the idea of the Lanczos algorithm is to construct iteratively an approximately invariant subspace of H, the so called Krylov space

$$K_M = \text{linspan}\left\{|\phi_0\rangle, H|\phi_0\rangle, H^2|\phi_0\rangle, \ldots, H^{M-1}|\phi_0\rangle\right\}, \qquad M < N, \tag{2.27}$$

where $|\phi_0\rangle$ is a normalized random vector. It has to be verified, that the Krylov-space has the above mentioned properties, which can be seen as follows.

If we apply the Hamiltonian H to the basis vectors of the Krylov-space Eq. (2.27), we get the set

$$\left\{H|\phi_0\rangle, H^2|\phi_0\rangle, \ldots, H^M|\phi_0\rangle\right\},$$

which are elements of K_M apart from the last vector. If we consider now a large value for M, we find the following convergence behavior:

$$\begin{aligned} H^{M-1}|\phi_0\rangle &= H^{M-1}\sum_{l=0}^{N} c_l|\psi_l\rangle \\ &= \sum_{l=0}^{N} c_l\varepsilon_l^{M-1}|\psi_l\rangle \\ &= c_0\varepsilon_0^{M-1}\left(|\psi_0\rangle + \sum_{l=1}^{N}\frac{c_l}{c_0}\left(\frac{\varepsilon_l}{\varepsilon_0}\right)^{M-1}|\psi_l\rangle\right), \end{aligned}$$

where ε_l and $|\psi_l\rangle$ are eigenvalues and eigenvectors of H. Provided

$$|\varepsilon_0| > |\varepsilon_l|, \qquad l > 0,$$

one can see that for large M the iteration $H^{M-1}|\phi_0\rangle$ converges to the ground state $|\psi_0\rangle$. In other words, for large M the vector $H^{M-1}|\phi_0\rangle$ is dominated by the eigenvectors of H with the largest eigenvalues, which implies that $H^{M-1}|\phi_0\rangle$ is approximately proportional to $H^M|\phi_0\rangle$ and consequently an approximately invariant subspace.

2.3.2. Ground-state Lanczos method

Starting point of the Lanczos procedure is an arbitrary normalized state $|\phi_0\rangle$ of the Hilbert space. It is necessary that this initial state has a non-zero overlap with the ground state of the model under consideration. If no information about the ground state is known, then this condition is usually satisfied by selecting an initial state with coefficients chosen by random. However, if there is some information on the properties of the ground state, like its momentum or spin, it is convenient to use an initial state already belonging to the subspace of these quantum numbers, again with random coefficients in this subspace.

After selecting the initial state $|\phi_0\rangle$, the corresponding expectation value of the energy is

$$\varepsilon_0 = \langle\phi_0|H|\phi_0\rangle.$$

By applying the Hamiltonian and subtracting the overlap with the initial state one constructs a new state

$$|\tilde{\phi_1}\rangle = H|\phi_0\rangle - \varepsilon_0|\phi_0\rangle.$$

After having normalized the new state ($|\tilde{\phi_1}\rangle = \| \tilde{\phi_1} \| \cdot |\phi_1\rangle$), the next iteration reads

$$|\tilde{\phi_2}\rangle = H|\phi_1\rangle - \varepsilon_1|\phi_1\rangle - k_1|\phi_0\rangle.$$

If we choose

$$\begin{aligned} \varepsilon_1 &= \langle\phi_1|H|\phi_1\rangle \\ k_1 &= \langle\phi_0|H|\phi_1\rangle \end{aligned}$$

the new vector $|\tilde{\phi_2}\rangle$ is orthogonal to the first two vectors. Moreover k_1 is real:

$$k_1^* = \langle\phi_1|H|\phi_0\rangle = \langle\phi_1|\tilde{\phi_1}\rangle + \varepsilon_0 \underbrace{\langle\phi_1|\phi_0\rangle}_{=0} = \| \phi_1 \| \in \mathbb{R}.$$

Finally, we got the iteration rule:

$$\begin{aligned} |\tilde{\phi}_{n+1}\rangle &= H|\phi_n\rangle - \varepsilon_n|\phi_n\rangle - k_n|\phi_{n-1}\rangle \\ \varepsilon_n &= \langle\phi_n|H|\phi_n\rangle \\ k_n &= \langle\phi_{n-1}|H|\phi_n\rangle = \| \tilde{\phi}_n \| \\ |\phi_{n+1}\rangle &= \frac{|\tilde{\phi}_{n+1}\rangle}{\| \tilde{\phi}_{n+1} \|} \end{aligned} \tag{2.28}$$

This set of vectors is orthogonal, which can easily be shown by induction.

By this construction the Hamilton matrix represented in the Krylov basis is tridiagonal and has the form

$$H_{ij} = \begin{pmatrix} \varepsilon_0 & k_1 & 0 & \cdot & \cdot & \cdot \\ k_1 & \varepsilon_1 & k_2 & 0 & \cdot & \cdot \\ 0 & k_2 & \varepsilon_2 & k_3 & 0 & \cdot \\ \cdot & 0 & k_3 & \varepsilon_3 & k_4 & \ddots \\ \cdot & \cdot & 0 & k_4 & \varepsilon_4 & \ddots \\ \cdot & \cdot & \cdot & \ddots & \ddots & \ddots \end{pmatrix} \tag{2.29}$$

As discussed in Sec. 2.3.1 the eigenvalues E_ν of this matrix converge to the eigenvalues of the original Hamilton matrix when M becomes large, especially those at the edges of the spectrum. The eigen state $|\psi_\nu\rangle$ of the original Hamilton matrix can be calculated by

$$|\psi_\nu\rangle = \mathcal{G}|\chi_\nu\rangle, \tag{2.30}$$

where the columns of $\mathcal{G}$ consist of the basis vectors of the Krylov space, $|\phi_i\rangle$, and $|\chi_\nu\rangle$ is the eigenvector with energy E_ν of the matrix in Krylov-representation. With the ground state $|\psi_0\rangle$ one can – at $T = 0$ – calculate the static expectation value $\langle\psi_0|A|\psi_0\rangle$ of an observable A.

Dynamical correlations at $T = 0$

The Lanczos algorithm allows not only to calculate the ground state and static expectation values but also dynamic correlation. To every dynamical correlation function there exists a retarded Green's function [25], which is defined for an operator O as

$$\begin{aligned} \ll O(t); O^\dagger \gg &:= -\mathrm{i}\Theta(t)\langle[O(t), O^\dagger]_\epsilon\rangle \\ &= -\mathrm{i}\Theta(t)\left(\langle O(t)O^\dagger\rangle + \epsilon\langle O^\dagger O(t)\rangle\right), \end{aligned} \tag{2.31}$$

where $\epsilon = +1(-1)$ for fermions (bosons). After inserting the Heisenberg time evolution and applying Fourier transformation the Green's function can be written as

$$\begin{aligned} \ll O; O^\dagger \gg_\omega = &-\mathrm{i}\left\langle O\left[\int_0^\infty \mathrm{d}t\, \mathrm{e}^{\mathrm{i}(\omega^+ - (H-E_0))t}\right] O^\dagger\right\rangle \\ &- \mathrm{i}\epsilon\left\langle O^\dagger\left[\int_0^\infty \mathrm{d}t\, \mathrm{e}^{\mathrm{i}(\omega^+ + (H-E_0))t}\right] O\right\rangle, \end{aligned}$$

where E_0 is the ground state energy and $\omega^+ = \omega + \mathrm{i}\eta$ and η a small real quantity. The integration can be done using the spectral theorem and leads to

$$\begin{aligned} \ll O; O^\dagger \gg_\omega =& \langle\psi_0 \mid O\frac{1}{\omega^+ - (H - E_0)}O^\dagger \mid \psi_0\rangle \\ &+\epsilon\langle\psi_0 \mid O^\dagger\frac{1}{\omega^+ + (H - E_0)}O \mid \psi_0\rangle, \end{aligned} \tag{2.32}$$

where $|\psi_0\rangle$ is the ground state. By inserting a complete set of eigen states $|\psi_\nu\rangle$ of H it is possible to replace the operator H by its eigen values, yielding for the first term of Eq. (2.32)

$$\langle\psi_0 \mid O\frac{1}{\omega^+ - (H - E_0)}O^\dagger \mid \psi_0\rangle = \sum_\nu \frac{|\langle\psi_\nu|O^\dagger|\psi_0\rangle|^2}{\omega^+ - (E_\nu - E_0)} \tag{2.33}$$

and a similar expression for the second term. We can now expand the eigenvectors $|\psi_\nu\rangle$ in a Lanczos basis $|\phi_i\rangle$

$$|\psi_\nu\rangle = \sum_i c_i^{(\nu)} |\phi_i\rangle, \qquad c_i^{(\nu)} = \langle \phi_i | \psi_\nu \rangle,$$

where $|\phi_o\rangle = \frac{1}{||O^\dagger \psi_0||} O^\dagger |\psi_0\rangle$ is chosen as the initial vector of the Lanczos procedure, and the $c_i^{(\nu)}$ are the elements of the Krylov eigen vectors $|\chi_\nu\rangle$. Thus we get for the numerator of Eq. (2.33)

$$\langle \psi_\nu | O^\dagger | \psi_0 \rangle = \sum_i \left(c_i^{(\nu)} \right)^* \langle \phi_i | O^\dagger | \psi_0 \rangle = \sum_i \left(c_i^{(\nu)} \right)^* \parallel O^\dagger \psi_0 \parallel \underbrace{\langle \phi_i | \phi_0 \rangle}_{\delta_{i,0}}$$

One can see from this formula that only the first term of the sum contributes, whereas all other terms vanish. Therefore we have

$$\langle \psi_\nu | O^\dagger | \psi_0 \rangle = \left(c_0^{(\nu)} \right)^* \parallel O^\dagger \psi_0 \parallel .$$

With this result we can write for Eq. (2.33)

$$\langle \psi_0 \mid O \frac{1}{\omega^+ - (H - E_0)} O^\dagger \mid \psi_0 \rangle = \parallel O^\dagger \psi_0 \parallel^2 \sum_\nu \frac{|c_0^{(\nu)}|^2}{\omega^+ - (E_\nu - E_0)}, \tag{2.34}$$

using only the first components $c_0^{(\nu)}$ of the expansion of the eigenvectors $|\psi_\nu\rangle$. This method that we presented in this section is called *spectral decoding method.*

Real-space Green's function

The spectral decoding method has a severe drawback, since it can only deal with correlation functions $\ll A; B \gg$ with $A^\dagger = B$. Unfortunately this condition is not fulfilled when calculating the cluster Green's function. The inverse photo-emission (IPES) part is in general given by

$$G_{ab}^{\text{IPES}}(\omega) = \langle \psi_0 | c_a \frac{1}{\omega^+ - (H - E_0)} c_b^\dagger | \psi_0 \rangle, \tag{2.35}$$

with $|\psi_0\rangle$ and E_0 the ground state and its energy, respectively. Note that for $a \neq b$ it is not possible to use Eq. (2.33) for the further calculation. Instead one can proceed with the following. One constructs the states $|\phi\rangle = c_b^\dagger |\psi_0\rangle$ and $|\phi'\rangle = c_a |\psi_0\rangle$. After being normalized, the vector $|\phi\rangle$ is used as initial state for a Lanczos procedure in order to construct an approximate eigen basis $|\psi_\nu\rangle$ of the Hamiltonian. Inserting this eigen basis as approximate unity operator in Eq. (2.35) gives

$$G_{ab}^{\text{IPES}}(\omega) = \sum_\nu^M \langle \phi' | \psi_\nu \rangle \langle \psi_\nu | \phi \rangle \frac{1}{\omega^+ - (E_\nu - E_0)},$$

with M the number of Lanczos steps. The dot products are most efficiently evaluated by expanding the vectors $|\psi_\nu\rangle$ in terms of Lanczos vectors, Eq. (2.30), because then the eigen states need not be calculated explicitly, and the dot products can be computed during the Lanczos procedure.

2.3.3. Finite-temperature Lanczos method

A major disadvantage of the method for calculating dynamical correlation functions as presented in the previous section is the limitation to $T = 0$. Often there is need to calculate dynamical correlations at finite temperatures, for example if one wants to investigate phase transitions. This limitation can, however, be overcome by calculating the thermodynamic trace by random sampling [7]. The matrix elements which are needed in this procedure are again calculated using the Lanczos algorithm.

Static expectation values

The thermodynamic expectation value of an observable O is given by

$$\begin{aligned} \langle O\rangle &= \frac{1}{Z}\sum_{n=1}^{N}\langle n|\mathrm{e}^{-\beta H}O|n\rangle \\ Z &= \sum_{n=1}^{N}\langle n|\mathrm{e}^{-\beta H}|n\rangle \end{aligned} \tag{2.36}$$

where $\beta = 1/T$ denotes the inverse temperature and the sum runs over a complete basis set of orthonormal vectors. If one could determine the full set of eigen states of the Hamiltonian, the evaluation of the exponentials would be straightforward, but because it is quite impossible to find all eigen states another approach is employed.

For calculating the matrix elements we first expand the exponential function into its power series which is equivalent to the high temperature expansion

$$\begin{aligned} \langle O\rangle &= \frac{1}{Z}\sum_{n=1}^{N}\sum_{k=0}^{\infty}\frac{(-\beta)^k}{k!}\langle n|H^kO|n\rangle \\ Z &= \sum_{n=1}^{N}\sum_{k=0}^{\infty}\frac{(-\beta)^k}{k!}\langle n|H^k|n\rangle \end{aligned} \tag{2.37}$$

In the next step we use the Lanczos algorithm to evaluate the matrix elements. Therefore we start a Lanczos procedure with the initial state $|\phi_0^{(n)}\rangle = |n\rangle$ up to the order M. This leads to a tridiagonal representation of H defined in the $(M+1)$-dimensional space spanned by the Krylov basis functions $|\phi_i^{(n)}\rangle, i = 0\dots M$. Let us assume this tridiagonal matrix has the eigen vectors $|\psi_j^{(n)}\rangle$ and eigen values $\varepsilon_j^{(n)}$. Using the Krylov basis $|\phi_i^{(n)}\rangle$ we can define projection operators

$$P_m^{(n)} = \sum_{n=0}^{m} |\phi_i^{(n)}\rangle\langle\phi_i^{(n)}|, m < M$$

which project on a Krylov subspace. Let us now consider the product of such an projection operator with the Hamiltonian. We get

$$P_m^{(n)} H = \sum_{i=1}^{m} |\phi_i^{(n)}\rangle\langle\phi_i^{(n)}|H = \sum_{i=1}^{m} |\phi_i^{(n)}\rangle \left(k_{i+1}^{(n)}\langle\phi_{i+1}^{(n)}| + \varepsilon_i^{(n)}\langle\phi_i^{(n)}| + k_i^{(n)}\langle\phi_{i-1}^{(n)}| \right),$$

where we have used the hermitian conjugate of the Lanczos iteration formula. This formula shows, that the product $P_m^{(n)} H$ consists only of Lanczos vectors up to the order $m+1$. Therefore we can write

$$P_m^{(n)} H = P_m^{(n)} H P_{m+1}^{(n)} = P_m^{(n)} H P_M^{(n)}, \qquad m < M. \tag{2.38}$$

The last step can be done, because the operator $P_M^{(n)}$ projects onto the whole Krylov space and naturally preserves all the states up to order $m+1$. With Eq. (2.38) and $\langle n| = \langle\phi_0^{(n)}| = \langle\phi_0^{(n)}|P_0^{(n)}$ we can write for the matrix element in Eq. (2.37) for $k < M$

$$\begin{aligned}\langle n|H^k O|n\rangle &= \langle\phi_0^{(n)}|P_0^{(n)} H^k O|\phi_0^{(n)}\rangle \\ &= \langle\phi_0^{(n)}|P_0^{(n)} H P_1^{(n)} H \cdots H P_k^{(n)} O|\phi_0^{(n)}\rangle \\ &= \langle\phi_0^{(n)}|P_M^{(n)} H P_M^{(n)} H \cdots H P_M^{(n)} O|\phi_0^{(n)}\rangle\end{aligned} \tag{2.39}$$

The only projection operator used in this formula is $P_M^{(n)}$, which can be seen as the identity operator in the Krylov space. The projection operators can therefore be constructed by the eigen vectors $|\psi_j^{(n)}\rangle$. Inserting the projection operators in Eq. (2.39) yields

$$\langle n|H^k O|n\rangle = \sum_{i=0}^{M} \left(\varepsilon_i^{(n)}\right)^k \langle n|\psi_i^{(n)}\rangle\langle\psi_i^{(n)}|O|n\rangle, \qquad k < M. \tag{2.40}$$

This shows that we can calculate the matrix elements in Eq. (2.37) exactly using the Lanczos algorithm provided $k < M$. But we want to extend the power series to infinity, i.e. $k \to \infty$. For this case we use Eq. (2.40) as approximation also for $k > M$ and thus we can write for the expectation value Eq. (2.37)

$$\begin{aligned}\langle O\rangle &\approx \frac{1}{Z}\sum_{n=1}^{N}\sum_{i=0}^{M} \mathrm{e}^{-\beta\varepsilon_i^{(n)}} \langle n|\psi_i^{(n)}\rangle\langle\psi_i^{(n)}|O|n\rangle \\ Z &\approx \sum_{n=1}^{N}\sum_{i=0}^{M} \mathrm{e}^{-\beta\varepsilon_i^{(n)}} \langle n|\psi_i^{(n)}\rangle\langle\psi_i^{(n)}|n\rangle\end{aligned} \tag{2.41}$$

In Eq. (2.41) the trace still runs over all basis states $|n\rangle$ which is a huge number of states and it is therefore impossible to evaluate the sum in this form. In this approach [7] the trace is evaluated stochastically upon summing over suitable random vectors defined by

$$|r\rangle = \sum_{n=1}^{N} \alpha_n^{(r)} |n\rangle,$$

where the $\alpha_n^{(r)}$ are random variables with zero mean and diagonal variance

$$\overline{\alpha_{n_1}^{(r_1)} \alpha_{n_2}^{(r_2)}} = \delta_{n_1 n_2} \delta_{r_1 r_2}$$

We estimate the trace $\operatorname{Tr} O$ of an operator O by

$$T := \operatorname{Tr} O = \frac{1}{N_r} \sum_{r=1}^{N_r} \langle r|O|r\rangle, \tag{2.42}$$

where N_r is the number of random vectors. The expectation value of the random variable T reads

$$\begin{aligned} \overline{T} &= \frac{1}{N_r} \sum_{r=1}^{N_r} \sum_{n_1=1}^{N} \sum_{n_2=1}^{N} \overline{\alpha_{n_1}^{(r_1)} \alpha_{n_2}^{(r_2)}} \langle n_1|O|n_2\rangle \\ &= \frac{1}{N_r} \sum_{n_1=1}^{N} \langle n_1|O|n_1\rangle \sum_{r=1}^{N_r} 1 = \sum_{n_1=1}^{N} \langle n_1|O|n_1\rangle \end{aligned} \tag{2.43}$$

Therefore Eq. (2.42) represents an unbiased estimator. The variance of the random variable T is given by $\operatorname{var}(T) := \overline{(\Delta T)^2} = \operatorname{Tr} O^2/N_r$. If the operator O is represented by a sparse band-like matrix the trace of this operator is of the order of the dimension of the matrix, $\operatorname{Tr} O \propto O(N)$. When squaring such matrices the band-like structure is conserved, i.e. $\operatorname{Tr} O^2 \propto O(N)$. Therefore the relative error reads

$$\frac{\sqrt{\operatorname{var}(T)}}{\operatorname{Tr} O} \propto \frac{1}{\sqrt{N N_r}},$$

which means that for large N it suffices in general to use a quite small number N_r of random variables.

If we use Eq. (2.42) in Eq. (2.41) we get

$$\begin{aligned} \langle O\rangle &\approx \frac{1}{N_r Z} \sum_{r=1}^{N_r} \sum_{i=0}^{M} \mathrm{e}^{-\beta\varepsilon_i^{(r)}} \langle r|\psi_i^{(r)}\rangle\langle\psi_i^{(r)}|O|r\rangle \\ Z &\approx \frac{1}{N_r} \sum_{r=1}^{N_r} \sum_{i=0}^{M} \mathrm{e}^{-\beta\varepsilon_i^{(r)}} \langle r|\psi_i^{(r)}\rangle\langle\psi_i^{(r)}|r\rangle \end{aligned} \tag{2.44}$$

In conclusion we have achieved to evaluate the expectation value Eq. (2.37) numerically, because it is no longer needed to calculate the sum over all basis states but only over a smaller number of random states.

Dynamical correlations at $T > 0$

By using the same approximations as in the previous section it is possible to calculate dynamical correlation functions. They are defined as

$$\langle A(t)B\rangle = \frac{1}{Z}\sum_{n=1}^{N}\langle n|\mathrm{e}^{-\beta H}\mathrm{e}^{\mathrm{i}Ht}A\mathrm{e}^{-\mathrm{i}Ht}B|n\rangle \tag{2.45}$$

with Z from Eq. (2.36). Similar to the procedure for evaluating the matrix elements for the static expectation values we insert again projection operators which are built by eigen vectors of H calculated by the Lanczos algorithm. One difference is that in this case we need a double sum over these eigen states, since we expand the exponentials $\mathrm{e}^{-(\beta-\mathrm{i}t)H}$ and $\mathrm{e}^{-\mathrm{i}Ht}$. Thus we get

$$\langle A(t)B\rangle = \frac{1}{Z}\sum_{n=1}^{N}\sum_{k=0}^{M}\sum_{l=0}^{M}\mathrm{e}^{(-\beta\varepsilon_k^{(n)})}\mathrm{e}^{\mathrm{i}(\varepsilon_k^{(n)}-\tilde{\varepsilon}_l^{(n)})t}\langle n|\psi_k^{(n)}\rangle\langle\psi_k^{(n)}|A|\tilde{\psi}_l^{(n)}\rangle\langle\tilde{\psi}_l^{(n)}|B|n\rangle, \tag{2.46}$$

where $\tilde{\varepsilon}_l^{(n)}$ and $|\tilde{\psi}_l^{(n)}\rangle$ are eigen values and eigen vectors from a Lanczos run starting with the initial vector $|\tilde{n}\rangle \propto B|n\rangle$. Now we again replace the sum over all basis vectors by a sum over random vectors which leads to the final formula

$$\langle A(t)B\rangle \approx \frac{1}{N_r Z}\sum_{r=1}^{N_r}\sum_{k=0}^{M}\sum_{l=0}^{M}\mathrm{e}^{(-\beta\varepsilon_k^{(r)})}\mathrm{e}^{\mathrm{i}(\varepsilon_k^{(r)}-\tilde{\varepsilon}_l^{(r)})t}\langle r|\psi_k^{(r)}\rangle\langle\psi_k^{(r)}|A|\tilde{\psi}_l^{(r)}\rangle\langle\tilde{\psi}_l^{(r)}|B|r\rangle \tag{2.47}$$

with Z from Eq. (2.44). Here $\tilde{\varepsilon}_l^{(r)}$ and $|\tilde{\psi}_l^{(r)}\rangle$ are eigen energies and eigen states generated with initial state

$$|\tilde{\phi}_0^{(r)}\rangle = B|r\rangle/\sqrt{\langle r|B^{\dagger}B|r\rangle}.$$

This choice of the initial state can be understood similar to importance sampling of Monte Carlo approaches, because in the second Lanczos procedure only the part of the Hilbert space is considered, where the operator B projects onto and hence the terms $\langle\psi_k^{(r)}|A|\tilde{\psi}_l^{(r)}\rangle$ and $\langle\tilde{\psi}_l^{(r)}|B|r\rangle$ in Eq. (2.47) become sufficiently large.

Symmetry sectors

Symmetries of the Hamiltonian can be used in order to decrease the numerical effort in the diagonalisation procedures. By identifying the corresponding conserved quantum numbers, e.g., the number of particles, the projection of the spin S^z, or the momentum $\boldsymbol{k}$, one can write the Hamiltonian in block-diagonal form. Each of these symmetry sectors s is then sampled separately, and the sum over random vectors has to be modified to

$$\frac{1}{N_r}\sum_{r} \quad\rightarrow\quad \sum_{s}\frac{N_s}{N_r}\sum_{r},$$

where N_s is the number of states in sector s. This factor ensures, that the different symmetry sectors are weighted correctly.

2.3.4. Low-temperature Lanczos method

In recent years the Finite Temperature Lanczos Method (FTLM) presented above has allowed the precise calculation of thermodynamic quantities of strongly-correlated systems. It has been applied to the t-J model for the cuprates [26–32] and vanadates [33, 34], orbital t-J model [35], Kondo lattice model [36], Heisenberg model [37] and static properties of the Hubbard model [38]. In principle this method can be applied at all temperatures, but at low temperatures the required number of random samples is very large.

In this section we present the Low Temperature Lanczos Method (LTLM) [8] which allows to calculate properties for large Hilbert spaces at low temperatures that are not accessible by the FTLM.

Let us consider the behavior of Eq. (2.44) and Eq. (2.47) in the limit $T \to 0$. In this case only the ground state $|\psi_0\rangle$ contributes and we get for Eq. (2.44)

$$\langle\mathcal{O}\rangle = \frac{\sum_r^{N_r} \langle\psi_0|\mathcal{O}|r\rangle\langle r|\psi_0\rangle}{\sum_r^{N_r} \langle\psi_0|r\rangle\langle r|\psi_0\rangle} \tag{2.48}$$

and similarly for Eq. (2.47). Thus the ground-state result will suffer from severe statistical fluctuations, although the exact (Lanczos) eigen vector $|\psi_0\rangle$ is reached with every $|r\rangle$ and one random vector should be sufficient. Yet, FTLM gets worse with decreasing temperature T.

The LTLM is designed to overcome this limitation. Let us introduce the method for a static expectation value Eq. (2.36). We use a symmetric form

$$\langle\mathcal{O}\rangle = \frac{1}{Z}\sum_n^N \langle n|\mathrm{e}^{-\frac{1}{2}\beta H}\mathcal{O}\mathrm{e}^{-\frac{1}{2}\beta H}|n\rangle. \tag{2.49}$$

As before, we approximate the trace by random sampling, but now we insert the approximate eigenbasis obtained by the Lanczos procedure twice, initially obtaining

$$\langle\mathcal{O}\rangle = \frac{1}{ZN_r}\sum_r^{N_r}\sum_{i,l}^{M} \mathrm{e}^{-\frac{1}{2}\beta(\varepsilon_i^{(r)}+\varepsilon_l^{(r)})}\langle r|\psi_l^{(r)}\rangle\langle\psi_l^{(r)}|\mathcal{O}|\psi_i^{(r)}\rangle\langle\psi_i^{(r)}|r\rangle \tag{2.50}$$

The partition function Z is calculated in the same way as in standard FTLM. The behavior in the limit $T \to 0$ is now different. If only the ground state $|\psi_0\rangle$ contributes, Eq. (2.50) becomes

$$\begin{aligned}\langle\mathcal{O}\rangle &= \frac{\sum_r^{N_r} \langle\psi_0|r\rangle\langle r|\psi_0\rangle\langle\psi_0|\mathcal{O}|\psi_0\rangle}{\sum_r^{N_r} \langle\psi_0|r\rangle\langle r|\psi_0\rangle} \\ &= \langle\psi_0|\mathcal{O}|\psi_0\rangle. \end{aligned} \tag{2.51}$$

In agreement with the ground-state Lanczos method, one random vector suffices for the ground-state expectation value.

If we compute the numerator in Eq. (2.50) and Z separately, both suffer from pronounced statistical fluctuations, which however cancel exactly at $T = 0$ as shown in Eq. (2.51). For finite T the fluctuations in numerator and denominator do not cancel exactly, although they are still strongly correlated. Separate error analysis for both terms would overestimate the statistical noise. These correlations are taken into account by employing a Jackknife technique [39].

For dynamical correlation functions, a straight-forward variant of Eq. (2.47) suitable for low temperatures is

$$\begin{aligned}\langle A(t)B\rangle = \frac{1}{Z}\sum_s \frac{N_s}{N_r}\sum_r^{N_r}\sum_{ijl}^{M} & \mathrm{e}^{-\frac{1}{2}\beta(\varepsilon_i^{(r)}+\varepsilon_l^{(r)})}\mathrm{e}^{-\mathrm{i}(\tilde{\varepsilon}_j^{(r)}-\frac{1}{2}(\varepsilon_i^{(r)}+\varepsilon_l^{(r)}))t} \\ & \langle r|\psi_l^{(r)}\rangle\langle\psi_l^{(r)}|A|\tilde{\psi}_j^{(r)}\rangle\langle\tilde{\psi}_j^{(r)}|B|\psi_i^{(r)}\rangle\langle\psi_i^{(r)}|r\rangle\end{aligned} \tag{2.52}$$

In order to span the relevant subspace of the Hilbert space, we now choose initial vectors $|\tilde{\phi}_0^{(r,i)}\rangle \propto B|\psi_i^{(r)}\rangle$ for the second Lanczos run. With M such second Lanczos runs, the numerical effort would be much higher than for FTLM. For low temperatures, it can be reduced, since only the low lying states contribute to the expectation values. We consider only states below a cutoff energy E_{cut}, defined by

$$\mathrm{e}^{-\beta_{\mathrm{cut}}(E_{\mathrm{cut}}-E_0)} < \varepsilon_{\mathrm{cut}}, \tag{2.53}$$

where $\varepsilon_{\mathrm{cut}}$ defines the accuracy of the approximation, β_{cut} is the minimal inverse temperature considered and the calculation will be accurate for all $\beta > \beta_{\mathrm{cut}}$.

We thus proceed as follows. For each random start vector $|r\rangle$, we perform an initial Lanczos run with M iterations. For each of the M_{cut} states $|\psi_i^{(r)}\rangle$ with energies below E_{cut}, we then calculate an initial vector $|\tilde{\phi}_0^{(r,i)}\rangle \propto B|\psi_i^{(r)}\rangle$ and perform a second run with M Lanczos iterations, obtaining an approximate eigenbasis $|\tilde{\psi}_j^{(r,i)}\rangle$. Using these basis sets, the final form of LTLM is the same as Eq. (2.50) and Eq. (2.52), with $\sum_{i,l}^{M}$ and $|\tilde{\psi}_j^{(r)}\rangle$ replaced by $\sum_{i,l}^{M_{\mathrm{cut}}}$ and $|\tilde{\psi}_j^{(r,i)}\rangle$, respectively. Note that the sum over j still runs from 1 to M and is not affected by the cutoff.

Memory requirements of our method are the same as for standard FTLM, but the CPU time requirements differ significantly. CPU time is mainly determined by the number of matrix elements that have to be calculated. In the case of static expectation values these are M for FTLM and M_{cut}^2 for LTLM for each random vector. Therefore both methods reach equivalent CPU time requirements per random vector when $M_{\mathrm{cut}} \approx \sqrt{M}$.

For dynamical correlation functions, the number of matrix elements to be calculated in the second Lanczos run is M^2 for FTLM and M_{cut}^2 for LTLM. For LTLM we have to perform M_{cut} second Lanczos runs, but only one for FTLM. Thus we have similar CPU time requirements per random vector for both methods when $M_{\mathrm{cut}} \approx M^{\frac{2}{3}}$.

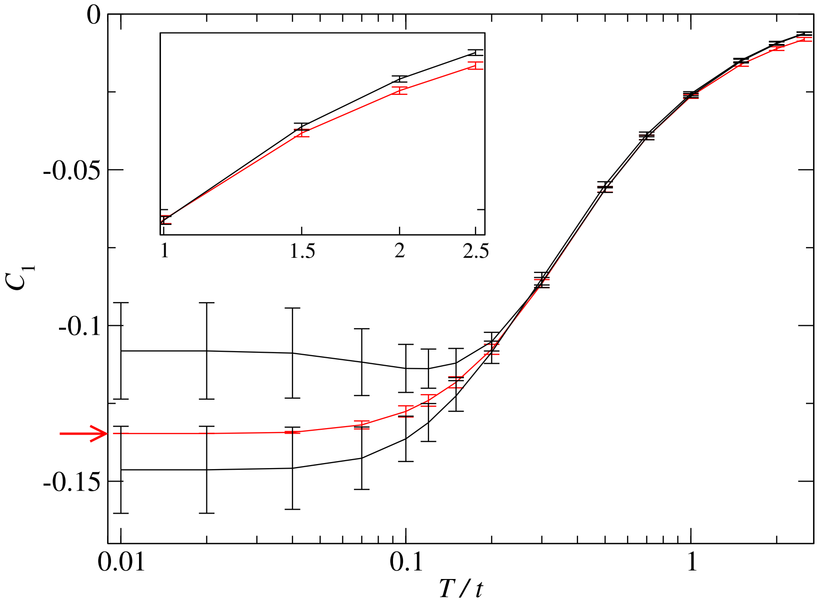

Figure 2.7.: Spin correlation function $C_1 = \langle S_i^z S_{i+1}^z \rangle$ for the 1D Hubbard model on a 12 site chain with periodic boundary conditions at $U = 8t$ and $n = 1$. Red: LTLM with $\beta_{\text{cut}} = 1$, $\varepsilon_{\text{cut}} = 0.01$, $M = 100$, and $N_r = 25$. Black: Two independent runs of FTLM with $M = 100$ and $N_r = 25$. The red arrow marks the result from the $T = 0$ Lanczos method. Inset: Deviation of C_1 in the high temperature region beyond β_{cut}. Here $N_r = 50$ in both cases.

In the limit $T \to 0$ we have $M_{\text{cut}} = 1$, and for $R = 1$ LTLM is comparable to the ground-state Lanczos technique.

For both methods, CPU-time is proportional to R, the number of random vectors. But, by design, far less random vectors are needed for the LTLM than for the FTLM at low temperatures for a given accuracy.

For a demonstration of the method we calculate static and dynamical properties of the one dimensional Hubbard model with Hamiltonian given by Eq. (2.13). As an example we calculate the static spin correlation function $C_1 = \langle S_i^z S_{i+1}^z \rangle$ on a 12 site chain with periodic boundary conditions at half filling ($n = 1$, $\mu = U/2$). The number of basis states for this problem is $N = 2\,704\,156$. Symmetry sectors are specified by momentum $\boldsymbol{k}$ and total spin S^z, where the largest sector $S^z = \pm 1$ has $52\,272$ basis states. The sector $S^z = 0$ is further reduced due to spin up/down symmetry.

In Figs. 2.7 and 2.8 the convergence and statistical errors of LTLM and FTLM are compared at equal computational effort, with $N_r = 25$ random samples per symmetry sector each, corresponding to sampling of $\frac{N_r}{N_s} \approx 0.05\%$ of the largest Hilbert subspace. At low temperatures, our method provides results which are orders of magnitude more precise than from standard FTLM, and which connect smoothly to the ground state

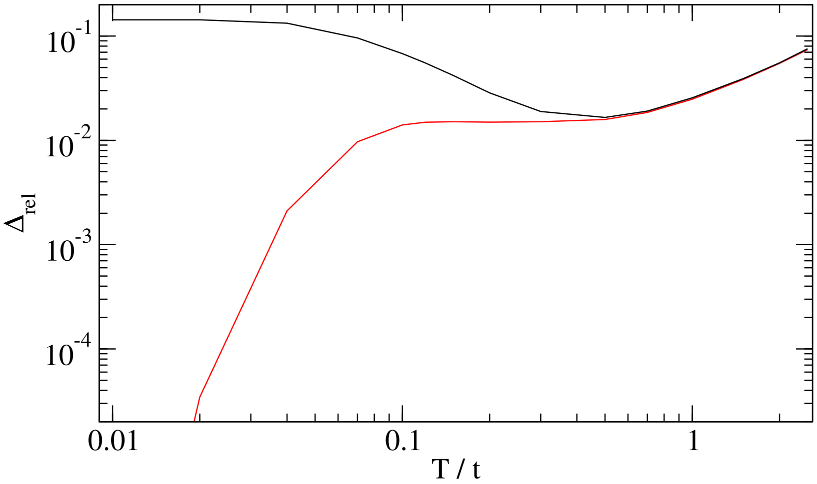

Figure 2.8.: Relative statistical errors $\frac{\Delta C_1}{C_1}$ of LTLM (red) and FTLM (black) with $N_r = 25$ in both cases. Other parameters as in Fig. 2.7. The error of LTLM at $T = 0.01t$ is $\Delta_{\text{rel}} = 10^{-8}$.

properties. We checked that for larger N_r, there is no systematic drift for either method, and the FTLM results converge towards those of LTLM. At intermediate temperatures, the statistical errors of LTLM increase and become similar to those of FTLM. Finally, considerably beyond the chosen cutoff-temperature $1/\beta_{\text{cut}}$, LTLM is no longer applicable, and begins to show a systematic deviation.

Both FTLM and LTLM provide results for a range of temperatures from a single calculation. For FTLM this range is limited towards low temperatures by statistical errors. For LTLM, it is limited by the chosen cutoff-temperature $1/\beta_{\text{cut}}$. Therefore a combination of both methods provides precise results for all temperatures with moderate effort.

As an example of dynamical correlation functions we calculate the regular part of the optical conductivity, given by the current-current correlation function

$$\sigma^{\text{reg}} = \frac{1 - \mathrm{e}^{-\beta\omega}}{\omega} \mathrm{Re} \int_0^\infty \mathrm{d}t \, \mathrm{e}^{\mathrm{i}\omega t} \langle j(t) j \rangle,$$

with the current operator $j = \mathrm{i}t \sum_{i,\sigma} (c^\dagger_{i\sigma} c_{i+1,\sigma} - \text{H.c.})$. In Fig. 2.9, we show results with approximately the same CPU time for both methods. Slightly above the ground state, at $\beta = 40$, LTLM approaches the exact ground state result [40, 41]. For intermediate temperatures $\beta = 10, 5, 3$, slight statistical fluctuations occur. By comparison to FTLM we see that $\beta = 1 < \beta_{\text{cut}}$ is indeed beyond the validity of this calculation. We also checked the accuracy of the results by using $M = 200$ Lanczos steps instead of $M = 100$ yielding the same LTLM spectra within statistical errors.

In contrast, FTLM suffers from strong statistical fluctuations at small temperatures. Errorbars are very large and regions occur where $\sigma^{\text{reg}}(\omega)$ becomes negative, a

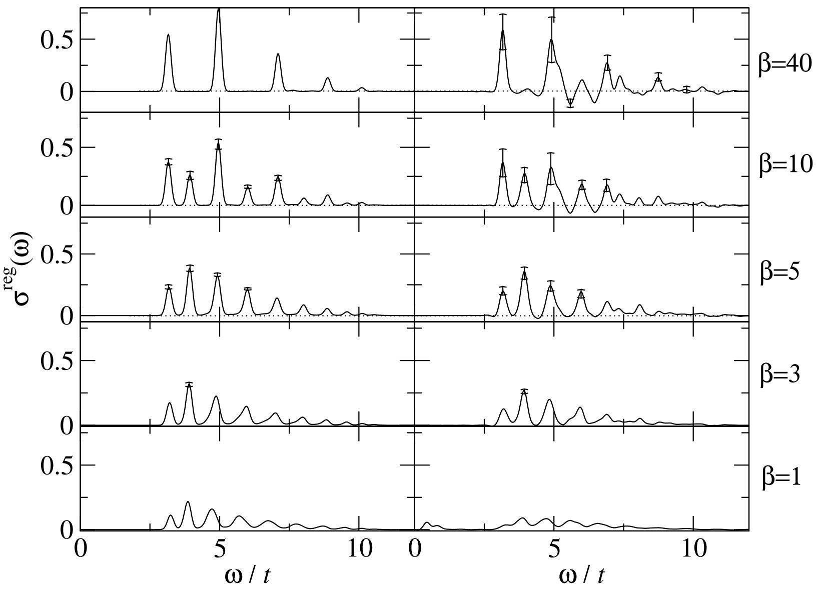

Figure 2.9.: Regular part of the optical conductivity of the 1D Hubbard model on a 12 site chain with periodic boundary conditions at $U = 6t$ and $n = 1$. Left panel: LTLM calculations with $\beta_{\mathrm{cut}} = 3$, $\varepsilon_{\mathrm{cut}} = 0.01$, and $N_r = 40$. Right panel: FTLM calculations with $N_r = 50$. Number of Lanczos steps $M = 100$ and additional broadening of $\eta = 0.1$. Dots mark the zero line. Only selected errorbars are shown. For curves without errorbars, the errors are smaller than the line width.

clear indicator that we did not use enough random vectors for FTLM. As expected from our consideration of static expectation values, errorbars of FTLM get smaller for higher temperatures. As for LTLM we did calculations with $M = 200$, yielding the same curves within errorbars but leading to a better convergence at the high frequency side of the spectrum.

To sum up the LTLM gives an accurate connection of the exact ground state Lanczos method and the established FTLM. Using LTLM at low and FTLM at higher temperatures makes it possible to calculate static and dynamical properties of strongly-correlated systems from $T = 0$ up to $T = \infty$ with very good accuracy and rather small numerical effort.

3. Cluster Perturbation Theory for Finite Temperatures

The most commonly used method for numerical considerations at finite temperatures are QMC approaches (for a review see Ref. [9]) on finite lattices, since they can naturally be defined for finite temperatures. Because of the finite lattice size, the available $\boldsymbol{k}$-resolution is a priori limited. For this reason it is interesting, whether it is possible to extend the ideas and advantages of CPT to finite temperatures.

The CPT was originally developed for the calculation of the ground state spectral function. However, there is no conceptual limitation to $T = 0$. As can be seen from Eq. (2.3), it is straightforward to investigate the finite temperature Green's function, as far as one can calculate the corresponding cluster Green's function. Therefore one has a certain amount of freedom for choosing an appropriate finite temperature method for the cluster calculations.

Sénéchal *et al.* proposed [4] that one possible way to explore finite temperature properties within CPT is to determine the cluster Green's function by means of QMC. However, one can come up with some disadvantages of this proposal. First of all QMC algorithms have to be formulated in imaginary time τ and cannot work directly on the frequency axis. The reason for this is that otherwise the Suzuki-Trotter decomposition cannot be performed. This implies that at some point of the calculation a continuation to real frequencies has to be done, which is in general an ill-posed problem and requires the Maximum Entropy method. This continuation can either be done right after the calculation of the cluster Green's function ($\boldsymbol{G}'(\tau) \rightarrow \boldsymbol{G}'(\omega)$), or after the application of the CPT equation (2.3) ($\boldsymbol{G}(\tau) \rightarrow \boldsymbol{G}(\omega)$), since the formulation of CPT is not restricted to real frequencies (for this point see also App. A). So far it is not clear at all, whether a CPT algorithm driven by QMC is a productive method. Above all the possible resolution of the Maximum Entropy method is rather poor and has problems resolving finer structures of the spectral function.

Another possibility is to restrict the calculations to very small clusters, e.g., 2×2 clusters, where the determination of *all* eigen states and energies is possible by a full diagonalisation. Of course these small system sizes will have an significant impact on the quality of the Green's function, although the convergence of CPT with the cluster size is rather good in most cases.

In this section we propose the following approach. We apply the FTLM and LTLM

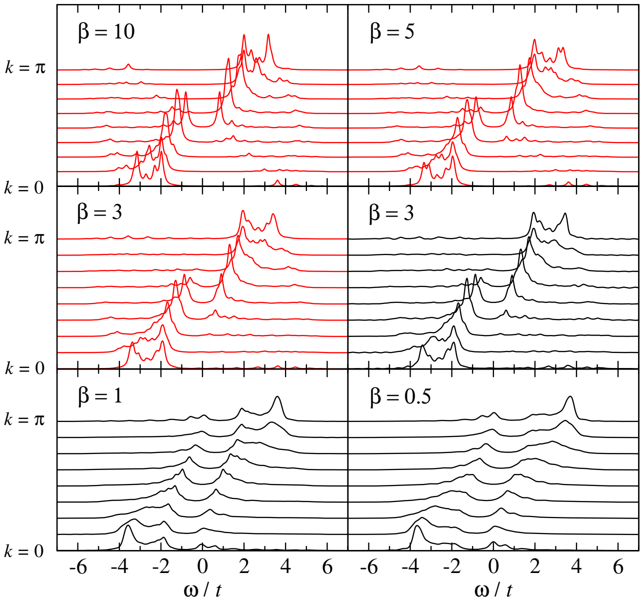

Figure 3.1.: Finite temperature spectral function of the 1D Hubbard model at $U = 4t$, calculated on a 8 site cluster. Red curves: LTLM algorithm. Black curves: FTLM algorithm. Inverse temperatures as indicated in the plots.

algorithms presented in Sections 2.3.3 and 2.3.4 for the calculation of the cluster Green's function. Although the computational burden for these calculations is noticeably higher than for a full diagonalisation, considerably larger cluster sizes ($\sqrt{10}\times\sqrt{10}$) can serve as reference system.

In Fig. 3.1 the spectral function for the 1D Hubbard model at $U = 4t$ is shown. Calculations were done at half filling, where the chemical potential is known ($\mu = U/2$). We used a cluster with $N_\mathrm{c} = 8$ as reference system. For low temperatures, $\beta \geq 3t$, we used the LTLM algorithm with a random sampling of $R = 25$ and $\beta_\mathrm{cut} = 2t$. For higher temperatures the FTLM has been applied with $R = 75$. Using the FTLM for all temperatures shown in Fig. 3.1 would result in very time-consuming calculations, particularly for low temperatures, as described in Sec. 2.3.3. At $\beta = 3t$, both methods provide the same results within error bars (see Fig. 3.1), with reasonable computational effort.

The spectral function at low temperatures, $\beta = 10t$, is very similar to the ground-state result, Fig. 2.2. The width of the peaks becomes a bit larger at $\beta = 5t$, and this effect increases when going to $\beta = 3t$. But note that one still finds a well defined Mott gap, and from the spectral function one can assume that the system is still an insulator.

This behavior changes drastically when going to even higher temperatures, $\beta = 1t$ and $\beta = 0.5t$, as shown in the bottom plots of Fig. 3.1. At $k = \pi/2$ a gap is still visible, but the dispersion of the excitations has changed. For lower temperatures the

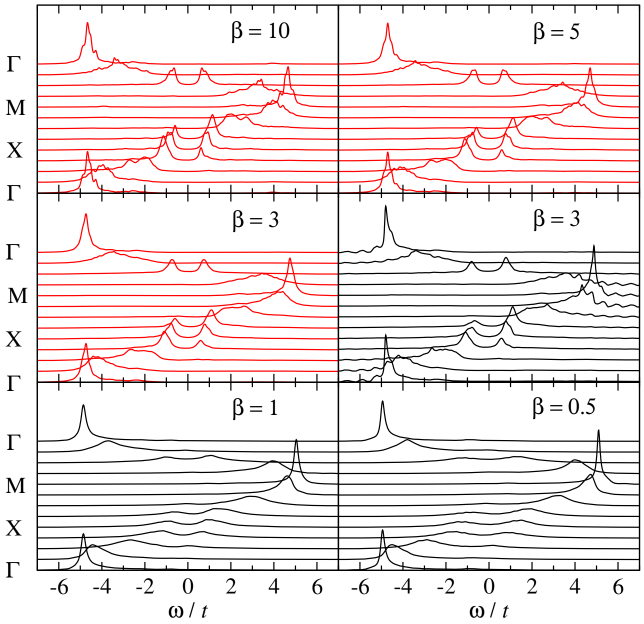

Figure 3.2.: Finite temperature spectral function of the 2D Hubbard model at $U = 4t$, calculated on a $\sqrt{10} \times \sqrt{10}$ cluster. Red curves: LTLM algorithm. Black curves: FTLM algorithm. Inverse temperatures as indicated in the plots.

bands disperse with periodicity π, because of short-range spin correlations manifesting themselves in a doubled unit cell. Now the dispersion has period 2π, similar to the non-interacting dispersion. This behavior can be understood by considering the magnetic super exchange given by $|J| = 4t^2/U = 1$. Hence, at $\beta = 1t$ the thermal fluctuation can break up the spin correlations, and no doubling of the unit cell can be seen.

In Fig. 3.2 we plotted the spectral function of the 2D Hubbard model at $U = 4t$ calculated with a $\sqrt{10} \times \sqrt{10}$ cluster as reference system. The parameters R and β_c were chosen as for 1D. Note that in the results of the FTLM at $\beta = 3t$ small oscillations of the spectral function around the zero line can be seen, which indicates that more random vectors should have been used in the sampling. Nevertheless we get good agreement of LTLM and FTLM at $\beta = 3t$. Similar to the 1D case the peaks become broader with increasing temperature, except of the excitations at $\boldsymbol{k} = (0, 0)$ and (π, π), which we cannot explain so far. An effect in connection with the magnetic super exchange can actually not be seen in our 2D calculations.

To conclude we have shown in this section that it is possible to apply CPT to finite temperatures by applying the FTLM and LTLM algorithms.

4. The Itinerant Antiferromagnet in Two Dimensions

The low-temperature antiferromagnetic (AFM) phase of the 2D Hubbard model at half filling represents an optimal playground to study the strengths and limitations of the V-CPT method for symmetry broken phases. The reason is that both the effects of short-range correlations and long-range antiferromagnetic order manifest themselves in static thermodynamic quantities as well as in the single-particle excitation spectrum.

Different to one dimension, where no long-range AFM phase can be found due to the Mermin-Wagner theorem [42], in two dimensions such a phase is realized at $T = 0$. In this section we will apply the V-CPT in order to study the AFM phase between one and two dimensions [43], and compare results with available previous work.

4.1. Hamiltonian and variational parameters

In this chapter we study the one-band Hubbard model with Hamiltonian

$$H = -t \sum_{\langle ij\rangle,\sigma} (c^{\dagger}_{i\sigma} c_{j\sigma} + \text{H.c.}) + U \sum_{i} n_{i\uparrow} n_{i\downarrow} - \mu \sum_{i} n_{i}. \tag{4.1}$$

Throughout this chapter, t sets the energy scale, and $\mu = U/2$ because of particle-hole symmetry at half filling. For the V-CPT optimization procedure one has to specify a set of variational parameters $\mathbf{\Delta}$, see Sec. 2.2.4. In principle, the "best" result is obtained by using a completely general single-particle term $\mathbf{\Delta}$. However, this would imply the computation of $\Omega(\mathbf{\Delta})$ for a too large number of parameters making the problem numerically impractical. For this reason, it is more convenient to start with a guess of the appropriate physical symmetry-breaking field. For half filling, a good candidate is certainly a staggered field producing a Néel-ordered state. For simplicity, we consider clusters containing an integer number of antiferromagnetic unit cells. With the notation $a = (i, \sigma)$, the corresponding $\mathbf{\Delta}$ has the form

$$\Delta_{a,b} = h \delta_{a,b} z_{\sigma} \mathrm{e}^{\mathrm{i}\boldsymbol{Q}\boldsymbol{r}_a}, \tag{4.2}$$

with $\boldsymbol{Q} = (\pi, \pi)$, $\boldsymbol{r}_a$ the lattice coordinate of the site corresponding to a, $z_{\sigma} = \pm 1$ for $\sigma =\uparrow, \downarrow$, and h the strength of the fictitious staggered field. The optimal value of h

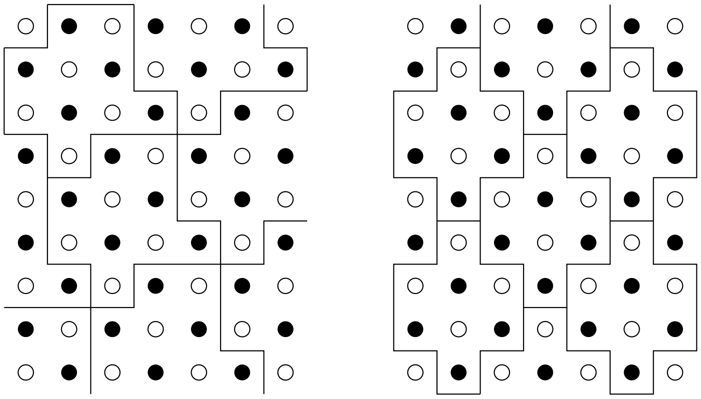

Figure 4.1.: Decomposition of the 2D square lattice into clusters of finite size. Left: $\sqrt{10}\times\sqrt{10}$ cluster. Right: $\sqrt{8}\times\sqrt{8}$ cluster. Full and empty circles denote the staggered order.

will be obtained by minimization $\Omega(\mathbf{\Delta}) \equiv \Omega(h)$. Obviously, $h = 0$ corresponds to the usual CPT approximation. We stress again that via the transformation Eq. (2.23), the staggered field is strictly equal to zero in the original Hamiltonian. It only appears in an intermediate step in the Hamiltonian of the reference system H' to parametrize the trial self-energy. Thus, h is a variational parameter without a direct physical meaning in the original lattice Hamiltonian H and must not be mixed up with a true magnetic field applied to the system. However, it does introduce a true staggered field in the reference (cluster) Hamiltonian H'.

For the numerical calculations we first considered a decomposition of the lattice into $\sqrt{10}\times\sqrt{10}$ clusters as indicated in Fig. 4.1 (left). As discussed in Sec. 2.2.3 obc are used, and the grand potential is evaluated according Sec. 2.2.1. Here a Lorentzian broadening $\omega^+ = \omega + \mathrm{i}\eta$ with finite $\eta = 0.1$ is used. For this choice typically 500 $\boldsymbol{k}$ points are sufficient for convergence of the results. We have checked that the results do not significantly depend on the Lorentzian broadening η.

4.2. Static quantities

The grand potential $\Omega(h)$ has been calculated at $U = 8$ at half filling and $T = 0$. The result is shown in Fig. 4.2. As anticipated, Ω depends on h, and three stationary points are found: a maximum at $h = 0$ and two (equivalent) minima for non-vanishing values $h \approx \pm 0.18$. This means that the interacting system prefers a symmetry-broken state with a non-vanishing staggered magnetization m, as one would have expected physically.

The stationary point at $h = 0$ corresponds to the usual CPT. For $h = 0$ the ground state of a single cluster shows antiferromagnetic correlations but is non-degenerate. Hence, the cluster Green's function and the self-energy are spin independent. This

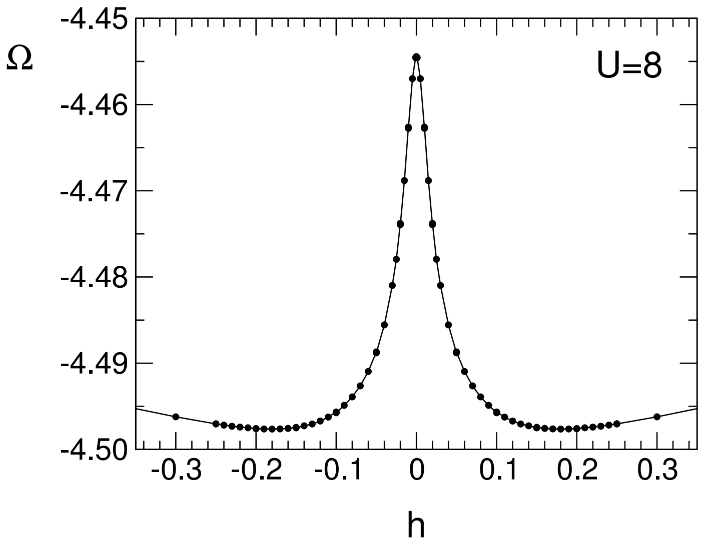

Figure 4.2.: Dependence of the grand potential Ω (per site) on the fictitious staggered field h as obtained by evaluating the self-energy functional. The lattice is decomposed into $\sqrt{10} \times \sqrt{10}$ clusters (see Fig. 4.1). Parameters: onsite repulsion $U = 8$, temperature $T = 0$, half filling. The optimal staggered field is found to be $h = \pm 0.18$.

implies that there is no *coherent* continuation of the antiferromagnetic correlations across the cluster boundaries within the usual CPT. Consequently, the order parameter is $m = 0$. The binding energy per site that is gained by a coherent matching of antiferromagnetic clusters for finite h can be read off from Fig. 4.2 to be $\Delta\Omega \approx 0.043$. This is small as compared to $|J| = 4t^2/U = 0.5$ as there are contributions from bonds connecting different clusters only.

From the value of the grand potential at the optimal field h the ground-state energy is obtained as $E_0 = \Omega + \mu\langle N \rangle$. Fig. 4.3 shows E_0 as a function of U for the respective optimal fictitious field h (V-CPT) and for $h = 0$ (CPT). The results are compared with those of an exact-diagonalization calculation for the isolated cluster with $N_\mathrm{c} = 10$ sites (direct ED). Furthermore, the results of a variational Monte Carlo (VMC) calculation [44] using a Gutzwiller-projected symmetry-broken trial wave function and the results of an auxiliary-field quantum Monte Carlo (QMC) study [45] are displayed for comparison. VMC and QMC data for different cluster sizes N_c are extrapolated [44, 46] to $N_\mathrm{c} = \infty$ (and to $T = 0$, in the latter case).

As compared to the ground-state energy that is obtained by diagonalization of an isolated cluster ("direct ED"), the (usual) CPT result represents a considerable improvement, as can be seen in the figure. Note that CPT (and V-CPT) recover the exact result in the non-interacting limit. The gain in binding energy is due to the (approximate) inclusion of the inter-cluster hopping. A comparison of CPT with

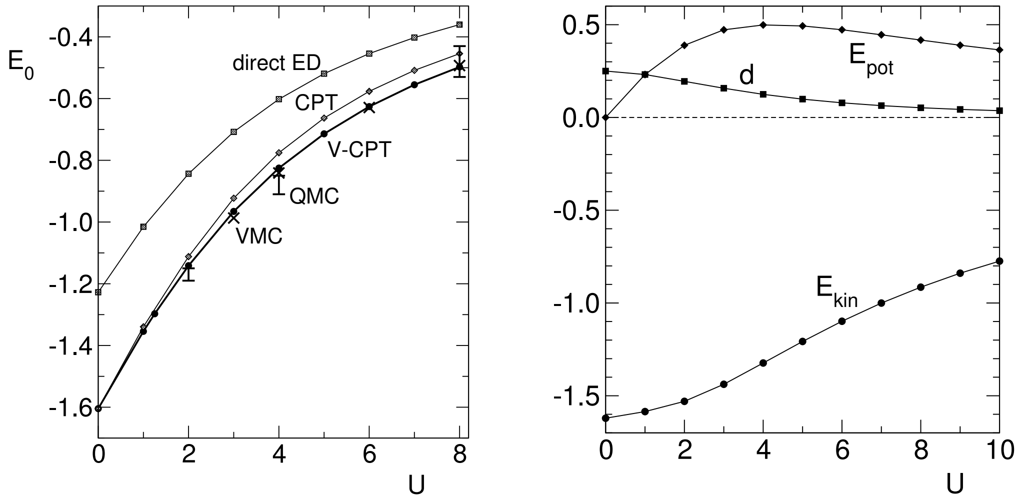

Figure 4.3.: Left: U dependence of the ground-state energy per site E_0 as obtained by different methods: direct ED (squares), usual CPT ($h = 0$, diamonds), and h-optimized V-CPT (circles) for $\sqrt{10} \times \sqrt{10}$ clusters. Variational Monte Carlo results (crosses) [44] and a QMC simulation (error bars) [45] are shown for comparison. VMC and QMC results are extrapolated to $N_\mathrm{c} = \infty$. VMC error bars are smaller than the symbol size. Right: Double occupancy $d = \langle n_{i\uparrow} n_{i\downarrow} \rangle$, potential energy per site $E_\mathrm{pot} = U\,d$, and kinetic energy per site $E_\mathrm{kin} = E_0 - E_\mathrm{pot}$ as functions of U via V-CPT.

Monte-Carlo results (VMC, QMC), however, still shows a sizable discrepancy. On the other hand, our variational CPT method perfectly agrees within the error bars with both Monte-Carlo results for E_0 in the entire U range. This shows that a proper description of long-range order is essential to get the ground-state energy accurately. Note, however, that for the ground state itself and for dynamical quantities, the inclusion of short-range correlations is at least equally important (see below).

Let us discuss a few other static quantities. Fig. 4.3 (right) shows the double occupancy $d \equiv \langle n_{i\uparrow} n_{i\downarrow} \rangle$ as a function of U. The double occupancy is obtained by numerical differentiation of the grand potential $d = \partial\Omega(\mu, U)/\partial U$ (at its respective minimum value). It monotonously decreases from the non-interacting value $d = \langle n_{i\uparrow} \rangle \langle n_{i\downarrow} \rangle = 0.25$ and correctly tends to approach the strong-coupling limit $d = 0$. Already for U of the order of the free band width, a strong suppression of d is found ($d \approx 0.052$ for $U = 8$). This indicates a quick crossover from a Slater-type (itinerant moments) to a Heisenberg-type antiferromagnet (local moments) with increasing U. The potential energy $E_\mathrm{pot} = U\,d$ and the kinetic energy $E_0 - E_\mathrm{pot}$ with $E_0 = \Omega + \mu\langle N \rangle$ and $\mu = U/2$ are shown in addition. Despite the fact that local-moment formation is almost completed for $U = 8$, there is still a considerable kinetic energy $E_\mathrm{kin} \approx -0.915$. This has to be attributed to the residual kinetic exchange.

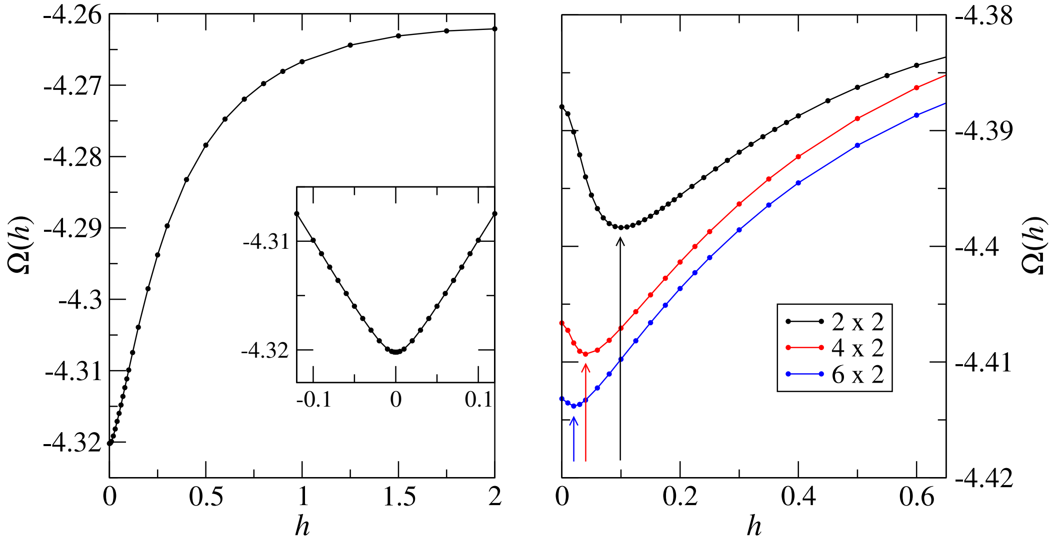

Figure 4.4.: Dependence of the grand potential Ω (per site) on the fictitious staggered field h. Left: Result for the 1D Hubbard model at $U = 8$, $T = 0$ and half filling. Reference system: decoupled set of Hubbard chains with 10 sites each. The inset displays $\Omega(h)$ on a finer scale. Right: Results for the one-dimensional Hubbard ladder. The reference system consists of finite (2×2, 4×2 and 6×2) ladders. Arrows indicate the optimal value of the fictitious staggered field.

4.3. From one to two dimensions

One may ask whether or not the variational procedure always yields an antiferromagnetic state, i.e., also in those cases in which this is not expected physically. For example, an antiferromagnetic state is prohibited in one dimension as quantum fluctuations break up any long-range spin order [47]. Mean-field methods, such as Hartree Fock, however, often yield a Néel state also in one dimension. In a strict mean-field theory, spatial correlations are neglected altogether. Due to the inclusion of short-range correlations, the variational CPT is clearly superior as compared to mean-field theory. For any finite N_c, however, longer-range spatial correlations are neglected. Hence, the V-CPT may be considered as a mean-field approach on a length scale exceeding the cluster dimensions. We therefore expect mild reminiscences of typical mean-field artifacts.

To test this, we have performed calculations for the one-dimensional Hubbard model. The reference system consists of a decoupled set of finite Hubbard chains with N_c sites each. Fig. 4.4 (left) shows the grand potential Ω as a function of the fictitious staggered field h for $U = 8$. As one can see, the minimum of Ω is given by $h = 0$, i.e., the V-CPT predicts the system to be a paramagnet, as expected physically. We

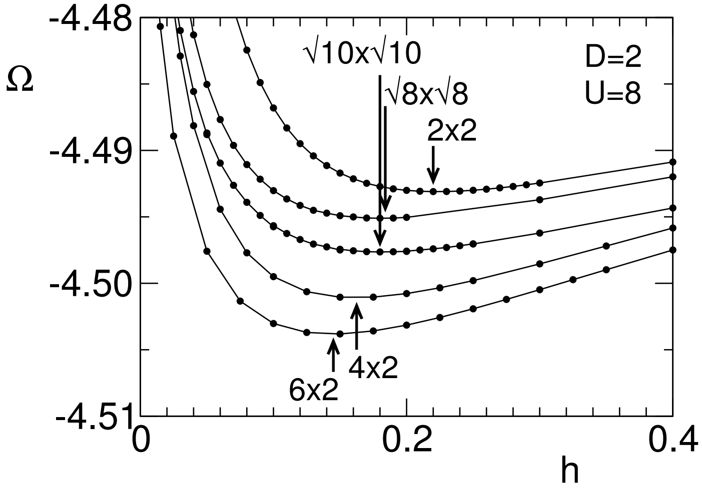

Figure 4.5.: $\Omega(h)$ as in Fig. 4.4 but now coupling the finite ladders (4×2 and 6×2) to a two-dimensional square lattice. Results using the decomposition of the square lattice into 2×2, $\sqrt{8} \times \sqrt{8}$ and $\sqrt{10} \times \sqrt{10}$ clusters are shown for comparison. Arrows indicate the optimal fictitious field.

conclude that for this case quantum fluctuations are taken into account in a sufficient way to prevent the system from becoming antiferromagnetic.

The results are not so straightforward if one considers a one-dimensional two-leg Hubbard ladder. The reference system consists of decoupled finite ladders with N_{rung} rungs, i.e. $N_{\mathrm{c}} = N_{\mathrm{rung}} \times 2$. Results for $N_{\mathrm{rung}} = 2$, $N_{\mathrm{rung}} = 4$ and $N_{\mathrm{rung}} = 6$ are shown in the right plot of Fig. 4.4. Despite of the fact that the system is quasi one dimensional, the calculations predict a finite value for the staggered field and for the staggered magnetization. Clearly, this is an artifact of the remaining mean-field character on a longer length scale. However, we can see from Fig. 4.4 that the optimal value of h rapidly decreases when improving the approximation, i.e., with increasing size of the clusters in the reference system. This is consistent with the fact that no finite magnetization is expected in the $N_{\mathrm{rung}} \to \infty$ limit.

It is interesting to see what happens if one uses the $N_{\mathrm{rung}} \times 2$ ladders in order to build up a true *two*-dimensional system. The results are plotted in Fig. 4.5. In this case, the optimal value of h is much larger than in the right plot Fig. 4.4, and the order parameter (see below) remains finite and depends only weakly on the cluster size. This signals that for the two-dimensional system the antiferromagnetic state is genuine, in contrast to 1D.

Fig. 4.5 also shows the results for the two-dimensional lattice using different “square” clusters, 2×2, $\sqrt{8} \times \sqrt{8}$ and $\sqrt{10} \times \sqrt{10}$ (the latter two clusters are shown in Fig. 4.1). The comparison shows that convergence with respect to the function $\Omega(h)$ is not yet achieved for the largest cluster size considered here. In the limit of very large clusters the SFA becomes formally exact as the trial self-energy $\mathbf{\Sigma}$ is defined to be the

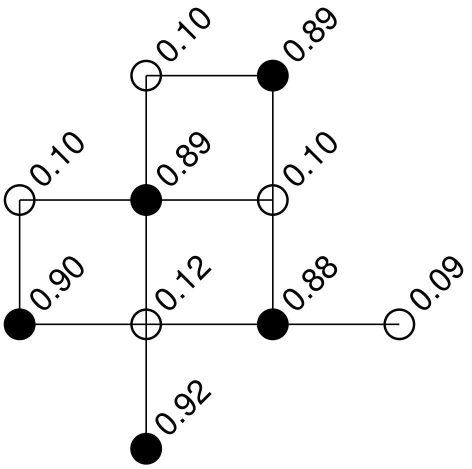

Figure 4.6.: Local average occupation $\langle n_{i\uparrow}\rangle$ for $U = 8$. $\langle n_{i\downarrow}\rangle = 1 - \langle n_{i\uparrow}\rangle$ (not plotted).

exact self-energy of H'. In this limit, we expect the location of the minima ($\pm h_0$) of the function $\Omega(h)$ to go to zero, or the function $\Omega(h)$ to become flat in a region around $h = 0$. The reason is that in the infinite system a finite value for the staggered magnetization will already be produced by an infinitesimally small field.

Note that for the series of 2×2, 4×2, $6 \times 2, \dots$ clusters, the reference system H' does *not* approach the original two-dimensional Hubbard model H.

4.4. Order parameter

While the staggered magnetization m for the one-dimensional ladder system rapidly decreases with cluster size, m remains finite and depends only weakly on the cluster size in case of the two-dimensional system. Differences in m are found to be less than 1-2% for the different cluster geometries considered in Fig. 4.5. A relative difference $\Delta m/m \leq 0.005$ is found when comparing the result for the 10-site and the 8-site clusters. The staggered magnetization is defined as

$$m = \left.\frac{\partial \Omega}{\partial h_{\text{ext}}}\right|_{h_{\text{ext}} \to 0}$$

where h_{ext} is the strength of an external *physical* staggered field (not to be confused with the fictitious field h). Adding a respective field term to the Hamiltonian H and performing the derivative with respect to h_{ext} of the grand potential (at the optimal fictitious field strength h), yields

$$m = \frac{1}{N_{\text{c}}} \sum_{j} \mathrm{e}^{\mathrm{i}\boldsymbol{Q}\boldsymbol{r}_j} (\langle n_{j\uparrow}\rangle - \langle n_{j\downarrow}\rangle),$$

where $\boldsymbol{r}_j$ runs over sites within a cluster, $\boldsymbol{Q} = (\pi, \pi)$, N_c is the number of cluster sites, and

$$\langle n_{j\sigma} \rangle = -\frac{1}{\pi} \lim_{\eta \to 0} \int_{-\infty}^{0} \mathrm{d}\omega \, \mathrm{Im} \; G_{j,j,\sigma}(\omega + \mathrm{i}\eta) .$$

This is the usual expression for the staggered magnetization, but averaged over the cluster. For the two-dimensional Hubbard model at $U = 8$ we find $m \approx 0.80$.

Fig. 4.6 shows the local average occupation $\langle n_{j\uparrow} \rangle$ for the sites j within the $\sqrt{10} \times \sqrt{10}$ cluster for $U = 8$. As any cluster approximation (constructed in real space), the V-CPT necessarily breaks the translational symmetries of the lattice. The approximate self-energy is obtained from a translationally non-invariant reference system which results from the decomposition of the original lattice into decoupled clusters of finite size. This implies that the local Green's function, which is computed from the self-energy using the Dyson equation, and thus the local occupations cannot be expected to be homogeneous (within a sublattice). It is interesting to see, however, that this is not a severe drawback: Fig. 4.6 shows that the variations of the spin-dependent local occupation and the local ordered moment are very moderate within a sublattice.

A much more inhomogeneous state with strongly varying local occupations is obtained when coupling the fictitious field h to two sites within the cluster only. This variant has been considered using the $\sqrt{10} \times \sqrt{10}$ and the $\sqrt{8} \times \sqrt{8}$ clusters. In this case, too, a finite optimal value for h and antiferromagnetic long-range order are found (not shown). The grand potential Ω at the optimal field, however, is considerably larger than in the usual case where h is coupled to all sites within a cluster. This shows that despite the artificial breaking of translational symmetry, a homogeneous state is restored as far as possible.

The U dependence of the staggered magnetization is plotted in Fig. 4.7 in comparison with the VMC results [44] (Gutzwiller-projected symmetry-broken trial wave function) and the results of auxiliary-field quantum Monte Carlo (QMC) [46]. Within the QMC, the order parameter is obtained from simulations of the static spin-spin correlation function at low temperatures. It is assumed that the system effectively behaves as if at $T = 0$ when the thermal correlation length exceeds the cluster dimensions [46]. VMC and QMC data are extrapolated to $N_\mathrm{c} = \infty$ [44, 46].

As one can see from Fig. 4.7, the variational CPT yields a staggered magnetization which strongly disagrees with QMC data. In the Heisenberg limit $U \to \infty$, the V-CPT seems to predict the staggered magnetization to approach unity. On the other hand, physically, one would expect a reduction of the staggered magnetization due to transverse spin fluctuations. In the two-dimensional Heisenberg model, several methods starting from the simplest spin-wave theory up to Monte Carlo methods, predict a reduction of the magnetization to about 60% of its saturated value [49]. On the other hand, the V-CPT agrees well with the results of the variational Monte Carlo study, where transverse spin fluctuations are not fully taken into account as well. Furthermore, there is a very good qualitative agreement with respect to the size

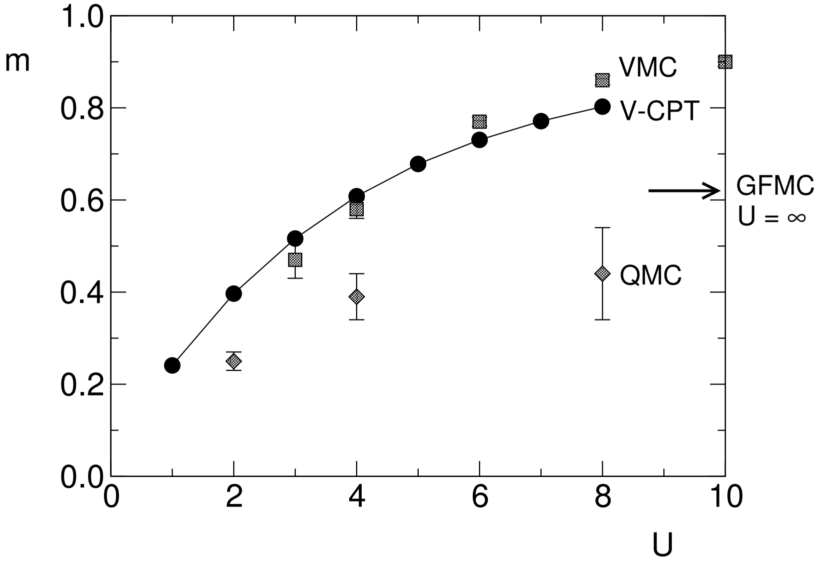

Figure 4.7.: Comparison of the staggered magnetization m as a function of U at half filling obtained by different methods: variational CPT (V-CPT), variational Monte Carlo (VMC) [44] and quantum Monte Carlo (QMC), [46] see text. The arrow indicates the result $m = 0.62 \pm 0.04$ of a Green's-function Monte Carlo study [48] for the two-dimensional Heisenberg model.

of m and the trend of $m(U)$, when comparing with the results of a dynamical mean-field calculation [50] (as the DMFT calculation has been performed for the $D = \infty$ hypercubic lattice, one has to rescale the energies by a factor four to obtain the same variance of the non-interacting density of states which may serve as the energy unit).

This appears to be somewhat surprising since spatial correlations are neglected altogether in the DMFT and also in the VMC calculation where local Gutzwiller projectors are used, while the V-CPT does include the coupling to short-range correlations on the scale of the cluster size. One has to bear in mind, however, that the size of the order parameter is strongly affected by the coupling to *long*-range spin excitations. Recall that in two dimensions and for any finite temperature the Mermin-Wagner theorem [42, 47] shows that antiferromagnetic long-range order is destroyed due to spin waves with wave vector $\boldsymbol{k} \to 0$. Hence, the overestimation of the staggered magnetization could be ascribed to the residual mean-field character of the V-CPT on a length scale exceeding the size of the cluster. This view is also substantiated by our results for the one-dimensional Hubbard ladder which have been discussed above: To achieve a clear suppression of long-range order within the V-CPT, reference systems (finite ladders) as large as 6×2 have been required (Fig. 4.4). This is an indication that in two dimensions a $\sqrt{10} \times \sqrt{10}$ cluster might be to too small to include non-negligible effects of spin excitations on the order parameter.

There is another important point which has to be taken into account in this context:

For a cluster of a given size, an optimal V-CPT calculation should not only consider the fictitious staggered field h but *any* one-particle term in the Hamiltonian of the reference system as a variational parameter. It is in fact reasonable to assume that there is room for improvement: Consider, for example, the hopping between nearest neighbors within the cluster as an additional variational parameter. Actually, this has already been considered in Sec. 2.2.3 for the 1D Hubbard model. There it was found that the optimal intra-cluster hopping is increased as compared to the nearest-neighbor hopping in the original lattice although the effect turned out to be rather weak. Here, the situation is different due to the antiferromagnetic long-range order. In the limit $U \to \infty$, an increased intra-cluster hopping implies an increased effective exchange interaction $|J|$. Assuming the optimal fictitious field h to be unchanged, this tends to *decrease* the order parameter m.

We have performed corresponding calculations which show that a variational adjustment of the intra-cluster hopping at a considerably increased value is very likely in fact. However, for these calculations an extrapolation of the results for Ω to $\eta = 0$ has to be done, because the variation of the hopping increases the impact of the Lorentzian broadening on Ω. After this extrapolation we found a stationary point at $t' = -1.165$, $h = 0.210$. Note that not only the hopping has changed, but also the optimal value of h is shifted to a considerably higher value, compared with $h \approx 0.18$ without optimization of t'. For this reason, the effect of the simultaneous optimization of t' and h on the order parameter is rather weak, and we found $m = 0.78$. We conclude that not only the optimization of additional parameters, but also the inclusion of long range (bosonic) magnons seems to be necessary for a proper description of the order parameter in the large U limit.

4.5. Dynamical quantities

While the V-CPT must be considered as mean-field-like on a length scale exceeding the cluster size, it does account for short-range spatial correlations as the cluster problem is solved exactly. For the two-dimensional Hubbard model at half filling, short-range spin correlations are known to manifest themselves in dynamical quantities such as the local density of states.

Fig. 4.8 shows the spin-dependent local density of states (DOS) $\rho_\sigma(\omega)$ for $U = 8$ which is calculated as a staggered average over the sites in a cluster:

$$\rho_\sigma(\omega) = \frac{1}{N_\mathrm{c}} \sum_j \mathrm{e}^{\mathrm{i}\boldsymbol{Q}\boldsymbol{r}_j} \rho_{j\sigma}(\omega),$$

where $\rho_{j\sigma}(\omega) = (-1/\pi) \lim_{\eta\to 0} \operatorname{Im} G_{j,j,\sigma}(\omega + \mathrm{i}\eta)$. Roughly, the spectrum consists of two broad peaks around $\omega = \pm 5$ and two strong and narrow peaks at about $\omega = \pm 3$. For both the high- and the low-energy excitations a strong spin polarization corresponding to $m \approx 0.80$ is clearly visible. There is also some finite but low spectral weight within

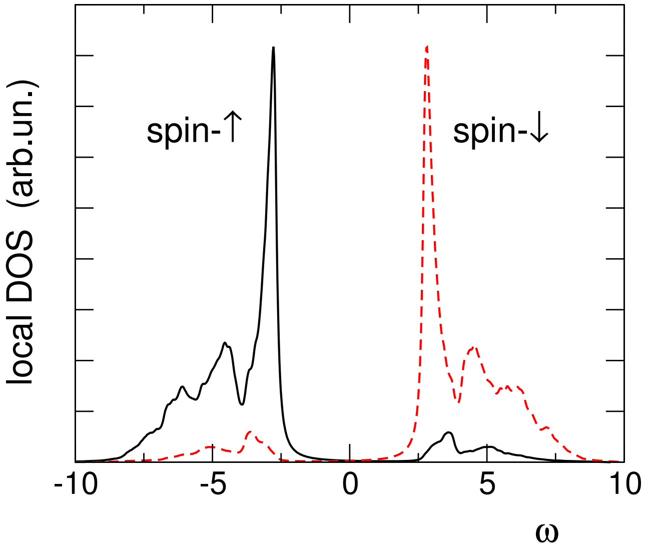

Figure 4.8.: Spin-dependent local density of states (DOS) $\rho_\sigma(\omega)$ (staggered average over the sites in a cluster) obtained for the $\sqrt{10} \times \sqrt{10}$ system via V-CPT for $U = 8$.

the insulating gap which, however, is an artifact of the finite Lorentzian broadening ($\eta = 0.1$).

The high-energy excitations in Fig. 4.8 are interpreted as charge excitations (Hubbard bands). While these are due to local correlations, the low-energy features (at $\omega = \pm 3$) result from (short-range) non-local correlations. The latter will be identified as being due to the coherent propagation of a quasi particle, namely a "spin bag". Physically, this spin bag originates from the frustration induced by the motion of the additional bare hole (electron) in the antiferromagnetic spin background. The different spectral features can easily be identified: The high-energy features are due to the bare particle "rattling around" within the spin bag. This gives rise to an incoherent motion and broad energy bands, i.e., the incoherent lower and upper Hubbard bands with a width set by the energy scale of the bare band width $W = 8$. The low-energy features, on the other hand, correspond to the above-mentioned coherent motion of the spin bag resulting in a strongly renormalized quasi-particle band with a width essentially given by $2|J| = 8t^2/U = 1$.

Note that these peaks are absent in a mean-field approach where off-site correlations are neglected altogether: A recent DMFT study [50] of antiferromagnetic order shows a rather featureless DOS consisting of the two (polarized) Hubbard bands only. Contrary, the effect of antiferromagnetic short-range correlations can be included in a cluster extension of the DMFT. Additional structures appear in the DOS within the dynamical cluster approximation (DCA), for example. Some indications of the mentioned low-energy features can be found by using the non-crossing approximation

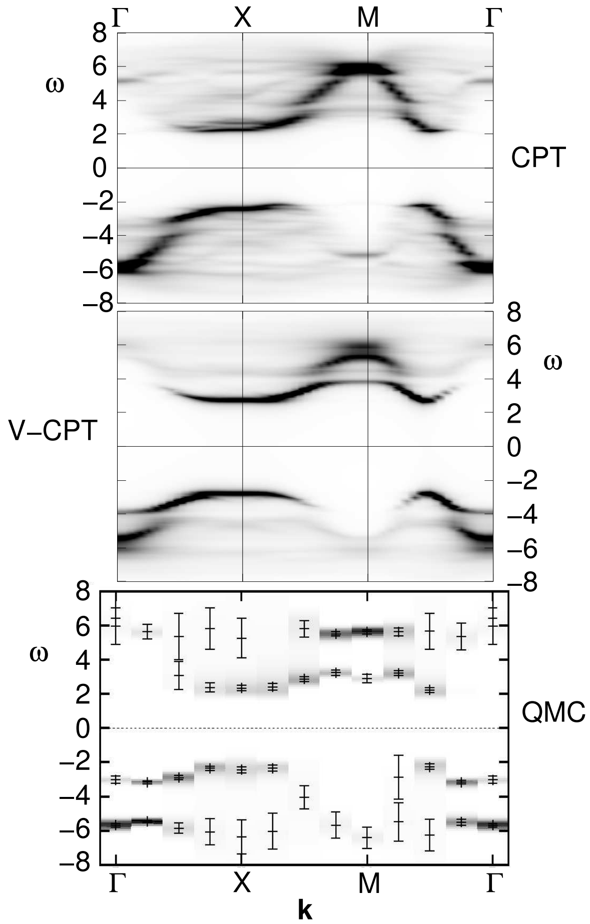

Figure 4.9.: Density plot of the spectral function for the 2D Hubbard model at $U = 8$, half filling and $T = 0$ as obtained by the CPT with $h = 0$ (top) and by the variational CPT with optimal fictitious staggered field $h \neq 0$ (middle). The lattice is covered by $\sqrt{10} \times \sqrt{10}$ clusters. Bottom: QMC (maximum entropy) result, taken from Ref. [52], for the same parameters but for a finite low temperature $T = 0.1$ and an isolated 8×8 cluster. Dark (light) areas correspond to large (small) spectral weight.

(NCA) to evaluate the DCA [51]. For a conclusive interpretation, however, the effects are too weak – probably due to the limited cluster size (a 2×2 cluster in reciprocal space) and the finite temperatures considered.

More elucidating is a comparison of the $\boldsymbol{k}$-resolved spectral density with available results from QMC simulations for isolated but larger clusters. In order to illustrate this point, we have plotted in Fig. 4.9 the spectral function $A(\boldsymbol{k}, \omega)$ for $U = 8$ along high-symmetry directions in the Brillouin zone of the *chemical* lattice. The result is compared with the result from the usual CPT ($h = 0$) and with numerically exact

QMC data from Gröber *et al.* [52] which are available for an $N_\mathrm{c} = 8 \times 8$ isolated cluster and finite but low temperature ($T = 0.1$). The spectral function $A(\boldsymbol{k}, \omega)$ obtained from the maximum-entropy method is shown in Fig. 4.9 (bottom). Since the spin-spin correlation length at $T = 0.1$ considerably exceeds the cluster dimensions, the QMC result can be considered as a good approximation to the $T = 0$ limit. At half filling the spectrum almost exactly respects the constraint $A(\boldsymbol{k}, \omega) = A(\boldsymbol{k} + \boldsymbol{Q}, -\omega)$ with $\boldsymbol{Q} = (\pi, \pi)$ which is predetermined by particle-hole symmetry. This must be considered as a strong check of the numerics. As for the finite system there is no spontaneous symmetry breaking, the spectrum is spin independent and shows perfect translational symmetry with respect to the chemical lattice (pbc have been used).

This must be kept in mind when comparing with the V-CPT. In the V-CPT the real-space Green's function Eq. (2.3), and hence the spectral function

$$A_{\boldsymbol{R},i,\boldsymbol{R}',j,\sigma}(\omega) = -\frac{1}{\pi} \lim_{\eta \to 0} \mathrm{Im}\, G^{\mathrm{ret}}_{\boldsymbol{R},i,\boldsymbol{R}',j\sigma}(\omega + \mathrm{i}\eta),$$

is spin dependent, and translational symmetry holds with respect to the super lattice vectors $\boldsymbol{R}$ only. But the procedure described in Sec. 2.1.2 for obtaining a fully momentum dependent Green's function, Eq. (2.11), implies a spatial average over the cluster sites. Due to this spatial average, the spectral function is spin independent – even in the symmetry-broken state (an *integer* number of antiferromagnetic unit cells are included in a single cluster).

The CPT spectral function is calculated accordingly but for $h = 0$ (Fig. 4.9, top). This means that any signatures of long-range order are switched off in the spectrum, and only short-range correlations (up to the cluster boundaries) are retained. Both, the CPT and the V-CPT result, respect the condition $A(\boldsymbol{k}, \omega) = A(\boldsymbol{k} + \boldsymbol{Q}, -\omega)$ with $\boldsymbol{Q} = (\pi, \pi)$ due to particle-hole symmetry. Note that in both cases the spectral function is defined for any $\boldsymbol{k}$ point in the Brillouin zone, contrary to the "direct" cluster method (QMC).

Roughly, the CPT and the V-CPT spectra appear to be similar but looking at finer structures it is obvious that the CPT predicts a spectral function which is quite different: First, and most important, there is no coherent low-energy band in the CPT spectrum. This shows up when comparing with the V-CPT around Γ for $\omega < 0$ (or around M for $\omega > 0$). In agreement with the QMC result, the V-CPT predicts a dispersive low-energy band which extends continuously with spectral weight from Γ to X and which is clearly separated from the more incoherent feature at higher energies. On the other hand, in the CPT spectrum this is missing. In the $\Gamma - M$ direction the low-energy features turn out to be too broad and are discontinuously split into several branches in the CPT spectrum. The dispersion around X is at variance with the QMC data. Finally, at higher excitation energies, several weak and almost dispersionless bands can be found in the CPT spectrum while in the V-CPT there is a comparatively smooth incoherent background. We conclude that the variational procedure is crucial to achieve a qualitatively correct reproduction of the single-particle excitation spectrum and of the coherent quasi-particle band in particular.

The physical reason is as follows. From previous QMC studies [52] it is well known that the quasi-particle band is the dispersion of a spin bag, i.e., an additional hole (electron) which is dressed by the local distortions of the spin order that are produced by the motion of the hole in the antiferromagnetic background. Since the linear extension of the spin bag is about 3-4 sites only, this picture is already captured by an exact diagonalization of an isolated small cluster. However, the emergence of a coherent band requires more, namely a coherent motion of the spin bag on a larger length scale. This is captured in the QMC results for a large cluster of 8×8 sites. Of course, the perturbative treatment of the inter-cluster hopping within the CPT framework carries out a part of the job. This results in a string dispersion in the V-CPT spectrum with a bandwidth of about $2|J| = 8t^2/U = 1$ as can be read off from Fig. 4.9. Also for the plain CPT the perturbative coupling of the clusters works into the right direction: Although the spectrum more or less consists of a two-band structure, there is a tendency towards the formation of a gap within each of the two bands, i.e., a coherent band *tends* to split off. Within the plain CPT, however, the motion of the dressed hole cannot be completely coherent as there is no definite alignment of spins across the cluster boundary. Upon reaching the cluster edge, the spin bag encounters a misaligned spin with 50% probability and is partly reflected back inside the cluster. This partial loss of coherence explains the several bands at higher energies in the CPT spectrum which are absent in the V-CPT. The variational generalization of the CPT cures this problem by ordering spins antiferromagnetically with the help of the fictitious staggered field not only within but also across the cluster boundaries thereby allowing the coherent spin-bag propagation.

5. Charge Ordering in the 1D and 2D Extended Hubbard Model

Realistic models that are used for the investigation of strongly-correlated electron systems consist of a kinetic part which accounts for the electron motion and an interaction part which is of the same order of magnitude. The simplest model that can be constructed under these assumptions is the tight-binding Hubbard model. It consists of a kinetic energy part, where the electrons can only hop between nearest neighbor sites and the Coulomb interaction U which acts only locally on each site. Although this model was used with great success for the description of a wide class of materials, there are interesting physical questions which require an extension. The inclusion of the nearest-neighbor Coulomb interaction, for example, is necessary for the study of inhomogeneous phases, such as the charge-density wave (CDW) phase. This leads to the so called extended Hubbard model (EHM).

So far a consistent formulation of the V-CPT presented in Sec. 2.2 could be achieved for lattice models with on-site interactions only. The reason for this restriction is that within the SFA the reference system must be chosen to have the same interaction as the original model. In case of the EHM the interaction couples the different sites of the lattice. Thus, there is no reference system with the same interaction which consists of decoupled subsystems of finite size.

In this chapter we extend the ideas of the CPT and V-CPT to the investigation of the EHM including nearest-neighbor Coulomb interaction. It is shown that a mean-field decoupling of the inter-cluster nearest-neighbor interaction yields a systematic and reliable cluster approach [53].

5.1. Decoupling the clusters

We start from the Hamiltonian of the extended Hubbard model

$$\begin{aligned} H = & \sum_{ij,\sigma} T_{i,j} c^{\dagger}_{i\sigma} c_{j\sigma} + U \sum_{i} n_{i\uparrow} n_{i\downarrow} \\ & + V \sum_{\langle ij \rangle} n_i n_j - \mu \sum_{i} n_i, \end{aligned} \tag{5.1}$$

where i, j indicate the position in the lattice, and for convenience we use a constant value $V_{i,j} \equiv V$ for all nearest-neighbor bonds. According to Eq. (2.1) we decouple the lattice into clusters yielding

$$\begin{aligned} H = &\sum_{\boldsymbol{R}} \left[H_0^{(\mathrm{c})}(\boldsymbol{R}) + H_{\mathrm{U}}(\boldsymbol{R}) + H_{\mathrm{V}}^{(\mathrm{c})}(\boldsymbol{R}) \right] \\ &+ \sum_{\boldsymbol{R},\boldsymbol{R}'} \left[H_0^{(\mathrm{i})}(\boldsymbol{R},\boldsymbol{R}') + H_{\mathrm{V}}^{(\mathrm{i})}(\boldsymbol{R},\boldsymbol{R}') \right], \end{aligned} \tag{5.2}$$

where the first row includes only terms of a single cluster and the second row couples different clusters. By comparing the second row with the corresponding term in Eq. (2.1) one can see that the term causing problems in the case of the EHM is the interaction term

$$H_V^{(\mathrm{i})}(\boldsymbol{R},\boldsymbol{R}') = V \sum_{[ij]} n_{\boldsymbol{R}i} n_{\boldsymbol{R}'j}, \tag{5.3}$$

which is of two-particle type. The symbol $[ij]$ indicates that the sum runs only over bonds connecting nearest neighbors in *different* clusters. For nearest-neighbor interactions this means that the indices $[ij]$ must belong to the cluster boundaries of two adjacent clusters. For the application of the method derived in Sec. 2.2 the coupling term must be of single-particle type, which can be achieved by a mean-field decoupling of the interaction term, Eq. (5.3). Hence we get

$$\begin{aligned} H_{\mathrm{V,MF}}^{(\mathrm{i})}(\boldsymbol{R},\boldsymbol{R}') = &V \sum_{[ij]} \left[n_{\boldsymbol{R}i} \langle n_{\boldsymbol{R}'j} \rangle + \langle n_{\boldsymbol{R}i} \rangle n_{\boldsymbol{R}'j} \right] \\ &- V \sum_{[ij]} \langle n_{\boldsymbol{R}i} \rangle \langle n_{\boldsymbol{R}'j} \rangle. \end{aligned} \tag{5.4}$$

Due to the translational invariance with respect to the superlattice vector $\boldsymbol{R}$, the mean-field parameters $\langle n_{\boldsymbol{R}i} \rangle$ and $\langle n_{\boldsymbol{R}'j} \rangle$ are independent of $\boldsymbol{R}$ and $\boldsymbol{R}'$ and will be denoted by λ_i and λ_j, respectively. With these abbreviations we get

$$\begin{aligned} &\sum_{\boldsymbol{R},\boldsymbol{R}'} H_{\mathrm{V,MF}}^{(\mathrm{i})}(\boldsymbol{R},\boldsymbol{R}') = \\ &\quad = V \sum_{\boldsymbol{R},\boldsymbol{R}'} \sum_{[ij]} \left[n_{\boldsymbol{R}i} \lambda_j + n_{\boldsymbol{R}'j} \lambda_i - \lambda_i \lambda_j \right] \\ &\quad = V \sum_{\boldsymbol{R}} \sum_{[ij]} \left[n_{\boldsymbol{R}i} \lambda_j + n_{\boldsymbol{R}j} \lambda_i - \lambda_i \lambda_j \right] \\ &\quad = \sum_{\boldsymbol{R}} H_{\mathrm{V,MF}}^{(\mathrm{i})}(\boldsymbol{R}). \end{aligned} \tag{5.5}$$

The double sum over $\boldsymbol{R}$ and $\boldsymbol{R}'$ reduces to a single sum, because for fixed values of $\boldsymbol{R}$, i, and j only one term of the sum over $\boldsymbol{R}'$ contributes due to the fact that two-site interactions couple at most two different clusters. One has to be careful in order to avoid double counting of the bonds $[ij]$. For instance, for a one-dimensional cluster of length N, Eq. (5.5) reduces to

$$V \sum_{\boldsymbol{R}} \left[n_{\boldsymbol{R}1} \lambda_N + n_{\boldsymbol{R}N} \lambda_1 - \lambda_1 \lambda_N \right], \tag{5.6}$$

because the only decoupled bond connects sites 1 and N of different clusters.

By this mean-field decoupling, two parameters λ_i are introduced for each decoupled bond, e.g. λ_1 and λ_N in one dimension, and in general all these parameters λ_i are independent of each other. But as we will see below, the number of mean-field parameters λ_i can be strongly reduced in special cases.

The decoupled interaction, Eq. (5.5), is of single-particle type and can be included in the intra-cluster hopping term $H_0^{(\mathrm{c})}(\boldsymbol{R})$, leading to a modified intra-cluster single-particle term

$$\tilde{H}_0^{(\mathrm{c})}(\boldsymbol{R}, \lambda_i) = H_0^{(\mathrm{c})}(\boldsymbol{R}) + H_{\mathrm{V,MF}}^{(\mathrm{i})}(\boldsymbol{R}, \lambda_i), \tag{5.7}$$

where we explicitly denoted the dependence on the parameters λ_i. After this mean-field decoupling we finally get the Hamiltonian

$$\begin{aligned} H_{\mathrm{MF}}(\lambda_i) = &\sum_{\boldsymbol{R}} \left[\tilde{H}_0^{(\mathrm{c})}(\boldsymbol{R}, \lambda_i) + H_{\mathrm{U}}^{(\mathrm{c})}(\boldsymbol{R}) + H_{\mathrm{V}}^{(\mathrm{c})}(\boldsymbol{R}) \right] \\ &+ \sum_{\boldsymbol{R}, \boldsymbol{R}'} H_0^{(\mathrm{i})}(\boldsymbol{R}, \boldsymbol{R}'), \end{aligned} \tag{5.8}$$

for which the method described in Sec. 2.2 is applicable.

From the decoupling of the clusters we have got additional parameters λ_i which are external parameters to the Hamiltonian Eq. (5.8) and have to be determined in a proper way. For this purpose we propose two different procedures:

(i) One can get the parameters from a self-consistent calculation on an isolated cluster. That means that one starts with a certain guess for the λ_i, which are the expectation values of the electron density on sites i. Then the ground-state wave function of an isolated cluster is calculated, giving new values for the λ_i. In this step open boundary conditions (obc) are used in order to be consistent with the obc necessary for the calculation of the cluster Green's function in Eqs. (2.3) and (2.15). These new values λ_i serve as parameters in the Hamiltonian for the next determination of the ground state, and the whole procedure is iterated until convergence of the λ_i is achieved. This procedure may work quite well for the EHM in the case of a first order phase transition between a disordered and an ordered phase, because (due to an avoided level crossing) the transition point, i.e. the critical Coulomb interaction V_c, is almost independent of the cluster size [54]. For second order phase transitions we expect that this method will not give satisfactory results, because here we face a discrepancy between the parameters calculated on the isolated cluster and the parameters that would give the optimal result in the thermodynamic limit.

(ii) The shortcoming in the case of second order phase transitions can be overcome in the following way. As we show in App. C, the self-consistent calculation of mean-field parameters is equivalent to the minimization of the free energy F. Since the relation $\Omega = F - \mu N$ holds at $T = 0$, this minimization can be done at the same time as the optimization of the single-particle parameters $\boldsymbol{\Delta}$ in the SFA formalism, and we can use Eq. (2.15) for the determination of the parameters λ_i, too. Note that all quantities in Eq. (2.15) which depend on the single-particle parameters $\boldsymbol{\Delta}$ are dependent on the mean-field parameters λ_i as well. To keep the calculations simple we consider only half-filled systems, where it is sufficient to use only two different values for the λ_i, namely $\lambda_A = 1 - \delta$ and $\lambda_B = 1 + \delta$ on sublattices A and B, respectively. Under this assumption we have only one mean-field parameter δ, and the grand potential is $\Omega = \Omega(\boldsymbol{\Delta}, \delta)$. The general procedure is now that for each value of δ the stationary point with respect to $\boldsymbol{\Delta}$ has to be found as required by the SFA formalism, yielding a function $\Omega = \Omega(\delta)$. By finding the minimum of this function one can determine the optimal value for δ.

Conceptually, the latter method (ii) of determining the mean-field parameters is superior to the procedure (i) described first as it uses information on the Green's function in the thermodynamic limit for the calculation of δ. However, one has to keep in mind that for each choice of δ the Green's function $\boldsymbol{G}'(\omega)$ of the isolated cluster has to be calculated many times to evaluate Eq. (2.15) which is much more time consuming than the self-consistency procedure on the isolated cluster.

5.2. Results for one dimension

The Hamiltonian of the one-dimensional EHM is given by

$$\begin{aligned} H = &- t \sum_{i,\sigma} \left(c^\dagger_{i,\sigma} c_{i+1,\sigma} + \text{H.c.} \right) + U \sum_i n_{i\uparrow} n_{i\downarrow} \\ &+ V \sum_i n_i n_{i+1} - \mu \sum_i n_i . \end{aligned}$$

Throughout this chapter we set t as the unit of energy. Although this model has been studied intensively [45, 54–70], the ground-state phase diagram is still under some discussion. We use this model as a testing ground for our method, because many results are available for comparison. The chemical potential is $\mu = U/2 + 2V$ due to particle-hole symmetry at half filling.

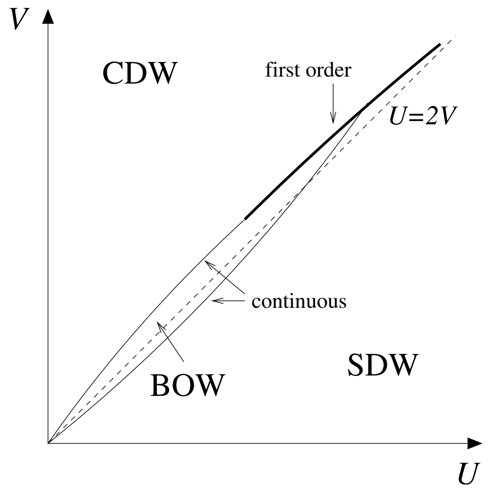

Figure 5.1.: Schematic phase diagram of the one-dimensional EHM, following Ref. [55]. Similar phase diagrams have been reported in Refs. [54, 57–59, 61, 70], but with different extensions of the BOW phase in the U-V-plane. The thick line marks the first-order phase transition, and the dashed line marks $U = 2V$.

In one dimension at half filling, the phase diagram of the EHM includes spin density wave (SDW) and charge density wave (CDW) phases. By weak-coupling renormalization-group (RG) techniques ("g-ology") [62, 63] the phase boundary between SDW and CDW phase was determined to $U = 2V$, which actually coincides with strong-coupling calculations for large U and V using second-order perturbation theory [62, 64]. For intermediate coupling the boundary was found to be shifted from the $U = 2V$ line, enhancing the SDW phase, shown by QMC calculations [45, 54–56] and strong-coupling calculations up to fourth order [65]. Moreover the nature of the transition is different in the two coupling regions, with a second-order transition at weak coupling and a first-order transition at strong coupling. The multi-critical point, where this change takes place, was investigated intensively in the past. Cannon and Fradkin [66] obtained $U_{\mathrm{m}} \approx 1.5$ by field theoretical techniques, whereas QMC gave $U_{\mathrm{m}} = 3$ [45, 56] and $U_{\mathrm{m}} = 4.7 - 5.5$ [54, 55], respectively. The latter value is in well agreement with results based on bosonization and RG [59, 61, 67]. Other estimations for the multi-critical point are $U_{\mathrm{m}} \approx 3.7$ (DMRG [60]) and $U_{\mathrm{m}} = 3.5 - 5$ from finite-size extrapolations of Lanczos results [68].

Only recently Nakamura [57, 58] has proposed an additional phase between the SDW and CDW phases, the so-called bond order wave phase (BOW). The existence of this phase has afterward been assured by several studies [54, 55, 59–61, 70]. A schematic phase diagram including Nakamura's BOW is depicted in Fig. 5.1. There is good agreement on the existence of the BOW phase, but its extension in the U-V-plane has not yet been clarified in detail.

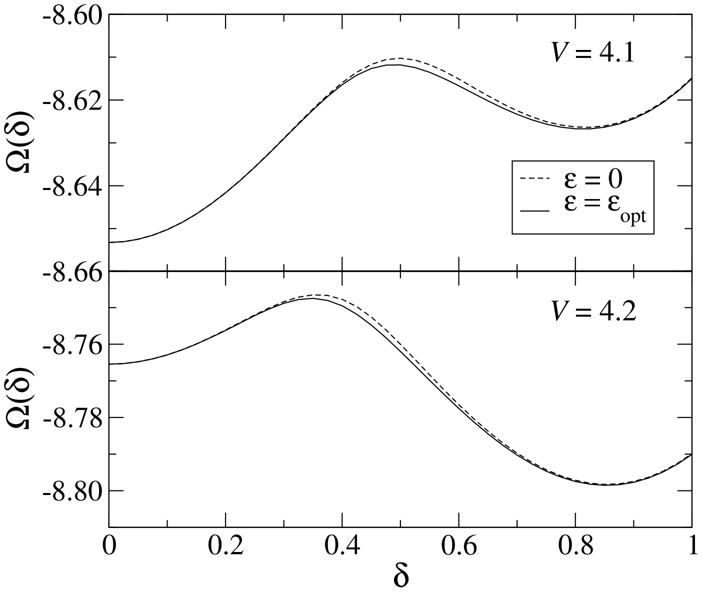

Figure 5.2.: Grand potential Ω as a function of the mean-field parameter δ at $U = 8$ calculated on a cluster with $N_\mathrm{c} = 8$ sites as reference system. Upper panel: $V = 4.1$. Lower panel: $V = 4.2$. Solid lines: With optimization of a staggered field. Dashed lines: Without optimization of a staggered field.

5.2.1. First-order phase transition

For a first test of our method we studied the one-dimensional EHM at $U = 8$, which is well above the multi-critical point. The phase transition is of first order without any BOW phase between SDW and CDW phases. As reference system H' according to Sec. 2.2, we used decoupled clusters of different lengths consisting of $N_\mathrm{c} = 8$, 10, and 12 sites, respectively. For the determination of the mean-field parameter δ we used the method (ii) described in Sec. 5.1, where δ is calculated from the minimum of the free energy of the system. For the SFA optimization of the single-particle parameters, we had to choose a set $\boldsymbol{\Delta}$ of parameters which are varied in the optimization procedure. In order to minimize the number of relevant parameters we use results of Sec. 2.2.3, where it has been shown that at $U = 8$ the variation of the hopping in the cluster yields only minor changes that can be neglected, and that open boundary conditions have to be used. Moreover, for the one-dimensional Hubbard model it has been pointed out in Sec. 4.3 that the use of a fictitious staggered magnetic field as a variational parameter gives a stationary point of the grand potential only for vanishing field, yielding a paramagnetic phase without long-range magnetic order. Since it can be assumed that these results are also valid in a similar way for the EHM, we did not use the hopping in the cluster or a staggered magnetic field in the optimization procedure. Here we studied charge-ordering effects and therefore we used as variational parameter a staggered field coupled to the charge densities given by Eq. (2.24) with

$$\Delta_{a,b} = \varepsilon\delta_{a,b}\mathrm{e}^{\mathrm{i}\boldsymbol{Q}\boldsymbol{r}_a}, \tag{5.9}$$

where $\boldsymbol{Q} = \pi$ is the wave vector of the staggered order, $\boldsymbol{r}_a$ the lattice vector of site a, and ε is the staggered-field strength. The grand potential obtained in this way is shown in Fig. 5.2 at two values of the inter-site Coulomb interaction. For comparison, calculations without optimization of the staggered field are shown as dashed lines in Fig. 5.2. As one can see, the optimization gives only minor changes to $\Omega(\delta)$. The optimal staggered-field strengths in these calculations varied between $\varepsilon_{\mathrm{opt}} = 0.0$ at $\delta = 0.0$ and $\varepsilon_{\mathrm{opt}} \approx 0.05$ at $\delta = 1.0$ at both values of V.

From the shape of $\Omega(\delta)$ one can directly infer the order of the transition. If three minima occur at $\delta = 0$ and $\delta = \pm\delta_{\mathrm{CDW}}$, it is of first order, whereas it is of second order if $\Omega(\delta)$ has only two minima at $\delta = \pm\delta_{\mathrm{CDW}}$ and a maximum at $\delta = 0$. As on can easily see in Fig. 5.2, we have clear evidence for a first-order phase transition at $U = 8$ with an SDW minimum at $\delta = 0.0$ and two degenerate CDW minima at $\delta = \pm\delta_{\mathrm{CDW}}$. At $V = 4.1$ the SDW phase is realized, $\Omega(0) < \Omega(\delta_{\mathrm{CDW}})$, whereas at $V = 4.2$ we have $\Omega(0) > \Omega(\delta_{\mathrm{CDW}})$ and the CDW phase is the stable one. Thus we can state that the critical value V_{c} for the phase transition is located between $V = 4.1$ and $V = 4.2$.

For a more accurate determination of the phase boundary V_{c}, we have calculated the grand potential at several values of V and cluster sizes $N_{\mathrm{c}} = 8$, 10, and 12. In addition to the grand potential and the ground-state energy $E_0 = \Omega + \mu N_e$ with N_e the number of electrons in the system, we calculated the order parameter

$$m_{\mathrm{CDW}} = \frac{1}{N_{\mathrm{c}}}\sum_j \left(n_j - \langle n\rangle\right)\mathrm{e}^{\mathrm{i}\boldsymbol{Q}\boldsymbol{r}_j}, \tag{5.10}$$

where $\boldsymbol{Q} = \pi$, N_{c} is the number of cluster sites, and the kinetic energy E_{kin}. Both properties can be extracted from the spectral function

$$A(\boldsymbol{k},\omega) = -\frac{1}{\pi}\lim_{\eta\to 0}\mathrm{Im}\; G(\boldsymbol{k},\omega + \mathrm{i}\eta) \tag{5.11}$$

and the kinetic energy is given by

$$E_{\mathrm{kin}} = \frac{2}{L}\sum_{\boldsymbol{k}}\int_{-\infty}^{0}\mathrm{d}\omega\, \varepsilon(\boldsymbol{k})A(\boldsymbol{k},\omega), \tag{5.12}$$

with $\varepsilon(\boldsymbol{k})$ the dispersion of the non-interacting system. Within our approach it is necessary to use the Lehmann representation for the cluster Green's function with small but finite Lorentzian broadening η. Whereas the grand potential Eq. (2.15) shows only minor dependence on this broadening, the dependence of the order parameter and the kinetic energy is considerably larger and one has to do an extrapolation to $\eta = 0$

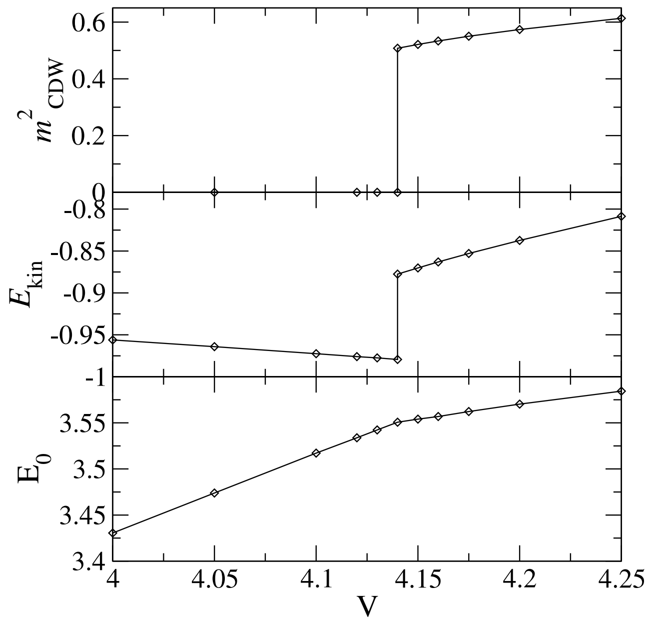

Figure 5.3.: Ground-state energy E_0, kinetic energy $E_{\rm kin}$, and order parameter $m^2_{\rm CDW}$ of the one-dimensional EHM at $U = 8$ after finite-size scaling. Lines are guides to the eye only.

[4]. Although the formalism applies to the thermodynamic limit, results show a finite-size dependence due to the finite size of the clusters serving as reference system. We found that the order parameter exhibits the strongest finite-size effects, which were of the order $m^2_{{\rm CDW},N_{\rm c}=10}/m^2_{{\rm CDW},N_{\rm c}=12} \approx 1.02$ at all values of V. Finite-size scaling to $N_{\rm c} = \infty$ is easily done and the results for the ground-state energy extracted from the minimum of the grand potential, the kinetic energy and the order parameter are shown in Fig. 5.3. Our results should be compared to Fig. 10 of Ref. [54] which shows excellent quantitative agreement with a deviation of less than 2 % for the calculated quantities at all values of V. From our calculations we get $V_{\rm c} = 4.140(5)$, again in agreement with the previous studies Refs. [54, 60].

In order to provide a complete picture of the method we also performed calculations with mean-field parameters obtained by a self-consistent procedure on an isolated cluster, see method (i) in Sec. 5.1. For instance for $N_{\rm c} = 12$ and $V = 4.1$ one finds self-consistent solutions for $\delta = 0$ and for $\delta_{\rm SC} = 0.832$, which differs only slightly from the value extracted from the grand potential, $\delta_{\rm CDW} = 0.822$. For this reason the calculation of the ground-state energy, kinetic energy, and order parameter using $\delta_{\rm SC}$ instead of $\delta_{\rm CDW}$ gives practically the same results as in Fig. 5.3. In the present case it is therefore sufficient to calculate the mean-field parameter from an isolated cluster which is much faster than finding the minimum of the grand potential.

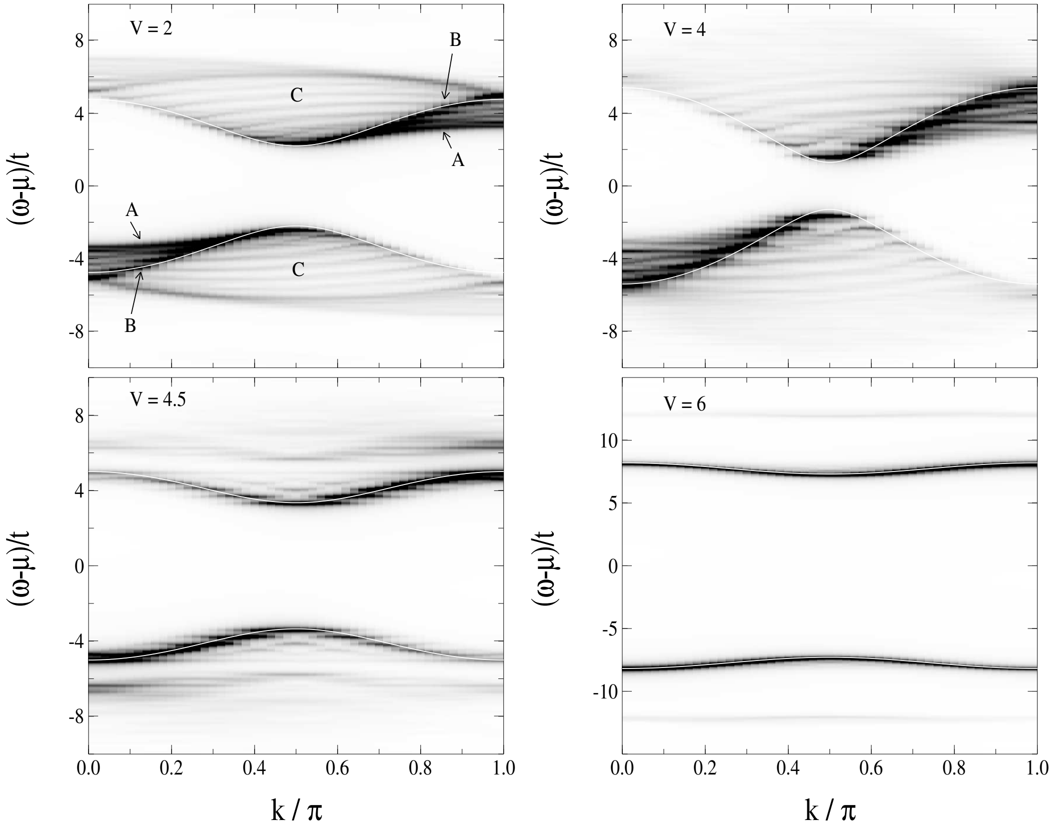

Figure 5.4.: Density plot of the spectral function $A(\boldsymbol{k},\omega)$ of the one-dimensional EHM at $U = 8$, calculated on a cluster of size $N_\mathrm{c} = 12$ with Lorentzian broadening $\eta = 0.1$. Darker regions represent larger spectral weight. Coulomb interaction V as indicated in the plots. White lines are fits to a Hartree-Fock SDW/CDW dispersion (see text).

Spectral function

Whereas the properties we have shown so far are well known for the one-dimensional EHM, we additionally calculated for the first time the spectral function by Eq. (5.11) for arbitrary wave vector $\boldsymbol{k}$. In Fig. 5.4 results are shown at $U = 8$ and selected values of V with a reference system consisting of $N_\mathrm{c} = 12$ cluster sites, and the mean-field parameter δ calculated self-consistently by method (i), see Sec. 5.1. We want to mention that the 'striped' structure, particularly visible in the regions marked by 'C' in Fig. 5.4, occurs because the decoupling into clusters breaks the translational invariance of the system.

The spectral function at $V = 2.0$ is very similar to the spectral function of the Hubbard model ($V = 0$) [3, 4] with splitting of the low-energy band into a spinon and an holon band, which are marked in Fig. 5.4 by 'A' and 'B', respectively. This

Table 5.1.: Fitted values for the hopping matrix element t_{fit}, gap Δ_{fit}, and gap Δ_{HF} of the full Hartree-Fock approximation at $U = 8$. Fitted values from results for the $N_{\mathrm{c}} = 12$ cluster.

	t_{fit}	Δ_{fit}	Δ_{HF}
$V = 0.0$	1.93	2.24	3.75
$V = 2.0$	2.11	2.20	3.75
$V = 4.0$	2.62	1.29	3.75
$V = 4.5$	1.86	3.35	4.80
$V = 6.0$	1.86	7.29	7.88

similarity could have already been expected based on the full Hartree-Fock solution—decoupling of all interaction terms in the Hamiltonian—where one has no dependence on V at all in the SDW phase. But this simple picture holds only away from the transition point V_{c} as can be seen in Fig. 5.4 in the plot for $V = 4.0$. At this point, in the vicinity of the phase transition $V_{\mathrm{c}} = 4.14$, the gap is considerably smaller than at $V = 2.0$, a clear deviation from the Hartree-Fock prediction. This indicates that charge fluctuations become very important in this regime, which are completely neglected by the Hartree-Fock approximation, but are taken into account on the length scale of the cluster in our approach. But although we found this deviation, one can still see residuals of the splitting of the low-energy band, a signature for spin-charge separation. For this reason we infer that spin-charge separation is present up to the transition point. The white lines in Fig. 5.4 correspond to fits of the holon branch to a Hartree-Fock dispersion $E(\boldsymbol{k}) = \pm\sqrt{\Delta^2 + \varepsilon(\boldsymbol{k})^2}$. The fitted values for the hopping matrix element t_{fit} and the gap Δ_{fit} are denoted in Tab. 5.1, where we included the values at $V = 0$ for completeness. One finds that the gap Δ_{fit} is almost constant from $V = 0$ to $V = 2$ and, as mentioned above, considerably decreases near the the phase transition ($V = 4$). The hopping matrix element t_{fit} shows the opposite behavior and increases when approaching the transition point from below. This is due to the fact that in the vicinity of V_{c}, doubly-occupied and singly-occupied sites become close in energy, which enhances the movement of the electrons. The actual value of the matrix element t_{fit} is very large compared to the original value $t = 1$ in the Hamiltonian. A fit to the spinon band would give a smaller value closer to $t = 1$, but whereas fitting to the holon band is consistent over the whole range of momentum vectors $\boldsymbol{k}$, the spinon band is only present for $\boldsymbol{k} < \pi/2$ for $\omega - \mu < 0$ (and $\boldsymbol{k} > \pi/2$ for $\omega - \mu > 0$, respectively).

The spectral function in the CDW phase shows a qualitatively different behavior. At $V = 4.5$ we found a gap considerably larger than in the SDW phase, and this gap increases very fast with increasing V, as can be seen in the plot at $V = 6$. Moreover, no evidence for spin-charge separation can be seen in the spectral functions. Within the full Hartree-Fock approximation, where both the onsite and the nearest neighbor interactions are mean-field decoupled, the gap Δ_{HF} is the solution of the self consistent equation

$$1 = \frac{2\Gamma_\alpha}{N} \sum_{\boldsymbol{k}} \frac{1}{\sqrt{\varepsilon(\boldsymbol{k})^2 + \Delta_{\mathrm{HF}}}},$$

with $\Gamma_{\mathrm{SDW}} = \frac{U}{2}$ and $\Gamma_{\mathrm{CDW}} = \frac{U}{2} - 2zV$ and z the coordination number of the lattice. By comparing the fitted value Δ_{fit} with the Hartree-Fock solution Δ_{HF}, one can see that the agreement at $V = 4.5$ is better than at $V = 4$, and that it becomes still better with increasing V. For this reason we conclude that charge fluctuations, which are neglected in the Hartree-Fock approximation, play a minor role in the CDW phase.

The values for t_{fit} and Δ_{fit} given above are determined by calculations with a $N_{\mathrm{c}} = 12$ cluster as reference system. An analysis of the finite-size dependence of these properties showed that finite-size effects are almost negligible in the SDW phase well below V_{c}. However, in the vicinity of the transition point, these effects increase considerably, especially for Δ_{fit}. For instance, at $V = 4.0$ we found $t_{\mathrm{fit}} = 2.49$ and $\Delta_{\mathrm{fit}} = 1.60$ for the $N_{\mathrm{c}} = 8$ cluster. This means that the values given in Tab. 5.1 underestimate the hopping and overestimate the gap in the vicinity of V_{c}. In the CDW phase, the finite-size effects become smaller again, but are still larger than in the SDW phase (e.g., $t_{\mathrm{fit}} = 1.77$ and $\Delta_{\mathrm{fit}} = 7.38$ for $V = 6$ and $N_{\mathrm{c}} = 8$).

5.2.2. Second-order phase transition

So far all calculations have been done at $U = 8$, where the system shows a first order phase transition. In the following, we study the EHM at $U = 3$, where the model exhibits a second-order transition into the charge ordered CDW phase [54, 60]. In this paper we do not consider the BOW, since it has been argued that the SDW-BOW transition is of Kosterlitz-Thouless type [58]. For an analysis of this type of transition the available cluster sizes are far too small and do not allow a clear distinction between SDW and BOW phase.

We calculate the grand potential $\Omega(\delta)$ in the same way as in Sec. 5.2.1 in order to determine δ. The result of a calculation on a cluster consisting of $N_{\mathrm{c}} = 8$ sites is shown in Fig. 5.5. One can easily see a striking difference between the grand potential at $U = 8$, Fig. 5.2, and at $U = 3$. In the latter case there is only a single minimum and it is located at $\delta = 0$ for $V < V_{\mathrm{c}}$. With increasing V the curve for $\Omega(\delta)$ becomes flatter in the region around $\delta = 0$ and finally two degenerate CDW minima occur at $\delta = \pm\delta_{\mathrm{CDW}}$ for $V > V_{\mathrm{c}}$. Note that here δ changes continuously when crossing V_{c}, whereas it shows a discontinuity in the case of a first-order phase transition.

We find that now it is indeed important to use a staggered field, Eq. (5.9), as a variational SFA parameter. In Fig. 5.5, results are shown with such an optimization (solid lines) and without (dashed lines). Whereas at $V = 1.6$ both calculations show only the SDW minimum at $\delta = 0$, they differ at $V = 1.7$ where the system should already be in the charge-ordered phase [54, 57, 58, 60]. Without optimization of the staggered field, we would still find the SDW minimum at $\delta = 0$, but with optimization

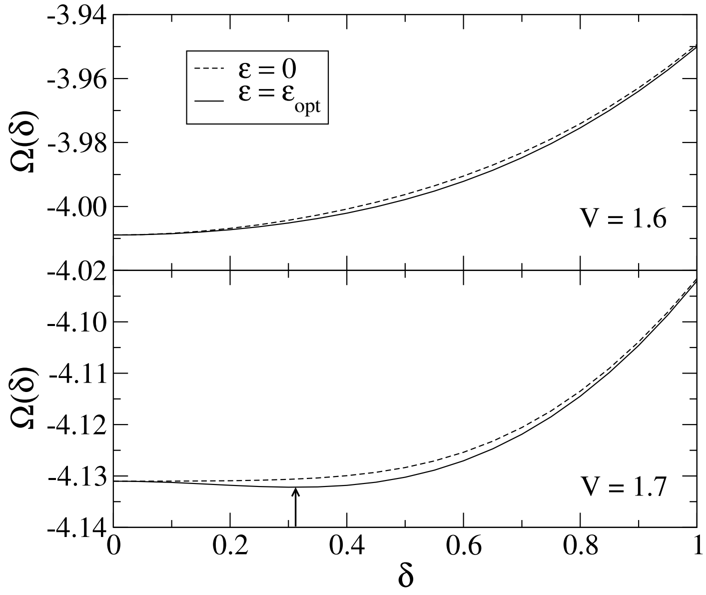

Figure 5.5.: Grand potential Ω as function of the mean-field parameter δ at $U = 3$ calculated on a cluster with $N_{\mathrm{c}} = 8$ sites as reference system. Upper panel: $V = 1.6$. Lower panel: $V = 1.7$. Solid lines: With optimization of a staggered field. Dashed lines: Without optimization of a staggered field. The arrow marks the CDW minimum at $V = 1.7$.

the minimum shows up for a finite value of $\delta = \pm 0.31$ characteristic for the CDW phase.

For the determination of the critical value V_{c}, we calculated the ground state energy E_0, kinetic energy E_{kin}, and the order parameter m_{CDW} at several values of V shown in Fig. 5.6. We performed no finite-size scaling like in Sec. 5.2.1 since we found that here the cluster sizes are too small for a systematic scaling. Different from Fig. 5.3, E_{kin}, m_{CDW}, and the slope of the ground state energy are continuous across the transition point as required for a second-order transition. From the kinetic energy and the order parameter calculated on a cluster of size $N_{\mathrm{c}} = 12$, we extract a critical value of $V_{\mathrm{c}} = 1.665(5)$, which is in good agreement with the critical value $V_{\mathrm{c}} \approx 1.65$ obtained by QMC [54] and diagonalization methods [57, 58, 68], and with $V_{\mathrm{c}} = 1.64(1)$ from DMRG calculations [60]. The slight difference is likely due to remaining finite-size effects. Moreover we made use of a single variational parameter only, namely the staggered field Eq. (5.9), and it can be expected that including more single-particle parameters in the SFA optimization procedure would give even more accurate results.

We would like to point out that in the present case of a second-order phase transition, the most accurate way of calculating the mean-field parameter δ is to find the minimum in the grand potential including SFA optimization of single-particle parameters. Calculations on a cluster of size $N_{\mathrm{c}} = 12$ showed that without optimization

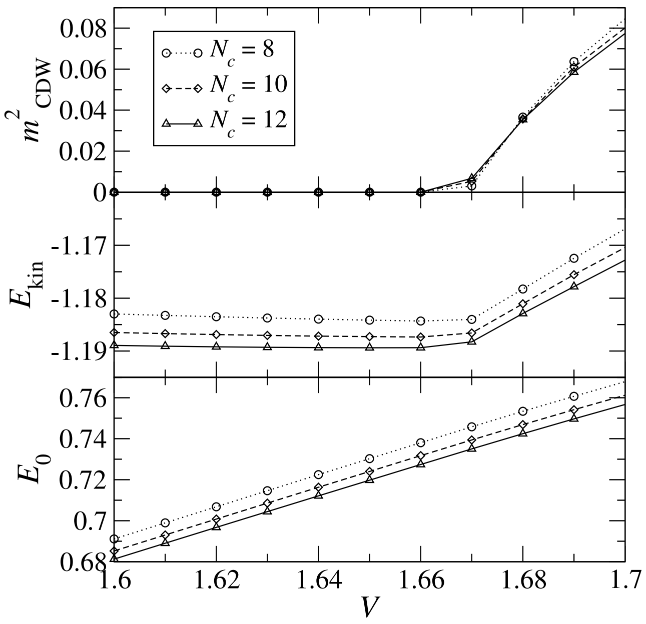

Figure 5.6.: Ground-state energy E_0, kinetic energy E_{kin}, and order parameter m^2_{CDW} of the one-dimensional EHM at $U = 3$ for cluster sizes $N_{\mathrm{c}} = 8$ (dotted), $N_{\mathrm{c}} = 10$ (dashed), and $N_{\mathrm{c}} = 12$ (solid line).

Table 5.2.: Same as Tab. 5.1, but for $U = 3$.

	t_{fit}	Δ_{fit}	Δ_{HF}
$V = 0$	1.38	0.29	0.93
$V = 1$	1.59	0.29	0.93
$V = 2$	1.40	1.13	2.12
$V = 3$	1.59	3.71	4.28

the critical value would be $V_{\mathrm{c}} = 1.685(5)$. Compared to $V_{\mathrm{c}} = 1.665(5)$ this is further away from the values obtained by other methods as given above. Calculations with δ obtained self-consistently on an isolated cluster are insufficient. In this case one would get $V_{\mathrm{c}} = 1.735(5)$ for the $N_{\mathrm{c}} = 12$ cluster. This means that for a second-order phase transition δ should be determined by minimizing the grand potential, whereas for first-order transitions the self-consistent determination was sufficient.

The spectral function $A(\boldsymbol{k}, \omega)$ at $V = 1.0$, 2.0, and 3.0, which has not been calculated previously, is depicted in Fig. 5.7. We found that the spectral function at $V = 1.0$ shows only minor differences to the spectral function of the Hubbard model ($V = 0$). The white lines in Fig. 5.7 are fits to a Hartree-Fock SDW/CDW dispersion. The parameters t_{fit} and Δ_{fit} can be read off from Tab. 5.2. In the SDW phase at $V = 0$ and $V = 1.0$, the gap Δ_{fit} is constant. Similar to the case $U = 8$ the agreement between Δ_{fit} and Δ_{HF} is better in the CDW phase than in the SDW phase. The hopping

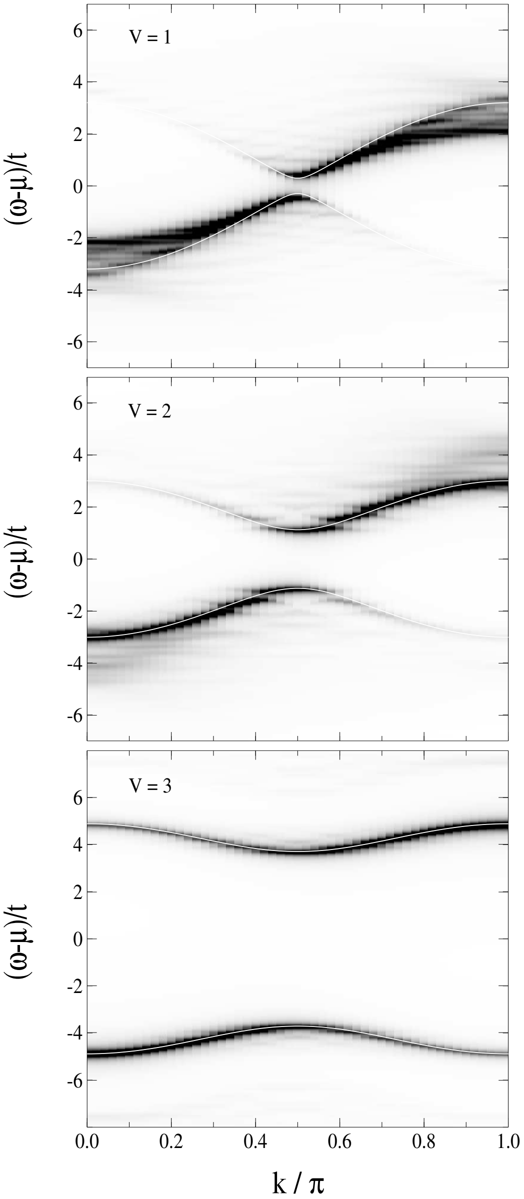

Figure 5.7.: Density plot of the spectral function $A(\boldsymbol{k}, \omega)$ of the one-dimensional EHM at $U = 3$ calculated on a cluster of size $N_c = 12$ with Lorentzian broadening $\eta = 0.1$. Darker regions represent larger spectral weight. From top to bottom: $V = 1.0$, 2.0, 3.0. White lines are fits to a Hartree-Fock SDW/CDW dispersion (see text).

parameter t_{fit} increases when approaching the phase transition from below, similar to Tab. 5.1, but the fitted values for t_{fit} are considerably smaller than in the case $U = 8$. For the finite-size effects of these properties the same behavior was found as for $U = 8$.

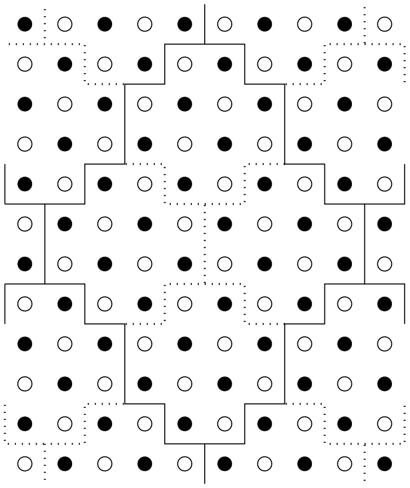

Figure 5.8.: Possible tiling of the two-dimensional square lattice into a super cluster with $N_\mathrm{c} = 48$ that allows for staggered order.

5.3. Results for two dimensions

The two-dimensional Hubbard model is one of the most intensely discussed models for strongly-correlated electron systems, especially in the context of high-temperature superconductivity. But different from the one-dimensional case, where many sophisticated methods have been used to investigate the extended Hubbard model as described in Sec. 5.2, only few studies have been done for the two-dimensional EHM. One reason for this is that many modern methods such as DMRG or fermionic loop-update QMC are difficult to apply to more than one spatial dimension. However, within our present approach, the extension to two dimensions is straightforward.

The two-dimensional EHM is defined by the Hamiltonian

$$\begin{aligned} H = & -t \sum_{\langle ij \rangle,\sigma} \left(c^\dagger_{i,\sigma} c_{j,\sigma} + \mathrm{H.c.} \right) + U \sum_i n_{i\uparrow} n_{i\downarrow} \\ & + V \sum_{\langle ij \rangle} n_i n_j - \mu \sum_i n_i, \end{aligned} \tag{5.13}$$

where $\langle ij \rangle$ connects nearest neighbors and the chemical potential is $\mu = U/2 + 4V$ at half filling. Early QMC studies [71] showed that this model has a SDW-CDW transition similar to the one-dimensional case with transition point $V_\mathrm{c} \approx U/4$. But due to numerical difficulties it was impossible to determine the exact position and the order of the phase transition. For repulsive interactions, calculations within the Hartree-Fock approximation [72–74] showed two stable phases for the Hamiltonian Eq. (5.13) at half filling, the SDW and CDW phase, separated by a phase boundary at $V_\mathrm{c} = U/4$. The same value for the critical interaction was obtained by the fluctuation-exchange approximation (FLEX) [75].

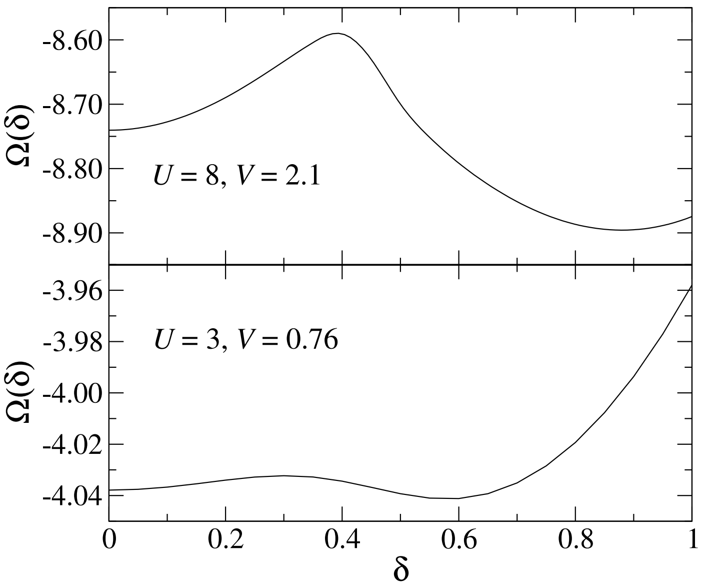

Figure 5.9.: Grand potential calculated on a cluster of size $N_\mathrm{c} = 8$ at $U = 8, V = 2.1$ (upper panel) and $U = 3, V = 0.76$ (lower panel).

For the application of the V-CPT method, the two-dimensional square lattice has to be decoupled into clusters of finite size. Some care has to be taken concerning the staggered order. Whereas for clusters with $N_\mathrm{c} = 8$ and $N_\mathrm{c} = 10$ shown in Fig. 4.1, the staggered order indicated by open and full circles is commensurate over the cluster boundaries, a straightforward decoupling into clusters of size $N_\mathrm{c} = 12$ is not possible. As one can easily see in Fig. 5.8, a super cluster with $N_\mathrm{c} = 48$ consisting of four $N_\mathrm{c} = 12$ clusters has to be constructed in order to take into account the staggered order correctly. The Green's function of the super cluster can be calculated by switching off the hopping processes that connect the single $N_\mathrm{c} = 12$ clusters, in other words on bonds across the dotted lines in Fig. 5.8. This gives a block-diagonal Hamiltonian which can be treated by the Lanczos algorithm. The switched off hopping processes are then incorporated again perturbatively, that means by including the corresponding hopping terms in the matrix $T_{a,b}^{\boldsymbol{R},\boldsymbol{R}'}$ in Eq. (2.3). Note that here the vectors $\boldsymbol{R}$ and $\boldsymbol{R}'$ denote the super clusters and not the single $N_\mathrm{c} = 12$ clusters. Of course there are many other possible tilings like the 4×3 cluster used in Refs. [3, 4, 21], but also in that case a super cluster of $N_\mathrm{c} = 24$ has to be used.

We start the analysis of the two-dimensional EHM with the determination of the order of the phase transition. For this purpose we use the $N_\mathrm{c} = 8$ cluster shown in Fig. 4.1 and calculate the grand potential $\Omega(\delta)$ in the vicinity of the transition point at $U = 8.0$ and $U = 3.0$ as described in method (ii) in Sec. 5.1. Here we did not use a staggered field as variational parameter, because it does not change the qualitative shape of $\Omega(\delta)$ (see Figs. 5.2 and 5.5) and is therefore not necessary for the determination of the order of the transition. The result of this calculation is shown in Fig. 5.9. At both values of U we found three minima, located at $\delta = 0$ and $\delta = \pm\delta_{\mathrm{CDW}}$, which indicates a first-order phase transition, different from the one-dimensional EHM, where at $U = 3.0$ the transition is of second order. We checked that this different behavior is not likely to be a finite-size effect due to the small linear dimension of the two-dimensional $N_{\mathrm{c}} = 8$ cluster by calculating $\Omega(\delta)$ for the one-dimensional model with $N_{\mathrm{c}} = 4$ which still shows clear evidence of a second-order phase transition at $U = 3$.

The fact that the system shows first-order transitions at both $U = 8.0$ and $U = 3.0$ simplifies the subsequent calculations. As discussed in the previous section, one gets good results in the case of a first-order transition by using a mean-field parameter δ determined self-consistently on an isolated cluster, as described in method (i) in Sec. 5.1. This procedure is much faster than the calculation of the grand potential for many values of δ, which makes it possible to use the $N_{\mathrm{c}} = 48$ super cluster shown in Fig. 5.8. We want to mention at this point that the calculation of the grand potential for the two-dimensional system is much more time consuming than for one dimension because of the larger number of $\boldsymbol{k}$ points required for the evaluation described in Sec. 2.2.1 (see Eq. (2.16)). For one dimension $L \approx 40$ is sufficient for convergence, whereas $L \approx 500$ is necessary for two dimensions. Nevertheless it is of crucial importance to use a cluster as large as possible, because the ratio of bonds treated exactly to mean-field decoupled bonds increases with increasing cluster size, especially pronounced for the two-dimensional square lattice. After having determined the mean-field parameter δ for the CDW phase self-consistently, we also performed an SFA optimization of a staggered field, Eq. (5.9).

A few more words have to be said about calculations in the SDW phase ($\delta = 0$). In Sec. 4.2 it has been shown that it is important to take into account the long-range magnetic order for the accurate description of salient features of the system. This has been achieved by using a staggered magnetic field as variational parameter, given by Eq. (4.2). Additionally it was argued that due to the connection of the hopping parameter t and the magnetic exchange constant J, results are further improved by letting the hopping in the clusters be of strength t' and optimizing the staggered magnetic field and t' simultaneously. Therefore we use

$$\Delta_{a,b} = h\delta_{a,b} z_\sigma e^{\mathrm{i}\boldsymbol{Q}\boldsymbol{r}_a} - \tau\delta_{\langle ab\rangle'}, \tag{5.14}$$

where the symbol $\delta_{\langle ab\rangle'}$ is equal to one for nearest-neighbor bonds inside the cluster and zero otherwise. The field strength h and $\tau = t' - t$ are the variational parameters in the optimization procedure.

To sum up, the following steps are performed in the analysis using the $N_{\mathrm{c}} = 48$ super cluster:

(i) First we determine the mean-field parameter δ_{CDW} in the CDW phase self-consistently on an isolated cluster.

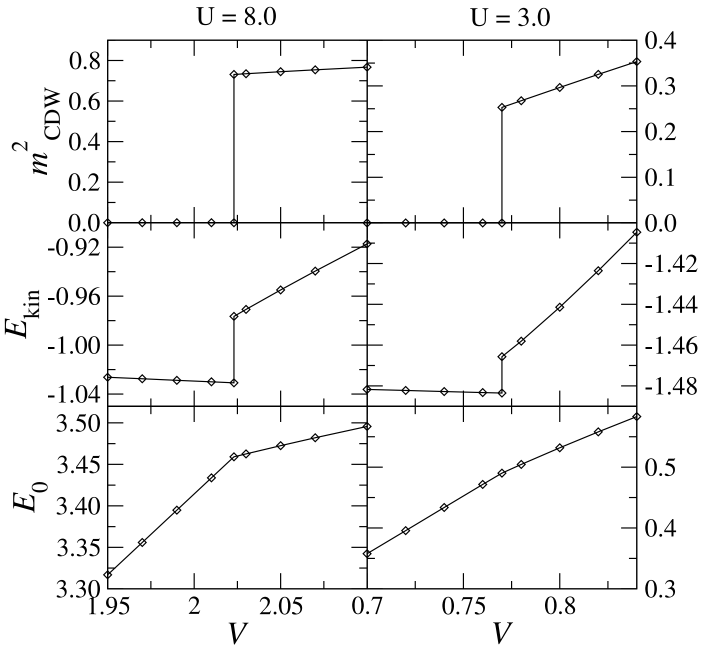

Figure 5.10.: Ground-state energy E_0, kinetic energy E_{kin}, and order parameter m^2_{CDW} of the 2D EHM at $U = 8.0$ (left) and $U = 3.0$ (right). Calculations were done on a $N_{\text{c}} = 48$ super cluster.

(ii) We use a staggered field Eq. (5.9) for an SFA optimization procedure.

(iii) In the SDW phase ($\delta = 0$) the staggered magnetic field and the intra-cluster hopping t', Eq. (5.14) are optimized simultaneously.

(iv) After determination of the SFA variational parameters we calculate the quantities we are interested in.

The results for the ground-state energy, kinetic energy, and order parameter are shown in Fig. 5.10. At both $U = 8.0$ and $U = 3.0$, the behavior of a first-order transition can be seen, where the change in the slope of E_0 is much stronger at $U = 8.0$ than at $U = 3.0$. This change at $U = 8.0$ is even more pronounced than for the one-dimensional model at $U = 8.0$. From Fig. 5.10 we can extract the critical value V_{c} of the phase transition by fitting E_0 to a straight line in the vicinity of the transition point, and for the $N_{\text{c}} = 48$ super cluster we find $V_{\text{c}} = 2.023(1)$ at $U = 8.0$, and $V_{\text{c}} = 0.770(3)$ at $U = 3.0$. These values of V_{c} are much closer to the Hartree-Fock result $V_{\text{c}} = U/4$ than for one dimension. Within our approach we cannot clarify whether this is an intrinsic feature of the two-dimensional model or it is an artifact of the approximation due to the larger number of mean-field decoupled bonds.

The SFA variational parameters in the SDW phase near the phase-transition point are found to be almost independent of the interaction V. At $U = 8$, the optimization resulted in $t' \approx 1.1$ for the intra-cluster hopping and $h \approx 0.14$ for the staggered magnetic field. The optimization of just one single parameter leads to $t' \approx 1.03|_{h=0}$ and $h \approx 0.12|_{t'=t}$, and the value of Ω also differs significantly from the value obtained by the simultaneous optimization of t' and h. This means that due to the strong connection between the magnetic order and the hopping matrix element it is important to optimize t' and h simultaneously in order to get the best approximation for the physics in the thermodynamic limit. In the charge-ordered phase the dependence of the variational parameter, Eq. (5.9), on the interaction V is larger with $\varepsilon = 0.08$ at $V = 2.01$ and $\varepsilon = 0.22$ at $V = 2.1$. A similar behavior can be found at $U = 3$: In the SDW phase the variational parameters $t' \approx 1.61$ and $h \approx 0.15$ are almost independent of V. In the CDW phase we get $\varepsilon = -0.03$ at $V = 0.76$ and $\varepsilon = -0.18$ at $V = 0.84$.

Whereas the application of the staggered magnetic field exhibits the symmetry $h \to -h$, this is not the case for the staggered field Eq. (5.9), because the symmetry is already broken by the mean-field decoupling. We found no stationary point of Ω for finite h in the CDW phases.

The spectral function at $U = 8$ in the SDW phase ($V = 1.0$) and in the CDW phase ($V = 3.0$) is shown in the left plots of Fig. 5.11. We found that the spectral function at $V = 1.0$ is very similar to the spectral function of the Hubbard model ($V = 0$), see Fig. 4.9. One can see that the spectrum mainly consists of four features, two high-energy Hubbard bands and two low-energy quasi-particle bands, separated by a gap in the spectrum. The dispersion of these low-energy excitations in the SDW phase differs significantly from the Hartree-Fock shape shown as white lines in the left upper panel of Fig. 5.11, which does not account for the splitting into coherent low-energy bands and high-energy Hubbard bands. The fit parameters were $t_{\text{fit}} = 1.34$ and $\Delta_{\text{fit}} = 2.51$. The width of the coherent bands $|\omega(X) - \omega(\Gamma)| \approx 1.25$ is rather set by the magnetic exchange J, consistent with QMC calculations at $V = 0$ [52, 76]. The black lines are fits to the t-J-like dispersion

$$E(\boldsymbol{k}) = \pm\left[-\Delta + J/2(\cos k_x + \cos k_y)^2\right],$$

which accounts better for the dispersion of the low-energy bands than the Hartree-Fock dispersion [76]. The fit parameters were $\Delta_{\text{fit}} = 2.69$ and $J_{\text{fit}} = -0.63$, which is in good agreement with the second-order perturbation-theory result $J = -4t^2/(U-V) = -0.57$. In the CDW phase the white lines correspond to Hartree-Fock dispersions with fit parameters $\Delta_{\text{fit}} = 7.69$ and $t_{\text{fit}} = 1.16$, and different from the SDW phase they agree well with the excitations of $A(\boldsymbol{k}, \omega)$.

The plots on the right hand side of Fig. 5.11 display the spectral function at $U = 3$ at interactions $V = 0.5$ and $V = 1.0$, respectively. The white lines again correspond to Hartree-Fock dispersions with fit parameters $t_{\text{fit}} = 1.06$, $\Delta_{\text{fit}} = 0.64$ at $V = 0.5$, and $t_{\text{fit}} = 1.07$, $\Delta_{\text{fit}} = 1.82$ at $V = 1.0$, respectively. As in the case $U = 8$ the dispersion of the coherent low-energy bands in the SDW phase differs from the Hartree-Fock prediction, but in this case the deviation is much smaller. We did not find an

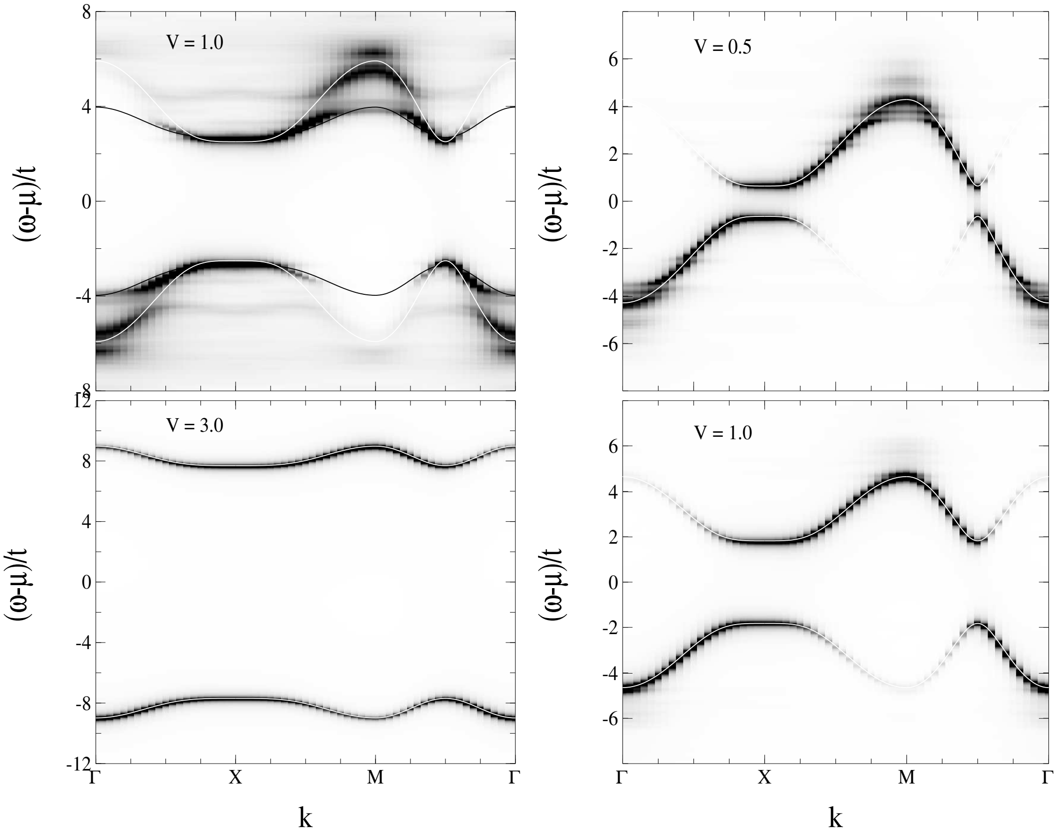

Figure 5.11.: Density plot of the spectral function $A(\boldsymbol{k},\omega)$ of the two-dimensional EHM calculated on a $N_\mathrm{c} = 48$ super cluster with broadening $\eta = 0.1$. Darker regions represent larger spectral weight. Left top: $U = 8.0, V = 1.0$. Left bottom: $U = 8.0, V = 3.0$. Right top: $U = 3.0, V = 0.5$. Right bottom: $U = 3.0, V = 1.0$. White lines are fits to Hartree-Fock dispersions. For the meaning of the black lines at $U = 8.0, V = 1.0$ see text.

accurate functional form in order to fit the low-energy excitations, but nevertheless we can extract the value of J from the band with of the coherent bands yielding $J = -(1/2)|\omega(X) - \omega(\Gamma)| \approx -1.57$. This value is again in good agreement with the perturbation-theory result $J = -4t^2/(U - V) = -1.6$.

We would like to mention that our results at $U = 3$ in the SDW phase are qualitatively different from QMC results at $U = 3$, $V = 0$, and inverse temperature $\beta = 3t$ [77], where the spectral function shows metallic behavior with no gap around the Fermi energy. This difference may be due to temperature effects or due to poor resolution of the Maximum-Entropy inversion of QMC correlation functions.

At both $U = 8$ and $U = 3$, one can easily see that the agreement of the Hartree-Fock dispersions with the low-energy excitations of $A(\boldsymbol{k},\omega)$ is better in the CDW phase than in the SDW phase. In addition the gap Δ_HF calculated within the Hartree-

Fock approximation is much closer to the fitted gap Δ_{fit} in the CDW phase (e.g., $\Delta_{\text{HF}} = 7.76$, $\Delta_{\text{fit}} = 7.69$ at $U = 8$, $V = 3$) than in the SDW phase (e.g., $\Delta_{\text{HF}} = 3.57$, $\Delta_{\text{fit}} = 2.51$ at $U = 8$, $V = 0$). Therefore we conclude that in the CDW phase charge fluctuations play only a minor role compared to the SDW phase, similar to the one-dimensional system.

6. Charge Ordering and Lattice Coupling in NaV_2O_5

The formation of an ordered pattern of ion charges is a rather general type of phase transition which occurs in three- as well as lower-dimensional solids. It has been known for more than six decades [78] since its discovery in magnetite Fe_3O_4. Even in that compound this phenomenon still attracts a lot of attention due to the interesting physics of the transition. Since the charge ordering causes changes in the interaction between the ions, it drives a lattice distortion, which, in turn, influences the order pattern. The quarter-filled ladder compound NaV_2O_5 [79] is another interesting example of a system which shows charge ordering.

6.1. Introduction to the compound NaV_2O_5

The crystallographic structure of NaV_2O_5 is depicted schematically in Fig. 6.1. It is mainly determined by the layers formed by the V_2O_5 pyramids. The sodium atoms, which are mainly acting as charge reservoir, form chains that are lying between the layers. The coupling in c direction, i.e., between the single layers, is very weak, and the properties of this compound are therefore mainly determined by the quasi two-dimensional V_2O_5 layers, shown in Fig. 6.2. The black circles indicate the vanadium atoms and the yellow ones the oxygen atoms of the ground plane of the pyramids. The oxygen on top of the pyramids plays only a minor role, since it does not couple two vanadium atoms of the layer.

The first X-ray studies at room temperature indicated a non-centrosymmetric structure $P2_1mn$ [80] with two different vanadium atoms in the unit cell, forming chains of two kinds of VO_5 pyramids. Analysis of the V-O bond length and of the Na-V distance showed that these chains are possibly $V^{4+}O_5$ and $V^{5+}O_5$ chains, resp. Therefore this compound should behave like a quasi one-dimensional spin system, because the magnetic V^{4+} ions are well separated by the non-magnetic V^{5+} ions.

Several years later this quasi-one-dimensional behavior was found experimentally in measurements of the magnetic susceptibility by Isobe and Ueda (see Fig. 6.3) [81]. They found that NaV_2O_5 behaves like a $S = \frac{1}{2}$ 1D antiferromagnetic Heisenberg linear chain with a coupling constant of approximately $J \approx 560\,\mathrm{K}$. In addition they found

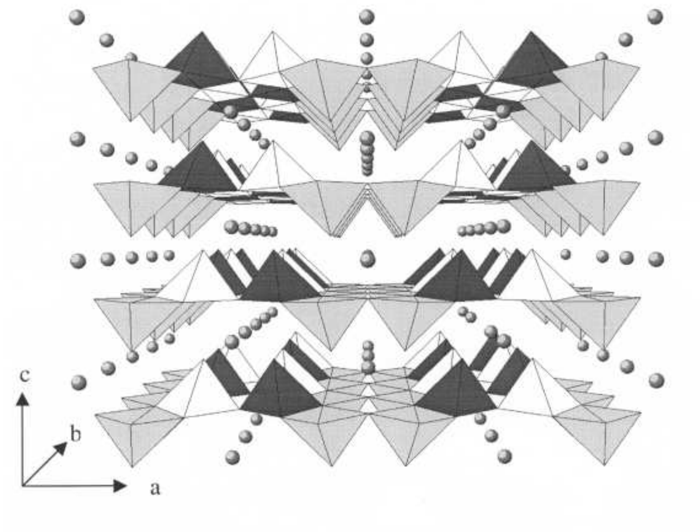

Figure 6.1.: Crystallographic structure of NaV_2O_5. The pyramids are built by oxygen atoms around a central vanadium site. The sodium atoms are lying between the V_2O_5 layers.

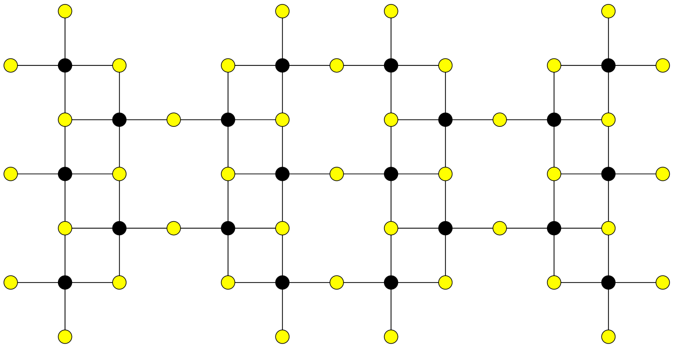

Figure 6.2.: One V_2O_5 layer, where only the oxygen atoms in the ground plane of the pyramids are displayed. Yellow circles indicate oxygen atoms and black circles vanadium atoms.

a phase transition at $T_c \approx 35K$ with a rapid decrease of the magnetic susceptibility and an opening of a spin gap with $\Delta \approx 10$ meV, and the unit cell is doubled in a and b direction and quadrupled in c direction. They supposed that this is due to a spin-Peierls transition, where a dimerization of the lattice results in alternating coupling constants, and hence in the opening of a spin gap.

Recent X-ray studies [79, 82, 83] showed, that the crystallographic structure of NaV_2O_5 at room temperature is the centrosymmetric structure $Pmmn$, and the vanadium ions are all in the same valence state $V^{+4.5}$. The one-dimensional behavior at

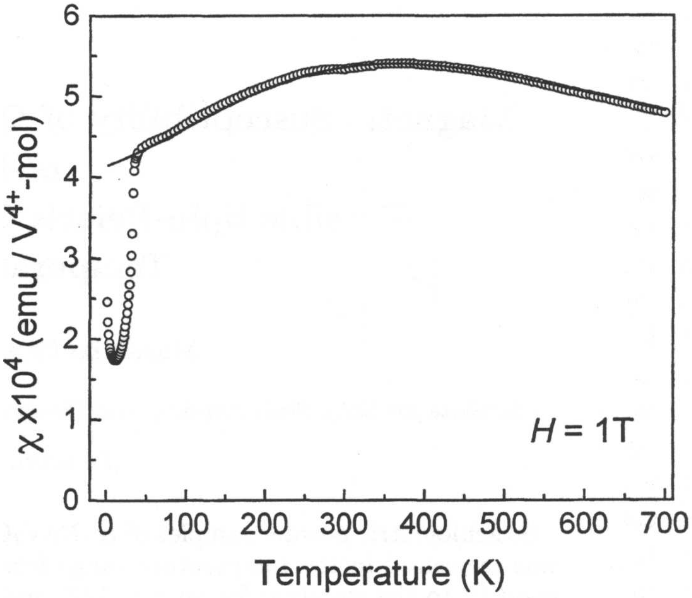

Figure 6.3.: Magnetic susceptibility of NaV_2O_5 measured in a field of $H = 1T$. Solid line is the fit to the formula for the $S = \frac{1}{2}$ 1D Heisenberg model. Figure taken from reference [81].

room temperature was therefore rather surprising, but this puzzle could be resolved by Horsch and Mack [84], who showed that a rung consisting of two vanadium sites is the key element of this compound.

Nuclear magnetic resonance (NMR) experiments [85] found a charge-ordering transition at $T_{\mathrm{CO}} \approx 35\,\mathrm{K}$ which occurs at the same [86] or at slightly lower temperature than the opening of the spin gap. In NaV_2O_5, where one d_{xy} electron is shared by two V ions in a V-O-V rung, the ordering occurs as a static charge disproportion δ between the V ions, which obtain charges $4.5 \pm \delta$ with a zig-zag pattern of δ's. Most probably, the main driving force for the transition is the Coulomb repulsion of electrons on the nearest-neighbor sites within one leg of the ladder. For half the ladders the apical oxygen ion is located below the ladder and for the other half above. Therefore the crystal environment of the V ions is asymmetric, and the d_{xy} electron is subject to a strong Holstein-like electron-phonon coupling [87]. As a result, the transition is accompanied by the displacement of ions from their positions in the high-temperature phase ($T > T_{\mathrm{CO}}$). They then form a larger unit cell, as clearly seen directly in the X-ray diffraction experiments [88], where displacements of V ions of the order of 0.05 Å were observed, and indirectly in the appearance of new phonon modes in the infrared absorption [89] and Raman-scattering spectra [90].

The importance of the coupling to the lattice for phase transitions in quarter-filled systems was shown in Refs. [91, 92]. The low-energy excitations of the zig-zag order parameter are also strongly influenced by the lattice [93].

The static properties of the ground state of the quarter-filled ladders without coupling to lattice distortions were extensively investigated using mean-field approaches [94–97], the density-matrix renormalization-group (DMRG) [98–100], bosonization and renormalization-group techniques [101]. The DMRG studies show that at strong enough onsite interaction the ladders exhibit a zig-zag charge order if the repulsion between the electrons on the nearest-neighbor sites exceeds some critical value V_c. The corresponding phase transition is of second-order as a function of V. For a very strong intersite repulsion, phase separation becomes possible [99]. Dynamical properties were studied with exact numerical diagonalization [33, 34, 102, 103] without taking into account the coupling to the lattice. They were quite successful in understanding NaV_2O_5 dynamical properties above the transition temperature.

The investigation of the ordering of electrons interacting with the lattice requires the knowledge of electron-phonon couplings and lattice-force constants in addition to electronic parameters such as hopping matrix elements and electron correlations. For a given compound almost all of these parameters can be extracted from first-principles band-structure calculations. The force constants and electron-phonon coupling can be obtained by comparing the total energies and the inter-ionic forces in distorted and undistorted lattices. The phonon frequencies required for studies of dynamical lattice distortions are given by experiment [90], while the necessary knowledge of their eigenvectors can be obtained from first-principles calculations [79, 104]. Here we will concentrate on the strongest electron-phonon mode present in NaV_2O_5, which is a simple Holstein-type interaction [104].

We therefore investigate a model which takes into account the main interactions, i.e., the Hubbard and intersite repulsions and the coupling to the lattice. We study the ground-state properties of a quarter-filled ladder coupled to static lattice distortion with the Lanczos algorithm, and moreover we apply the V-CPT method in order to investigate the spectral features of this compound, which can be compared to angle-resolved photo-emission experiments [105, 106].

6.2. Model

The quarter-filled ladder compound α'-NaV_2O_5 can be described microscopically by an extended Hubbard (or t-U-V) model (EHM). For the description of the distorted low-temperature phase we also include the coupling of electrons to the lattice, yielding the model

$$H = H_{\mathrm{EHM}} + H_{\mathrm{l}} + H_{\mathrm{e-l}}, \tag{6.1}$$

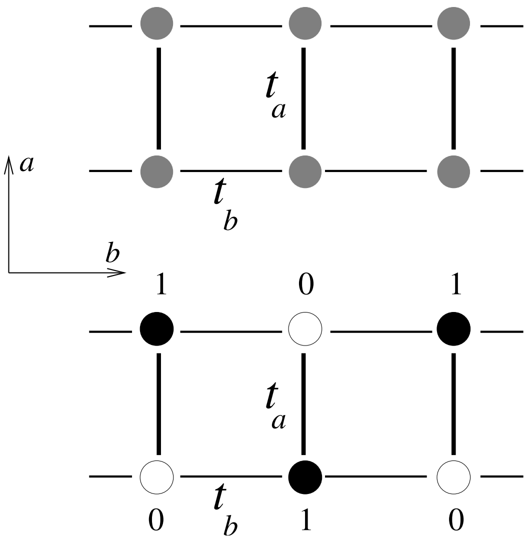

Figure 6.4.: Schematic picture of single ladders, with hopping matrix elements t_a on the rungs, and t_b along the chains. The darkness of the circles corresponds to the charges on the sites of the ladder. The upper ladder is shown without charge order, the lower ladder with zig-zag charge order.

where H_l is the lattice deformation contribution, and $H_\mathrm{e-l}$ the electron-lattice interaction. These terms are given by

$$\begin{aligned} H_\mathrm{EHM} =& -\sum_{\langle ij\rangle,\sigma} t_{ij}\left(c^\dagger_{i\sigma}c_{j\sigma}+\mathrm{H.c.}\right) \\ & + U\sum_i n_{i\uparrow}n_{i\downarrow} + \sum_{\langle ij\rangle} V_{ij}n_i n_j, \quad (6.2a) \\ H_\mathrm{l} =& \kappa\sum_i \frac{z_i^2}{2}, \quad (6.2b) \\ H_\mathrm{e-l} =& -C\sum_i z_i n_i, \quad (6.2c) \end{aligned}$$

with the effective lattice force constant κ and the Holstein constant C. The sites are labeled by the indices i, j, and z_i is the distortion on site i. The hopping matrix elements t_{ij} connect nearest neighbor sites $\langle ij\rangle$ (see Fig. 6.4) with occupation numbers $n_i = n_{i\uparrow} + n_{i\downarrow}$.

The first-principles calculations done in Refs. [79] and [104] yield the intra-rung hopping $t_a \approx 0.35$ eV, which we will use below as the unit of energy. For the hopping along the ladder we use $t_b = t_a/2$, again in agreement with the band structure results, whereas previous DMRG studies [98, 99] were mostly done at $t_a/t_b \leq 1.4$. For the onsite Coulomb interaction we use $U = 8.0$ as estimated in Ref. [79]. We assume

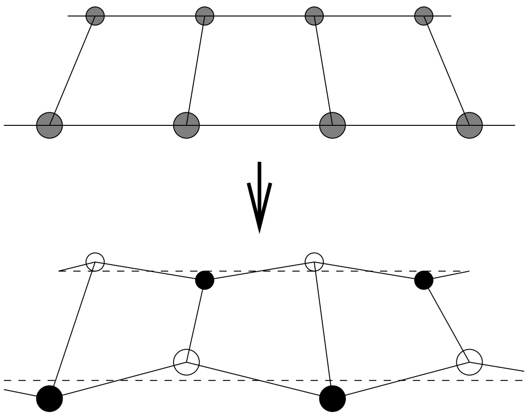

Figure 6.5.: Zig-zag distortions on a single ladder. Top: Undistorted lattice. Bottom: Distorted lattice. The gray scale of the circles indicates the charge disproportion.

$V_{ij} = V$ to be the same for all bonds, and take V as a free parameter since there is no unique procedure of extracting it from the band-structure calculations.

The lattice distortions are expressed in units of 0.05 Å since the ion displacement below T_{CO} are of this order of magnitude [88]. For the pattern of the zig-zag distortions see Fig. 6.5. With the chosen units of energy and length the comparison of the band structure and lattice force calculations done on distorted and undistorted lattices give the dimensionless constants $\kappa = 0.125$ and $C = 0.35$, respectively [104]. The effective coupling parameter C^2/κ is close to unity, and, therefore, the lattice plays an important role in determining the properties of $\mathrm{NaV_2O_5}$.

6.3. Results from exact diagonalisation

The Hamiltonian in Eq. (6.1) will be used for calculations with both static and dynamical lattice distortions [107]. At first we restrict ourselves to single ladders, which enables us to do simple finite-size scaling, and calculate the quantities of the system at zero temperature by the ground-state Lanczos method (see Sec. 2.3.2). The largest Hilbert space for the eight-rung lattice considered in this study was of dimension $N_{\mathrm{states}} = 1\,656\,592$, which could be reduced in special cases by exploiting translational invariance and S^z conservation to $N_{\mathrm{states}} = 103\,820$. The next lattice size admitting charge order would consist of ten rungs, which is so far beyond our computational capabilities. The restriction to a single ladder is a considerable simplification compared to the structure of $\mathrm{NaV_2O_5}$, but since the inter-ladder interactions are frustrated their effect in the zig-zag ordered state is supposed to be of minor importance. Later on (Sec. 6.4) we will study the influence of inter-ladder couplings by means of the V-CPT method, too.

6.3.1. Static properties

Charge order

To investigate the connection between the lattice distortion and charge ordering we calculated the static charge structure factor

$$S_{\mathrm{C}}(\boldsymbol{q}) = \frac{1}{N}\sum_{ij} \mathrm{e}^{\mathrm{i}\boldsymbol{q}(\boldsymbol{r}_i-\boldsymbol{r}_j)} \left(\langle n_i n_j\rangle - \langle n\rangle^2\right), \tag{6.3}$$

where N is the total number of sites in the system. The zig-zag charge order parameter m_{CO} can be expressed in terms of this structure factor as

$$m_{\mathrm{CO}}^2 = \frac{1}{N\langle n\rangle^2} S_{\mathrm{C}}(\boldsymbol{Q}), \quad \boldsymbol{Q} = (\pi,\pi). \tag{6.4}$$

The term $\langle n\rangle^2$ in the denominator ensures that the order parameter is equal to unity for full ordering, which in NaV_2O_5 corresponds to the charges of V ions within a rung to be equal to +5 and +4, respectively.

At this point the lattice distortions z_i in the Hamiltonian are external parameters of the model and not dynamical variables. Therefore they have to be fixed in a proper way, for which we chose a mean-field approach. Considering the distortions as the mean-field parameters one can extract the optimal value for the z_i by looking for the minimum in the ground state energy with respect to z_i. This procedure could be done within the unrestricted Hartree-Fock approximation, but this complicates the calculation because of the larger number of variables for which the minimum has to be found. Instead we restrict ourselves to a single order pattern, the zig-zag order [94, 96], which was observed experimentally [88],

$$z_i = z\mathrm{e}^{\mathrm{i}\boldsymbol{Q}\cdot\boldsymbol{r}_i}, \tag{6.5}$$

and investigate the total energy as a function of z. The optimal values of z, where the total energy reaches the minimum for several values of the nearest neighbor Coulomb interaction V determined in this way are indicated by arrows in Fig. 6.6. In the following we denote the position of the minimum in the ground-state energy by z_{min}.

For interaction strengths of $V = 1.5$ up to $V = 3.0$ a clear minimum occurs at $z \approx 1$. Additionally one finds a maximum at $z = 0$, which results from the $z \to -z$ symmetry of the system. We also found a small distortion for $V = 1.0$, but it is strongly size-dependent and rapidly decreases with increasing length of the ladder, whereas the distortions marked by arrows in Fig. 6.6 are almost independent of the system size. Therefore we argue that the finite value of z at $V = 1.0$ is due to finite-size effects and disappears in the thermodynamic limit. For this reason we did not mark it with an arrow in Fig. 6.6.

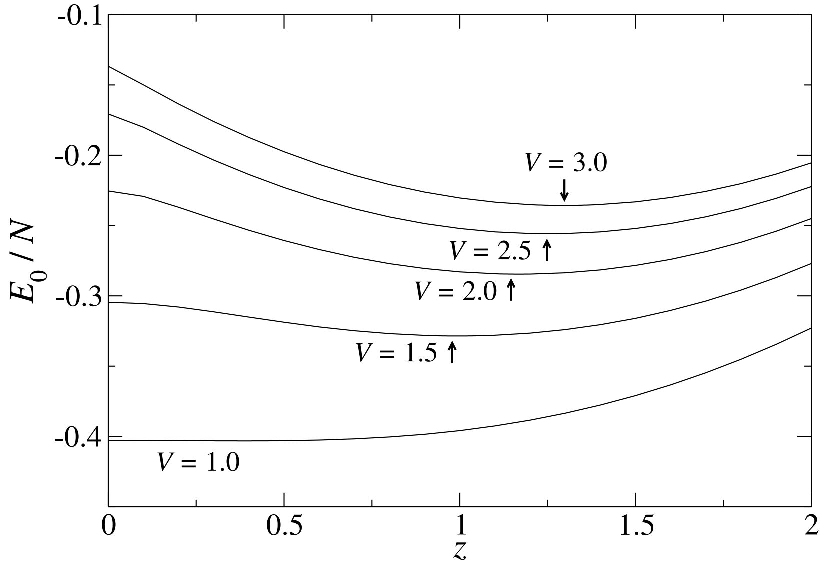

Figure 6.6.: Ground-state energy per site as a function of the distortion z calculated on an 8×2 system with periodic boundary conditions along the ladder, and $C = 0.35$. From bottom to top: $V = 1.0$, 1.5, 2.0, 2.5, 3.0. The arrows indicate the position of the minimum.

This behavior gives a first idea about the charge ordering of the system with and without coupling to the lattice. From Fig. 6.6 one could expect that the charge-ordering transition in the presence of static mean-field-like lattice distortions occurs in the region between $V = 1.0$ and $V = 1.5$. In order to investigate this transition we calculate the order parameter given by Eq. (6.4). This quantity shows strong finite-size effects, which makes it necessary to apply finite-size scaling. We calculated the order parameter for systems of four and eight rungs, respectively, the largest system size available. Although higher-order corrections to the scaling behavior are expected for these small systems, we performed a $1/N_{\text{rungs}}$ extrapolation to $1/N_{\text{rungs}} = 0$. This procedure does not give the exact value of the order parameter in the thermodynamic limit and does not allow to extract an exact value for the critical Coulomb interaction V_{c}, but it provides the possibility to obtain a rough estimate of the interaction V at which the phase transition occurs as well as the approximate $m^2_{\text{CO}}(V)$ dependence.

To study the effects of the lattice distortions we also calculated the order parameter without coupling to the lattice, that is for $C = 0$. The results are shown in Fig. 6.7. As one can see in the upper panel where no lattice distortions are present, the order parameter changes rather smoothly when going from the disordered phase into the ordered one. A different behavior can be found for finite lattice distortions. Here the charge ordering sets in at a much lower value of V than in the absence of distortions. In addition the transition sharpens considerably. For both zero and finite distortions the finite size scaled order parameter is slightly negative for small interactions V, which

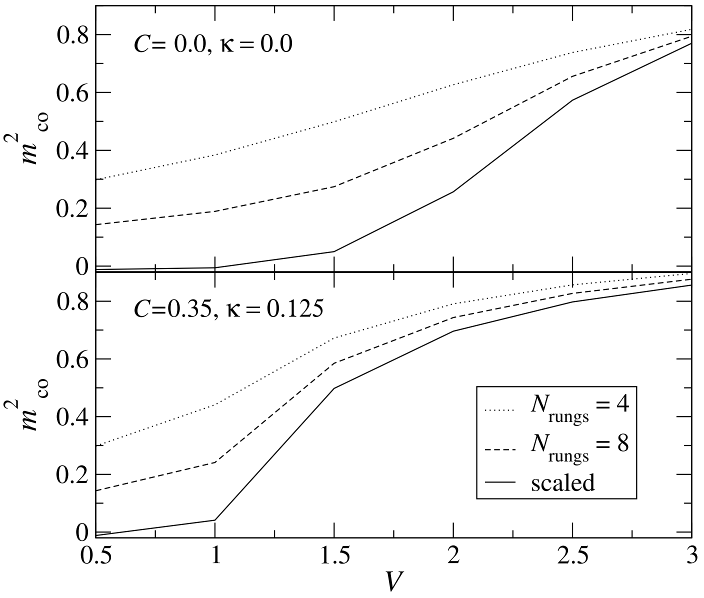

Figure 6.7.: Charge order parameter for several values of V. Upper/lower panel: Calculation without/with coupling to the lattice. The solid lines are obtained by $1/N_{\rm rungs}$ finite-size extrapolation.

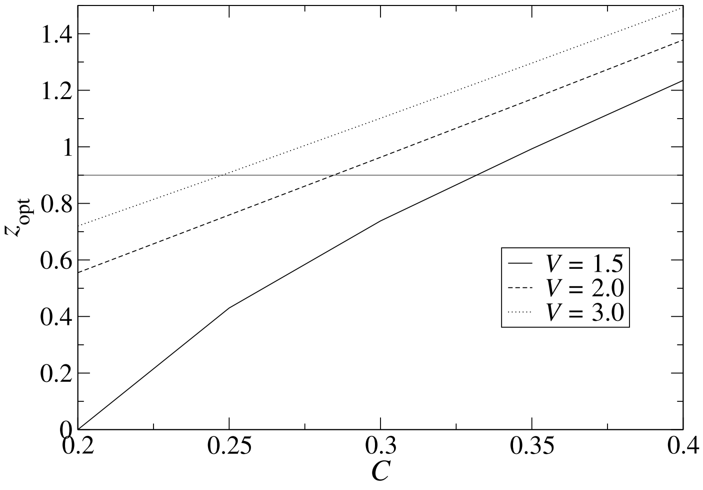

Figure 6.8.: Optimal distortion $z_{\rm opt}$ as a function of the Holstein constant C for different values of the Coulomb interaction V, calculated on a 8×2 cluster. The horizontal line indicates the experimental result.

is due to the fact that higher order corrections in the scaling have been neglected.

The optimal distortions z for different values of the Holstein constant C and repulsion V are presented in Fig. 6.8. In our units the distortion found experimentally in the charge-ordered phase is at approximately $z = 0.9$ [88], indicated by a horizontal

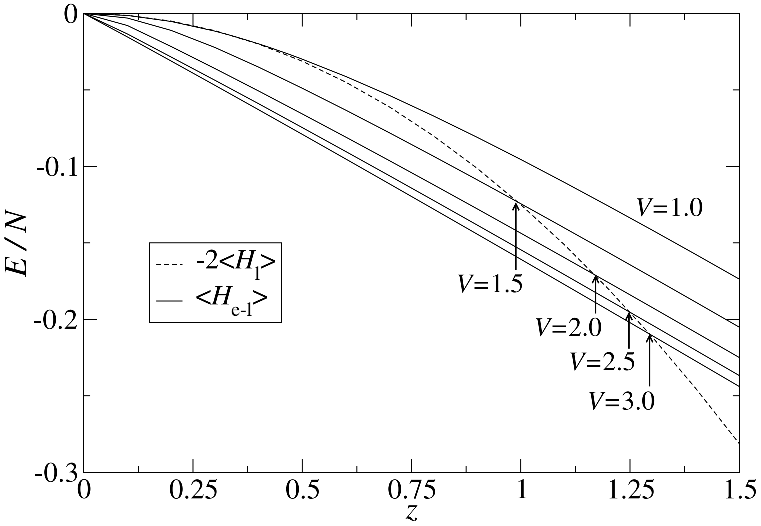

Figure 6.9.: Contribution of the lattice energy Eq. (6.2b) (dashed) and the electron-lattice energy Eq. (6.2c) (solid) to the ground state energy as a function of the distortion z, at $C = 0.35$. The lattice energy is independent of V. Electron-lattice energy, from top to bottom: $V = 1.0$, 1.5, 2.0, 2.5, 3.0. The arrows are drawn where the total energy has its minimum, as in Fig. 6.6.

line in Fig. 6.8. For $V = 1.5$, close to the charge-order phase transition, this value of $z = 0.9$ is reached near $C = 0.33$. The distortion close to $z = 0.9$ is realized also for other interactions, e.g., deep in the ordered phase at $V = 3.0$, $C = 0.24$. Since, however, NaV_2O_5 is close to a quantum critical point of charge ordering [33], and because of the value for C obtained from the band-structure calculations, we conclude that the system can best be described in the ordered phase using $V \approx 1.3$ and $C \approx 0.35$.

When calculating the ground-state energy of the system, the question arises how the terms in Eq. (6.1) contribute to the total energy, i.e., whether some sort of virial theorem holds. In Fig. 6.9 the behavior of the two contributions Eq. (6.2b) and Eq. (6.2c) is shown. One can easily see that the crossing points of the curves are at the same value of z at which the ground-state energy reaches its minimum, Fig. 6.6. Therefore we find that a virial theorem, like that for the one-electron polaronic states [108], is fulfilled in the form

$$\langle H_{\mathrm{l}} \rangle = -\frac{1}{2} \langle H_{\mathrm{e-l}} \rangle,$$

with a relative numerical accuracy of better than 10^{-4}. For large Coulomb interactions well above the phase transition this high accuracy is likely achieved since the ion charges depend very weakly on z. Therefore, compared to $H_{\mathrm{e-l}}$ and H_{l}, H_{EHM} is almost independent of z

$$\frac{\mathrm{d}H_{\mathrm{EHM}}}{\mathrm{d}z}(z_{\mathrm{min}}) \approx 0.005,$$

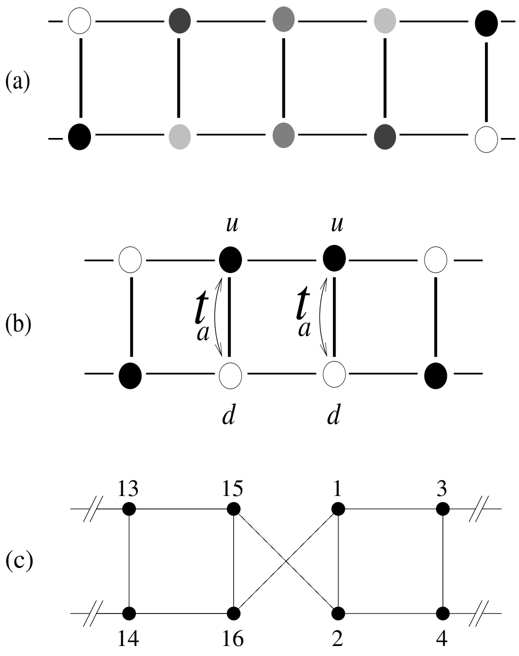

Figure 6.10.: (a) A schematic plot of a nonlocal kink-like excitation in an ordered ladder. The darkness of the circles corresponds to the charges on the sites of the ladder. (b) Local kink excitation with a sharp change of the order parameter. The electron states for one of the electrons moving between sites u and d are degenerate in this case. (c) Twisted ("Möbius") boundary conditions which produce a kink excitation. The numbers label the sites in the 8×2 cluster from 1 to 16.

and the dependence of $H_{\mathrm{e-l}}(z)$ in Fig. 6.9 is close to a straight line. Then the virial theorem follows from the functional form of $H_{\mathrm{l}}(z)$ and $H_{\mathrm{e-l}}(z)$. For smaller values of the interaction, e.g., $V = 1.5$, the dependence of the ion charges and H_{EHM} is considerably larger

$$\frac{\mathrm{d}H_{\mathrm{EHM}}}{\mathrm{d}z}(z_{\mathrm{min}}) \approx 0.03.$$

Yet also in this case the virial relation is satisfied. The contribution of the sum of the lattice terms $\langle H_{\mathrm{l}} + H_{\mathrm{e-l}} \rangle$ to the total energy varies between 19% at $V = 1.5$ and 30% at $V = 3.0$.

Kink excitations

So far we have considered the perfect zig-zag charge order pattern described by Eq. (6.5). This ordering can be destroyed by local in-rung excitations where an electron hops from the site with minimal energy to that with maximal energy, as marked by black and white circles in Fig. 6.4. The excitation energy of this process is $2V$,

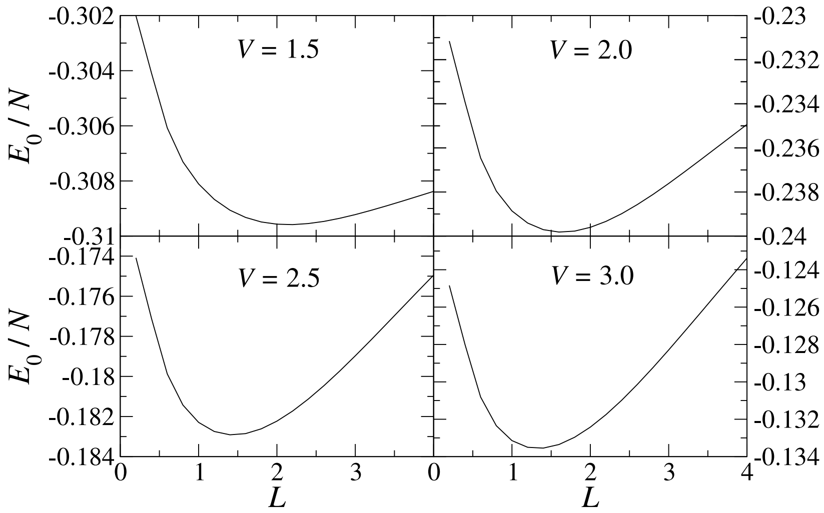

Figure 6.11.: Ground-state energy per site as a function of the kink length L, Eq. (6.6).

provided the system is totally ordered, that is $m_{\mathrm{CO}} = 1.0$. Another type of excitation is the formation of a local pair of doubly-occupied and empty rungs, which has the same energy $2V$ at $m_{\mathrm{CO}} = 1.0$. In addition, there are nonlocal kink-like excitations, where the order parameter smoothly changes along the ladder between two degenerate patterns as shown in Fig. 6.10. The nonlocal character of the excitation leads to a decrease of the excitation energy. Since the lattice is coupled to ion charges by the Holstein interaction, the kinks couple to the lattice, too.

In order to investigate kink excitations we used the largest system size available, which is a single ladder consisting of eight rungs, and imposed twisted "Möbius" boundary conditions [109] as shown in Fig. 6.10. The zig-zag distortions of Eq. (6.5) are modified to a kink distortion

$$z_i = z e^{\mathrm{i}\boldsymbol{Q}\cdot\boldsymbol{r}_i} \tanh\left[\frac{(\boldsymbol{r}_i - \boldsymbol{r}_0)\hat{\boldsymbol{e}}_a}{L}\right], \tag{6.6}$$

with the center of the kink $\boldsymbol{r}_0$ located in the middle between the rungs, L being its length in units of the lattice spacing, and $\hat{\boldsymbol{e}}_a$ the unit vector in ladder direction.

For interactions up to $V = 1.0$ the ground-state energy strongly decreases with increasing kink length L without a minimum, implying that at this weak coupling we have no kink excitations in the system. For larger interactions we found a clear minimum in the ground-state energy. The kink length at $V = 1.5$ is $L \approx 2.15$, and it shrinks to $L \approx 1.33$ at $V = 3.0$.

The kink excitation energy is defined as the difference between the ground-state energy with twisted boundary conditions at the optimal value of L and the ground-state energy with periodic boundary conditions and static distortions $z = z_{\mathrm{min}}$. It is shown in Fig. 6.12. In the fully ordered state and in the atomic limit where $V \gg t_a$,

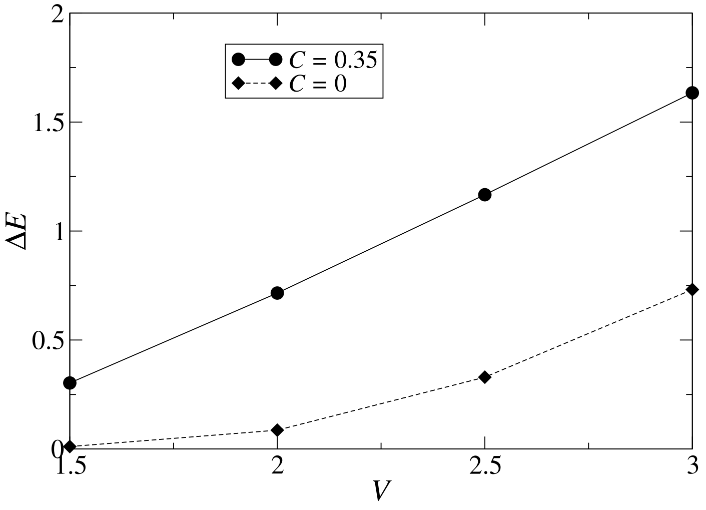

Figure 6.12.: Kink excitation energy as a function of the interaction V. It is zero for $V \leq 1.0$. The lines are guides to the eye.

the kink potential energy ΔE is close to V (see Fig. 6.10). The actual total energy is considerably smaller since the kinks are extended and since at the kink boundary the electron energy on the upper (u) and lower (d) legs become degenerate as shown in Fig. 6.10, and therefore the intra-rung hopping becomes more likely. The hopping kinetic energy of the order of $-t_a$ decreases the total energy of the system, leading to the result shown in Fig. 6.12.

For weak interactions, where the kinks are well extended and $m_{\mathrm{CO}}^2 \ll 1$, our results can be compared with a model calculation in a classical ϕ^4 model for infinite ladders [93] which gives

$$L = \frac{1}{\sqrt{V - V_{\mathrm{c}}}} \tag{6.7a}$$

$$\Delta E = \frac{3}{2} V \left(V - V_{\mathrm{c}}\right)^{3/2}, \tag{6.7b}$$

where V_{c} is the critical value of the Coulomb interaction for the phase transition. To make a connection to our results, we estimate V_{c} from Eqs. (6.7a) and (6.7b) for the distorted lattice at $V = 1.5$ and $C = 0.35$ independently and compare them. From L and ΔE we obtain $V_{\mathrm{c}} = 1.28$ and $V_{\mathrm{c}} = 1.05$, respectively. These values are in reasonable agreement with each other and consistent with the behavior of the order parameter, see Fig. 6.7.

At all values of V the kink excitation energy with lattice coupling is larger than the excitation energy without coupling shown as dashed line in Fig. 6.12. This can be understood since at a fixed value of $V > V_{\mathrm{c}}$ the charge order parameter is larger for the distorted lattice. Since the ordering is more complete, the kink lengths are smaller

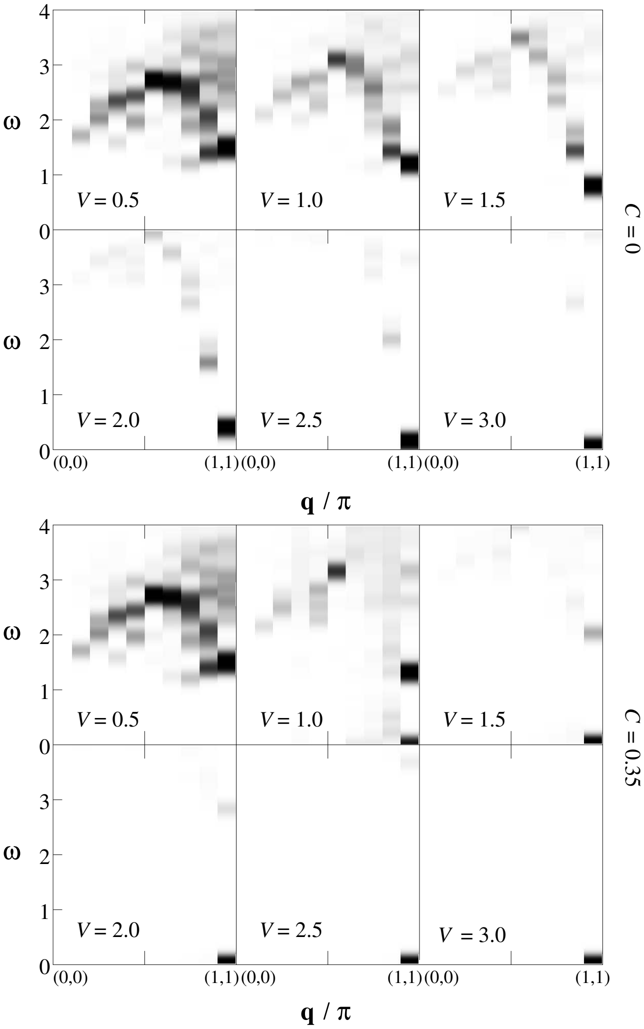

Figure 6.13.: Charge susceptibility calculated on an 8×2 ladder. Upper panel: without lattice coupling. Lower panel: With lattice coupling ($C = 0.35$). The wave-vector scan consists of the two ranges $(q_a, q_b)/\pi = (0, 0) \to (0, 1)$ and $(1, 0) \to (1, 1)$, separated by a tick mark on the horizontal axis. An additional broadening of width $\eta = 0.1$ was used.

which increases the excitation energy. Note that without lattice coupling we have no parameter L like in Eq. (6.6) for the determination of the kink length.

6.3.2. Dynamical properties

In the previous section we only considered static properties. However, enlightening insight into the physics of the system can be extracted from dynamical correlation functions showing the spectra of charge and spin excitations. The corresponding sus-

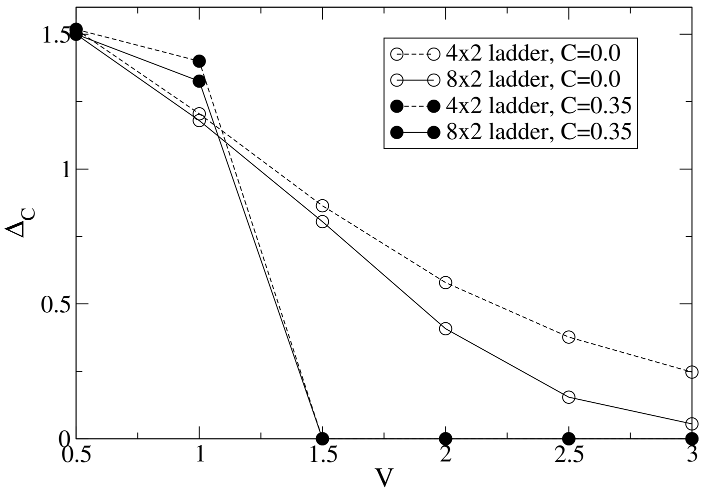

Figure 6.14.: Charge gap Δ_C at $\boldsymbol{q} = \boldsymbol{Q}$ of the charge susceptibility as a function of V. Solid lines: 8×2 ladder. Dashed lines: 4×2 ladder. Open symbols: Without lattice coupling. Full symbols: With lattice coupling (see text for case $V = 1.0$).

ceptibilities are given by

$$\chi_{\mathrm{C}}(\boldsymbol{q}, \omega) = \int \mathrm{d}t \, \mathrm{e}^{\mathrm{i}\omega t} \langle n_{\boldsymbol{q}}(t) n_{-\boldsymbol{q}} \rangle \tag{6.8a}$$

$$\chi_{\mathrm{S}}(\boldsymbol{q}, \omega) = \int \mathrm{d}t \, \mathrm{e}^{\mathrm{i}\omega t} \langle S^z_{\boldsymbol{q}}(t) S^z_{-\boldsymbol{q}} \rangle, \tag{6.8b}$$

where $n_{\boldsymbol{q}}(t), n_{-\boldsymbol{q}}$ and $S^z_{\boldsymbol{q}}(t), S^z_{-\boldsymbol{q}}$ are the the Fourier transforms of the charge and of the z-component of spin densities, respectively.

We calculated the charge susceptibility Eq. (6.8a) on a ladder consisting of eight rungs with pbc along the ladder. The results are shown in Fig. 6.13. We define the charge gap Δ_C as the energy at which the lowest-lying excitation of the charge susceptibility occurs. The corresponding momentum is always $\boldsymbol{q} = \boldsymbol{Q}$. In the disordered phase we have no gapless charge excitation. When increasing the Coulomb interaction V, the gap at $\boldsymbol{q} = \boldsymbol{Q}$ decreases as shown in Fig. 6.14, and all other charge excitations become insignificant. The charge gap does not vanish exactly for $C = 0$, i.e., without coupling to the lattice, but appears to go to zero as $N_{\text{rungs}} \to \infty$. When the coupling to the lattice is switched on, the gap is exactly zero in the ordered phase where the symmetry is broken explicitly. The charge gap behaves in a similar way as the order parameter (Fig. 6.7), namely: without electron-lattice coupling it changes smoothly across the phase transition, whereas the changes for finite coupling are significantly sharper.

In Fig. 6.13 at $V = 1.0$, a gapless excitation at $\boldsymbol{q} = \mathbf{Q}$ can be seen, which occurs due to a small but finite distortion. As already discussed in Sec. 6.3.1, this distortion

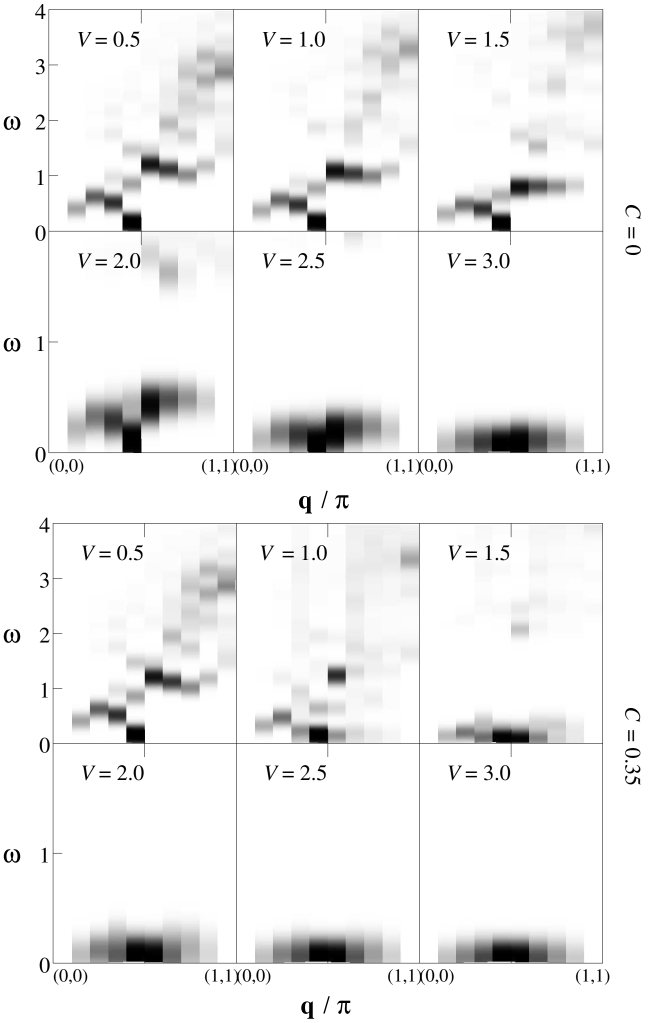

Figure 6.15.: Spin susceptibility calculated on an 8 × 2 ladder. Upper panel: without lattice coupling. Lower panel: With lattice coupling ($C = 0.35$). Presentation like Fig. 6.13.

is finite only due to the finite-size effects and should be zero in the thermodynamic limit.

We note that the gap Δ_C in the charge spectrum is different from the one commonly used in DMRG calculations, $\Delta := [E_0(N+2) - E_0(N)]/2$, where $E_0(N+2)$ and $E_0(N)$ are the ground-state energies for systems consisting of $N+2$ and N particles, respectively. Indeed, as a function of V, Δ shows a behavior *opposite* to Δ_C, with $\Delta = 0$ in the unbroken phase and $\Delta > 0$ at large V [99].

The spin susceptibility (Eq. (6.8b)) calculated on the same system is shown in Fig. 6.15. The momentum scan consists of two ranges, from $(q_a, q_b) = (0, 0)$ to $(0, \pi)$, and from $(\pi, 0)$ to (π, π). In the first range ($q_a = 0$) one can clearly see the disper-

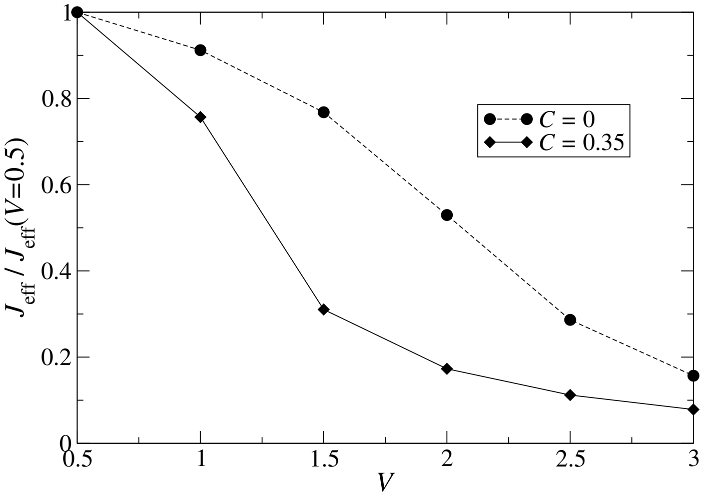

Figure 6.16.: Effective magnetic exchange interaction J_{eff} in ladder direction in units of $J_{\text{eff}}(V = 0.5)$ as a function of V, extracted from the spin susceptibility Eq. (6.8b). The interaction is shown with (solid line) and without lattice coupling (dashed line).

sion of an effective one-dimensional Heisenberg model, as predicted by perturbation theory [84]. The main change of the spin susceptibility as a function of V in this range is a decrease of the effective magnetic exchange interaction J_{eff} with increasing charge order. It can be extracted from the spin dispersion using $J_{\text{eff}} = 2\,\omega(0, \pi/2)/\pi$ (Ref. [110]), and is shown in Fig. 6.16. According to magnetic susceptibility measurements [111], J_{eff} in the low-temperature phase is approximately 0.8 of the exchange in the disordered phase. Our results are in a good qualitative agreement with these data in the sense that an increase in charge order goes together with a decrease in J_{eff} [112]. However, a quantitative comparison cannot be made since in the experiment the ordering and, correspondingly, J_{eff}, are traced as a function of temperature for given other system parameters while we investigate the ordering at $T = 0$ as a function of the extended Hubbard repulsion V. Our calculation also agrees well with the analytical results of Refs. [99] and [113], where it was shown that the exchange rapidly decreases with increasing V. Quantitatively, at $V = 3, C = 0$ our results give $J_{\text{eff}} \approx 0.06$ while perturbation theory [99, 113] predicts $J_{\text{eff}} \approx 0.04$. Moreover, for $V = 1.3, C = 0.35$, which give a lattice distortion close to the value observed experimentally (see Fig. 6.8), the exchange parameter in Fig. 6.16 is about 67 meV which is very close to the experimental 60 meV observed in the inelastic neutron scattering measurements of Ref. [114].

The second range in the spin spectrum (Fig. 6.15), with $q_a = \pi$, shows only high-energy excitations at small V, but again an effective Heisenberg dispersion at large V. For small V the gap in the spin spectrum is very close to the charge gap, indicating

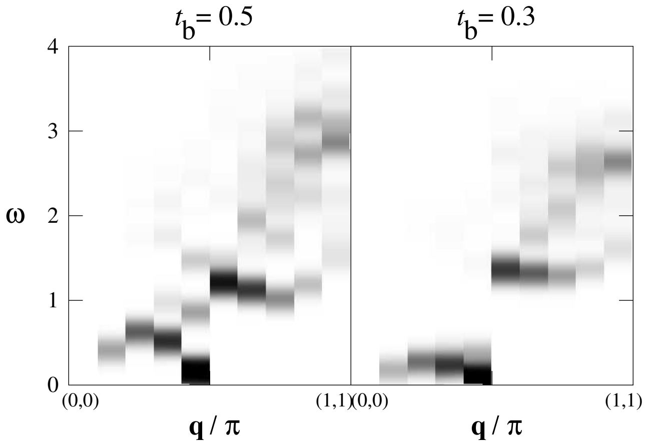

Figure 6.17.: Spin susceptibility in the disordered phase at $V = 0.5$ for hopping along the ladder $t_b = 0.5$ (left) and $t_b = 0.3$ (right). Momentum scan as in Fig. 6.13.

that it is due to charge excitations. To verify this conjecture, we calculated charge and spin susceptibilities in the non-interacting limit $V = 0$, with $t_b = 0$ (isolated rungs). In this case charge and spin susceptibilities are equal for $q_a = \pi$ and the gap is exactly the difference between the bonding and the anti-bonding state given by $2t_a$. Secondly, we analyzed the dependence of the spin susceptibility on the hopping t_b along the ladder in the disordered phase at $V = 0.5$ (Fig. 6.17). Whereas the dispersion for $q_a = 0$ scales as t_b^2, which is clear evidence of the magnetic origin of these excitations, the difference between the maximal and minimal excitation energy for $q_a = \pi$ scales as t_b. These observations show a direct interplay between the spin and the dipole-active charge excitations, which is similar to the "charged" magnons introduced in Ref. [115, 116] for interpretation of the infrared absorption spectra of NaV_2O_5.

It is interesting to note that the spin spectra in the ordered phase appear to possess a mirror symmetry with respect to the central tick mark in Fig. 6.15. To quantify this observation, the dispersions of the low energy excitations at $V = 3.0$ have been depicted in Fig. 6.18 The dispersions for $q_a = 0$ and $q_a = \pi$ are indeed very similar. Without lattice coupling the dispersion with $q_a = \pi$ is shifted upward compared to $q_a = 0$ because of the small but finite charge gap at $V = 3.0$ (see Fig. 6.14). With lattice coupling and at interactions where no charge gap occurs the agreement is even better. This behavior can be understood in the following way. In the disordered phase where each electron on a rung occupies a molecular orbital consisting of two sites, momenta $q = (0, \pi)$ and $q = (\pi, 0)$ are not equivalent (same spin on the two sites of the rung, versus opposite spin on two sites of neighboring rungs). In this phase pure spin excitations with $q_a = \pi$ are not possible since they require different spins on different sites within a rung. This could be achieved only by exciting another electronic state within the rung, which has the energy $2t_a$. In the totally zig-zag

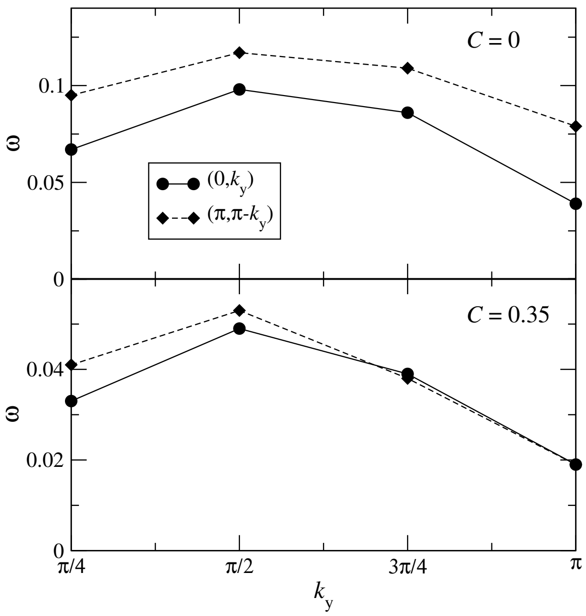

Figure 6.18.: Spin dispersion in the ordered phase at $V = 3.0$ extracted from Fig. 6.15. Bottom: with lattice coupling, top: without lattice coupling. Direction of momentum scans: Solid lines: $(0,0) \to (0,\pi)$, dashed lines: $(\pi,\pi) \to (\pi,0)$.

ordered state where the electrons are located on one site of the rung, these momenta become equivalent. The same holds for momenta $q = (0,0)$ and $q = (\pi,\pi)$.

The overall effect of charge ordering on the dynamical susceptibilities can best be seen by comparing the plots for $V = 2.5, C = 0.0$ and $V = 1.5, C = 0.35$, where the values of the order parameter are similar, see Fig. 6.7. The spin and charge excitations shown in these plots are qualitatively the same and the susceptibilities differ only slightly on a few points. From these figures we conclude that the dynamical spin and charge susceptibilities of the system mainly depend on the order parameter but not on the way in which the order has been achieved.

6.3.3. Hubbard-Holstein model

So far we have only considered static distortions of the lattice. Although this is a good approximation if the dynamic fluctuations around these equilibrium positions are small, quantum phonon effects can play an important role, especially in the critical region. In this section, we therefore consider the Extended Hubbard-Holstein model (EHHM)

$$H = H_{\mathrm{EHM}} + \sum_i \left[\frac{1}{2M}\hat{p}_i^2 + \frac{\kappa}{2}\hat{z}_i^2 - C\hat{z}_i n_i \right], \tag{6.9}$$

with H_{EHM} defined in Eq. (6.2a) and M being the mass of the local oscillators. The operators $\hat{z}_i$ and $\hat{p}_i$ are the coordinate and momentum of the ion on lattice site i, and all other quantities are defined in Eq. (6.1). When expressed in phonon creation and annihilation operators, it reads (up to a constant)

$$H = H_{\mathrm{EHM}} + \omega_0 \sum_i b_i^\dagger b_i - g \sum_i (b_i^\dagger + b_i) n_i. \tag{6.10}$$

Here $b_i^\dagger$ (b_i) creates (annihilates) a phonon of frequency ω_0 (with $\hbar = 1$) at lattice site i, and the phonons are locally coupled to the electron density with coupling strength $g = C\sqrt{\omega_0/2\kappa}$.

We would like to point out that the nature of the local phonon mode in Eq. (6.10) is not specified and could correspond to one of several phonon modes in the vanadates. Clearly, the use of dispersionless Einstein phonons neglects any coupling between lattice distortions of neighboring sites. However, a coupling of the Holstein type is the strongest phonon mode in $\mathrm{NaV_2O_5}$ [104]. It also represents the simplest model for electron-phonon interactions, and has been successfully used to describe the physics of other transition metal oxides such as the manganites [117].

Compared to exact diagonalization of the model described by the Hamiltonian in Eq. (6.1), an additional difficulty arises in the case of the EHHM since the number of phonons is not conserved. Consequently, even for a finite number of lattice sites, the Hilbert space contains an infinite number of states, and has to be truncated in some way in order to apply the Lanczos method. For this reason the size of the systems which can be investigated is also considerably reduced. We restricted ourselves to a lattice with four rungs and chose a subset of the phonon states as [118, 119]

$$|r\rangle_{\mathrm{ph}} = \prod_{i=1}^{N} \frac{1}{\sqrt{\nu_i^{(r)}!}} \left(b_i^\dagger\right)^{\nu_i^{(r)}} |0\rangle_{\mathrm{ph}}\,, \tag{6.11}$$

where $\nu_i^{(r)}$ denotes the number of phonons at lattice site i and $|0\rangle_{\mathrm{ph}}$ is the phonon vacuum state. Alternatively, the basis states could also be formulated in momentum space as in Ref. [118].

Now the truncation of the Hilbert space consists of restricting the total number of phonons in the $|r\rangle_{\mathrm{ph}}$ subset as:

$$\sum_{i=1}^{N} \nu_i^{(r)} \leq N_{\mathrm{ph}} \tag{6.12}$$

leading to $(N_{\mathrm{ph}}+N-1)!/(N_{\mathrm{ph}}!(N-1)!)$ allowed phonon configurations for N sites. We would like to point out that the set of basis states in Eqs. (6.11) and (6.12) consists of all possible phonon states with up to N_{ph} phonons excited. In particular, the Hilbert space includes all linear combinations of such states.

Usually, N_{ph} is increased until convergence of an observable of interest O is achieved. The latter can be monitored by calculating the relative error

$$\frac{|O(N_{\mathrm{ph}}+1)-O(N_{\mathrm{ph}})|}{|O(N_{\mathrm{ph}})|}.$$

Due to the complexity of the EHHM and the value of parameters, it is not possible to include enough phonon states to obtain converged results. Nevertheless, as in the case of the pure Holstein model [120] it is still possible to deduce the tendency of the results as N_{ph} is increased and thereby obtain information about the exact results (corresponding to $N_{\mathrm{ph}}=\infty$).

To reduce the required number of dynamical phonons, it is expedient to introduce static distortions z_i as a coordinate transformation $\hat{z}_i = z_i + \hat{x}_i$ so that quantum fluctuations $\hat{x}_i$ take place around the position z_i. Applying this transformation to Eq. (6.9) yields

$$\begin{aligned} H = H_{\mathrm{EHM}} &+ \sum_i \left[\frac{\kappa}{2} z_i^2 - C z_i n_i\right] \\ &+ \sum_i \left[\frac{1}{2M}\hat{p}_i^2 + \frac{\kappa}{2}\hat{x}_i^2 + (\kappa z_i - C n_i)\hat{x}_i\right], \end{aligned} \tag{6.13}$$

which in second quantization results in an expression analogous to Eq. (6.10). Note that the first line in the above equation is the same as Eq. (6.1). For the static distortions z_i we again use the zig-zag order pattern, Eq. (6.5), and determine the optimal value of z by minimizing the ground-state energy in the presence of phonons yielding a static distortion z_{stat}, which is related to z_{min} introduced in Sec. 6.3.1 by $z_{\mathrm{min}} = z_{\mathrm{stat}}(N_{\mathrm{ph}}=0)$.

Note that we perform this coordinate transformation only because the number of phonons accessible in our calculations is very small, and in this case it is better to start from a different equilibrium position $z = z_{\mathrm{stat}}$ and not from $z = 0$. If it were possible to use $N_{\mathrm{ph}}=\infty$, this coordinate transformation would have no influence on the physical results and the actual lattice distortions would be produced by the dynamical phonons as a coherent state of oscillators associated with the ions, independent of any initial coordinate transformation. Of course the broken symmetry would only occur in the thermodynamic limit, while correlations of the phonon positions exist already on finite lattices.

The effect of dynamical phonons on the charge order parameter is shown in Fig. 6.19. We did calculations for several values of V at phonon frequencies $\omega_0 = 60\,\mathrm{meV}$ and $\omega_0 = 125\,\mathrm{meV}$, the two most relevant modes in NaV$_2$O$_5$ [104]. The smaller frequency belongs to a collective vibration which includes displacements of the vanadium and oxygen ions, whereas the larger one corresponds to a vibration of the apical oxygen along the z axis. From the upper panel of Fig. 6.19 one can easily see that for the nontransformed coordinates (circles) the inclusion of dynamical phonons with

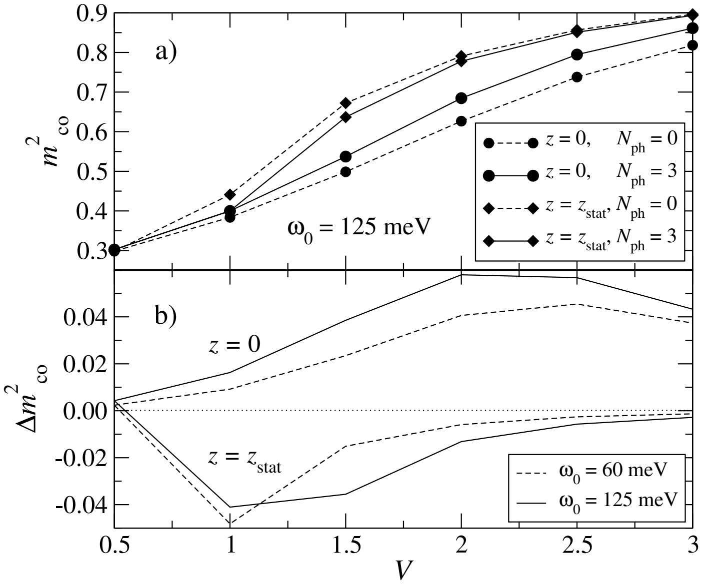

Figure 6.19.: a): Order parameter m^2_{CO}, calculated on a cluster with four rungs. Phonon parameters are $C = 0.35$, $\kappa = 0.125$, and $\omega_0 = 125\,\mathrm{meV}$. Parameters are chosen as shown in the caption. b): $\Delta m^2_{\mathrm{CO}} = m^2_{\mathrm{CO}}(N_{\mathrm{ph}} = 3) - m^2_{\mathrm{CO}}(N_{\mathrm{ph}} = 0)$ for two phonon frequencies $\omega_0 = 60\,\mathrm{meV}$ and $125\,\mathrm{meV}$. Upper two curves: Without static distortion. Lower two curves: with static distortion. The dotted line marks $\Delta m^2_{\mathrm{CO}} = 0$.

$\omega_0 = 125\,\mathrm{meV}$ considerably increases the charge order. Calculations with $N_{\mathrm{ph}} = 1$ and 2 (not shown) revealed that the increase is monotonic in the number of phonon states and we conclude that for convergence many more phonon states would be necessary. For the distorted lattice (diamonds), the dynamical phonons actually decrease the charge ordering for $V \geq 1.0$, and the strongest effect occurs in the vicinity of the phase transition at $V = 1.0$ and $V = 1.5$. The reason for this decrease is that z_{stat} is shifted downward with increasing number of dynamical phonons. At $V = 1.0$, where a finite z_{stat} at $N_{\mathrm{ph}} = 0$ is a finite size effect (Sec. 6.3.1), z_{stat} is reduced to zero for $N_{\mathrm{ph}} = 3$. At $V \geq 1.5$ the relative change in z_{stat} is similar to that in m^2_{CO} (Fig. 6.19). We want to mention that the two solid curves in the upper panel of Fig. 6.19 give an upper and a lower boundary for the actual value of the order parameter on the four rung lattice, since for $N_{\mathrm{ph}} \to \infty$ results for $z = 0$ and $z = z_{\mathrm{stat}}$ become equivalent, as discussed above.

In the lower panel of Fig. 6.19 the difference Δm^2_{CO} of the order parameter in the presence of dynamical phonons to $N_{\mathrm{ph}} = 0$ is shown including data for $\omega_0 = 60\,\mathrm{meV}$. For $z = 0$ (upper two curves) this deviation is positive and the effect is always larger for $\omega_0 = 125\,\mathrm{meV}$, which corresponds to a larger value of g. For $z = z_{\mathrm{stat}}$ (lower two curves) it is negative for $V \geq 1.0$. The crossing at $V = 1.0$ is due to the small finite

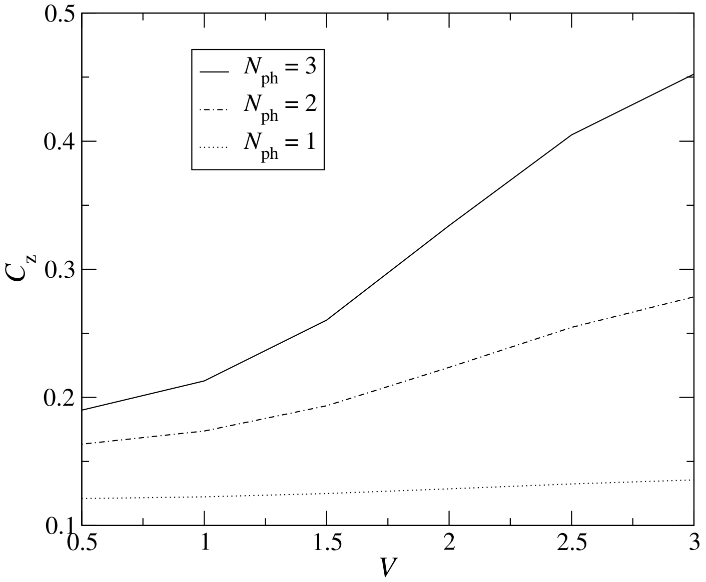

Figure 6.20.: Correlation function C_{z} as defined in Eq. (6.14) without static distortions for $\omega_0 = 125\,\text{meV}$. The number of phonons is given in the caption.

value of z_{stat} for $N_{\text{ph}} = 0$, i.e., a finite-size effect.

It is interesting to study the order pattern of the dynamically induced distortions. For this purpose we define the correlation function

$$C_{\text{z}} = \frac{1}{N^2} \sum_{ij} \mathrm{e}^{\mathrm{i}\boldsymbol{Q}(\boldsymbol{r}_i - \boldsymbol{r}_j)} \Big\langle \big(\hat{z}_i - \langle \hat{z}_i \rangle\big)\big(\hat{z}_j - \langle \hat{z}_j \rangle\big) \Big\rangle, \tag{6.14}$$

which measures the zig-zag ordering of the lattice distortions, similar to Eq. (6.4) for the charge densities. For the nontransformed coordinates it is depicted in Fig. 6.20 for $\omega_0 = 125\,\text{meV}$ and different numbers of dynamical phonons. From this figure it is clear that dynamical phonons induce zig-zag lattice distortions which strongly increase around the phase transition point. Note that the correlation function C_{z} is not normalized to the interval $[0, 1]$ since lattice distortions are not conserved quantities, different from, e.g., charges.

For the transformed coordinates we can calculate the dynamically induced zig-zag distortions z_{dyn} directly from the expectation values $\langle \hat{z}_i \rangle$ since the symmetry of the system is broken explicitly. Results show that the sum $z_{\text{tot}} = z_{\text{stat}} + z_{\text{dyn}}$ of the static distortion and the dynamically induced distortion is always smaller than the value z_{min} determined in section Sec. 6.3.1, and this effect is most pronounced near the phase transition. For $V = 1.5$ and $N_{\text{ph}} = 3$ we got $z_{\text{stat}} = 0.889$ and $z_{\text{dyn}} = 0.013$ yielding a total zig-zag distortion of $z_{\text{tot}} = 0.902$, which is noticeably smaller than $z_{\text{min}} = 1.001$ for $N_{\text{ph}} = 0$. Well above the transition point the dynamically induced distortions are very small, for instance for $V = 3.0$ and $N_{\text{ph}} = 3$ calculations gave

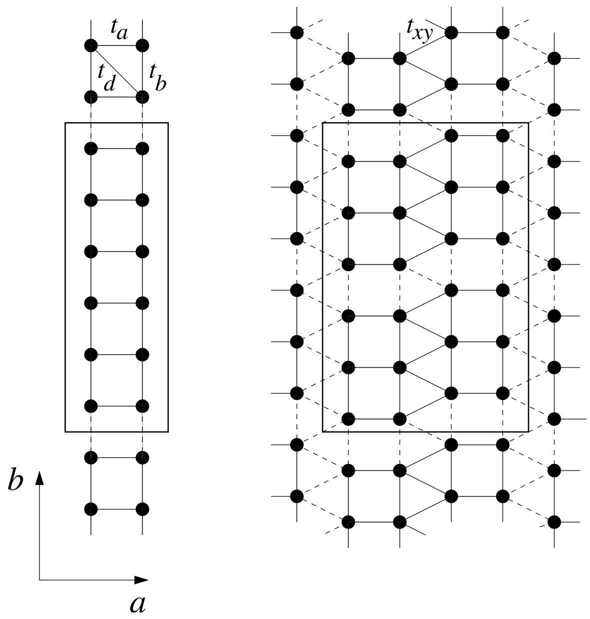

Figure 6.21.: Clusters used for the V-CPT calculations. The diagonal hopping t_d is indicated only once, but is present equivalently between other sites. Decoupled bonds treated perturbatively are marked by dashed lines, and the boxes show the clusters of finite size. Left: Single ladder with 6×2 cluster. Right: Super cluster consisting of two 12 sites clusters.

$z_{\mathrm{dyn}} = 0.0005$, and $z_{\mathrm{stat}} = 1.290$ is only slightly smaller than $z_{\mathrm{min}} = 1.294$.

From this analysis we conclude that using just static distortions gives qualitatively correct results but overestimates the lattice distortions, in particular in the vicinity of the phase transition. The value of the order parameter in the full dynamical model with $N_{\mathrm{ph}} = \infty$ will therefore be somewhat smaller than in Sec. 6.3.1, as discussed above.

6.4. Spectral properties of NaV_2O_5

So far all calculations have been done using the ground-state Lanczos method. In this section we study the single-particle properties of NaV_2O_5 by means of V-CPT [121]. Since the inclusion of nonlocal Coulomb interactions is of crucial importance in this compound, we have to apply the extension of V-CPT presented in Sec. 5.1.

In this section we do not only investigate single ladders but also the inter-ladder coupling. The clusters necessary for these studies are shown in Fig. 6.21. On the left hand side a cluster for single-ladder calculations is shown, consisting of $N_{\mathrm{rungs}} = 6$ rungs and $N_{\mathrm{c}} = 12$ sites, respectively. Of course the number of rungs can be varied, and we used up to eight rungs for the forthcoming calculations. The right plot shows the $N_c = 2 \times 12$ super cluster used for the investigation of the inter-ladder coupling. The super cluster has to be used, because otherwise the charge-order pattern would not fit into the clusters of finite size, similar to the super cluster used in Sec. 5.3. In addition the hopping parameters used in the Hamiltonian Eq. (6.1) are indicated in Fig. 6.21. The parameters t_a and t_b have already been introduced in the previous sections, and again we use t_a as the unit of energy. The additional hopping parameters t_d and t_{xy} will be discussed in the according sections.

Before turning to the results we want to mention a technical difficulty that arises in these calculations. Since calculations are not done at half filling, the chemical potential μ is not known a priori. Note that the Hamiltonian (6.1) does not include μ, different to the Hamiltonians used in the previous chapters. In general the chemical potential has to be determined from the self-consistent procedure described at the end of Sec. 2.2.1. However, here this cycle can be avoided. One can infer the chemical potential directly from the energies of the excited states obtained by exact diagonalisation. An approximate value for the chemical potential is then given by

$$\mu_{\mathrm{ED}} = \frac{E_{\mathrm{min}}^{\mathrm{IPES}} + E_{\mathrm{max}}^{\mathrm{PES}}}{2}, \tag{6.15}$$

with $E_{\mathrm{min}}^{\mathrm{IPES}}$ the minimal energy of inverse-photo-emission (IPES) states and $E_{\mathrm{max}}^{\mathrm{PES}}$ the maximum energy of photo-emission (PES) states. This value only weakly depends on the mean-field and variational parameters, and as discussed below we found in all our calculations a well established gap between the PES and IPES states yielding a constant density n in a reasonably large neighborhood of the physical chemical potential μ. Therefore μ_{ED} gives a reasonable approximation for our calculations.

6.4.1. Results for single ladders

Critical interaction

We start our investigations with decoupled ladders, i.e., $t_{xy} = 0$ and $V_{xy} = 0$ (see the left sketch of the lattice structure in Fig. 6.21). Before we turn to the spectral function, we study the charge-ordering transition as function of V. Since we apply a mean-field decoupling of the nonlocal Coulomb interactions across cluster boundaries as described in Sec. 5.1, we first study the effect of this approximation. For this purpose we treat the EHM without coupling to the lattice in the limit of exactly one electron per rung and $t_b = 0$, and the Coulomb interaction between different rungs is taken into account within the mean-field approximation. This consideration gives a second-order phase transition between a disordered state and a zig-zag ordered state at a critical interaction of $V_c^{\mathrm{MF}} = 1.0$. On the other hand this special limiting case is exactly solvable by a mapping to an Ising model in a transverse field [96], yielding a critical interaction of $V_c^{\mathrm{exact}} = 2.0$ [122–124]. That means that we expect strong mean-field effects, since in this special limit we found $V_c^{\mathrm{exact}} = 2V_c^{\mathrm{MF}}$. Since it can

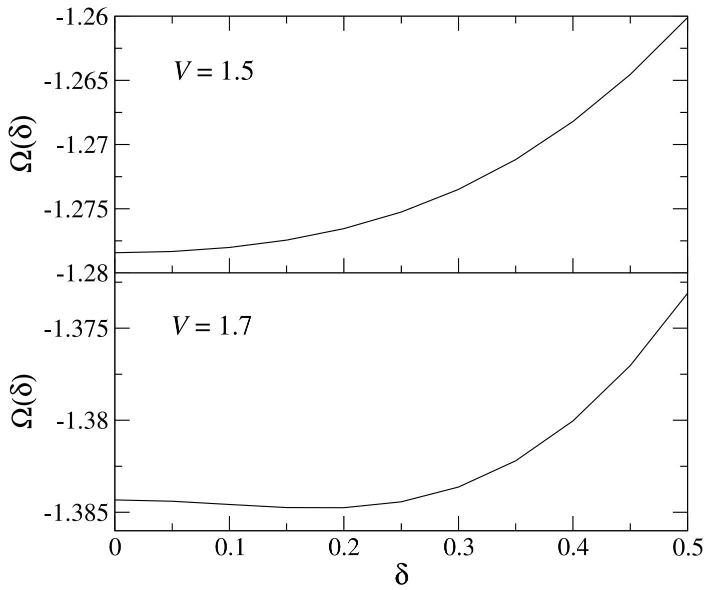

Figure 6.22.: Grand potential $\Omega(\delta)$ as function of mean-field parameter δ with a 6×2 cluster serving as reference system, and without coupling to the lattice. Upper panel: $V = 1.5$. Lower panel: $V = 1.7$.

be assumed that a finite value of the hopping between adjacent rungs t_b weakens the charge ordering, the actual critical value V_c is presumably located slightly above 2.0 when t_b is finite.

In order to determine the order of the transition within the framework of V-CPT it is sufficient to calculate the grand potential Ω, Eq. (2.15), as function of the mean-field parameters. Since our system is quarter filled we consider only one parameter δ giving mean-field electron densities $\langle n \rangle + \delta$ and $\langle n \rangle - \delta$ on sublattices A and B, respectively. It was argued in Sec. 5.2 that for second-order phase transitions it might be important to include a fictitious staggered chemical potential, Eq. (5.9), as variational parameter. Our calculations showed that in the present case the inclusion of such a field does not have any significant effect and the relative change in Ω is at most of the order of 10^{-4}. For this reason all further calculations are done without a staggered chemical potential.

We found that the spectral function is gapped around the chemical potential, which means that the frequency integrations, which are necessary for the evaluation of Ω do not strongly depend on μ.

Fig. 6.22 shows the dependence of $\Omega(\delta)$ on the mean-field parameter δ calculated with a 6×2 cluster as reference system, and the hopping parameter along the ladder was $t_b = 0.5$. One can easily see that the system undergoes a continuous phase transition, which is located between $V = 1.5$ and $V = 1.7$. For simplicity we set $V_a = V_b = V$. This value for the critical interaction is considerably smaller than the

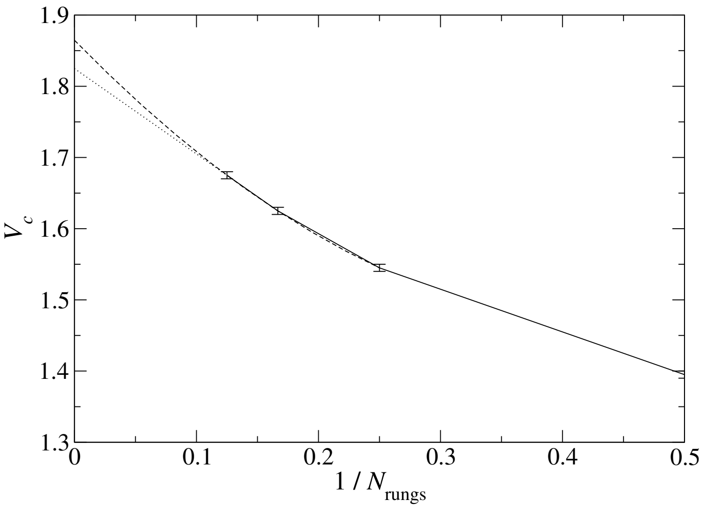

Figure 6.23.: Finite-size dependence of the critical Coulomb interaction V_c without lattice coupling. Error bars are due to the finite step $\Delta V = 0.01$ in the calculations. Dotted line: Linear extrapolation of the 8 and 6 rung cluster. Dashed line: Quadratic extrapolation of the 8, 6, and 4 rung cluster.

above mentioned value of the analytical solution, but the agreement is much better than the result of a purle mean-field consideration.

In order to study the finite size dependence of the critical Coulomb interaction we did calculations on clusters of different length, and the results are depicted in Fig. 6.23. The steps in V in our calculations were $\Delta V = 0.01$, which results in error bars of $\Delta V_\mathrm{c} = 0.005$. As expected V_c is too small for all considered cluster sizes, and it is strongly finite-size dependent. From Fig. 6.23 we can expect that for larger cluster sizes the critical interaction V_c increases further and reaches the assumed value of slightly above 2.0, but for a more sophisticated finite-size scaling our cluster sizes are too small. Nevertheless it is possible to study the spectral function both in the disordered and the ordered phase, although the critical Coulomb interaction is somewhat different from the value in the thermodynamical limit. Since the calculations for the 8×2 ladder are very time consuming, all single-ladder spectra presented in the following are determined with a 6×2 ladder as reference system.

Disordered phase

We start our investigations of the spectral function with the disordered high-temperature phase. Since the system is supposed to be near a quantum critical point between ordered and disordered phase, we choose the nearest-neighbor interaction to be slightly below the critical value. To be specific we set $V = V_a = V_b = 1.3$, $t_b = 0.5$.The result of this calculation is shown in Fig. 6.24. An additional Lorentzian broadening

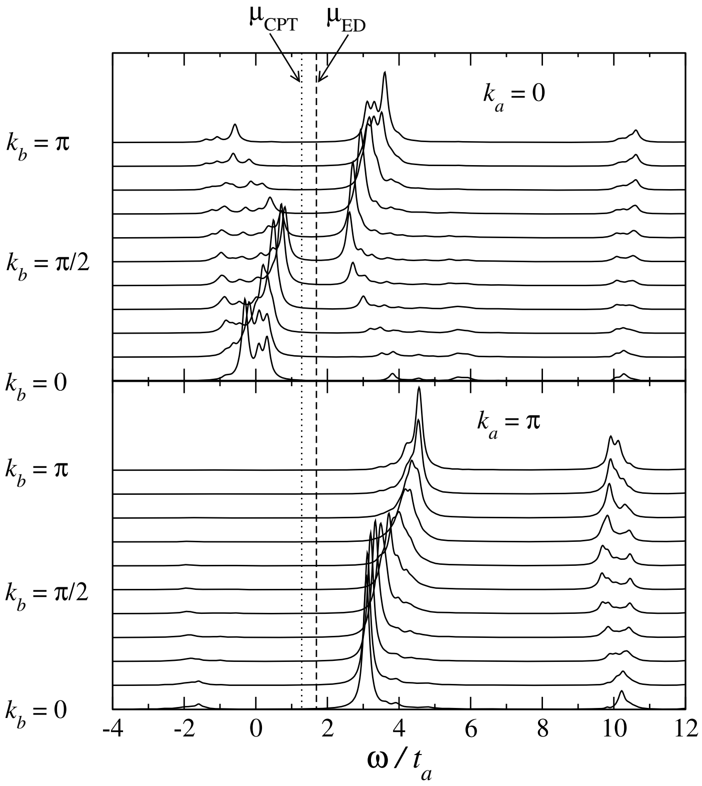

Figure 6.24.: Single-particle spectral function $A(\boldsymbol{k}, \omega)$ calculated on a 6×2 ladder in the disordered phase at $V_a = V_b = 1.3$. Top panel: Momentum $k_a = 0$ perpendicular to the ladder. Bottom panel: $k_a = \pi$. The dashed line marks the chemical potential calculated by Eq. (6.15), the dotted line marks the result obtained from Eq. (2.20).

of $\eta = 0.1$ is used for all spectra shown in this section. The dashed vertical line marks μ_{ED} calculated from Eq. (6.15), and the dotted line denotes μ_{CPT} determined from the condition Eq. (2.20). For the latter quantity the sum over momentum vectors had to consist of about 80 $\boldsymbol{k}$ vectors in order to get a well converged result. It is easy to see that $\mu_{\mathrm{ED}} = 1.71$ lies exactly in the middle of the gap, whereas $\mu_{\mathrm{CPT}} = 1.23$ is located at its lower boundary. But since there are no ingap states both values of μ give approximately the same average density n, and the ground-state energy $E_0 = \Omega + \mu N$ hardly depends on whether we use μ_{ED} or μ_{CPT}. These facts confirm that our approximation to use $\mu = \mu_{\mathrm{ED}}$ as chemical potential gives correct results, and in addition the numerical effort for this procedure is much less than for the above described self-consistent determination of μ.

As one can easily see in Fig. 6.24 the spectral function exhibits a well defined gap around the chemical potential, a clear indication of insulating behavior. In order to check if the insulator is only stable above some critical intersite Coulomb interaction,

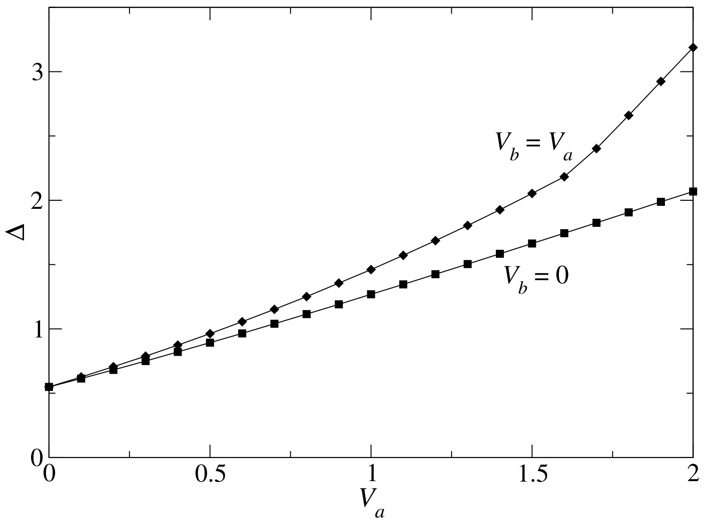

Figure 6.25.: Gap Δ in the spectral function as function of V_a. Squares: $V_b = 0$. Diamonds: $V_b = V_a$.

we calculated the gap Δ at $(k_a, k_b) = (0, \pi/2)$ as function of the intra-rung interaction V_a. We studied two cases with $V_b = 0$ and $V_b = V_a$, respectively, and the results are shown in Fig. 6.25. Note that for $V_b = 0$ no mean-field decoupling is needed, since there are no interaction bonds between different clusters. At $V_a = 0$, where both cases are equivalent, we found a finite value of the gap, $\Delta \approx 0.55$. We checked the finite size dependence by calculating the gap on a 4×2 cluster giving $\Delta \approx 0.59$. By applying a $1/N_{\text{rungs}}$ extrapolation to $N_{\text{rungs}} = \infty$ one gets $\Delta \approx 0.47$, indicating that the curves in Fig. 6.25 somewhat overestimates the value of the gap for the infinite ladder. Nevertheless we conclude from our calculations that the system is insulating already for small values of V_a. This is consistent with DMRG calculations [98–100], where for $t_a > t_b$ a homogeneous insulating phase is found for $V = 0$. The behavior of the spectral function is also in agreement with ED calculations on small clusters for $V = 0$, where for large enough t_a an insulating state has been found [103]. Similar results have been obtained by Kohno for the $U = \infty$ Hubbard ladder [125].

In the case $V_b = 0$, which means that there is no Coulomb interaction between adjacent rungs, we found that Δ increases linearly with V_a. For $V_b = V_a$ the gap is slightly larger and the deviation increases with increasing V_a. Here the system undergoes a phase transition at $V_c \approx 1.625$, which results in the kink in Δ around this critical value. Note that for $V_b = 0$ such a phase transition is not possible.

Let us now discuss the spectral features as shown in Fig. 6.24. For $k_a = 0$ the spectral function looks very similar to that of the half-filled one-dimensional Hubbard model with a totally filled lower and an empty upper Hubbard band. Different to the 1D Hubbard model the gap between these two bands is not determined by the onsite interaction U, but mainly by the intra-rung interaction V_a, as discussed above. At

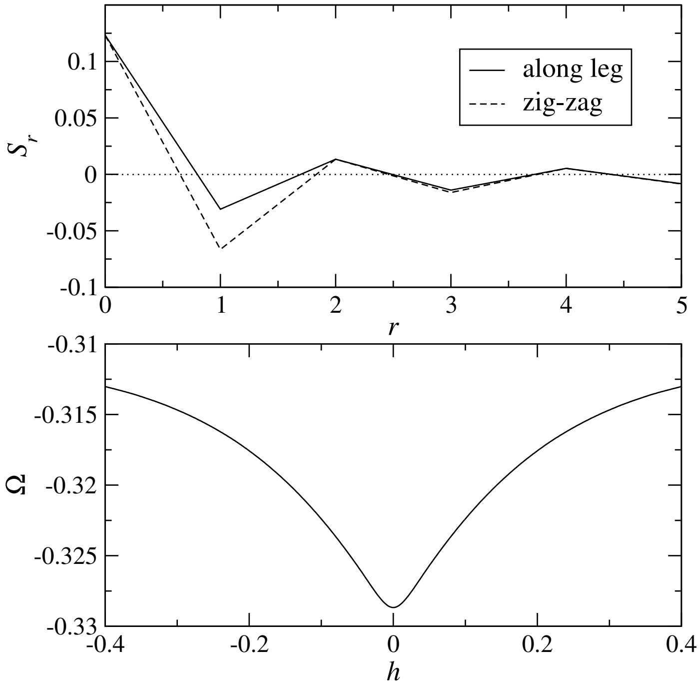

Figure 6.26.: Magnetic properties of a single ladder at $V_a = V_b = 1.3$. Upper panel: Spin correlation function $S_r = \langle S_1^z S_{1+r}^z \rangle$ calculated on an isolated 6×2 cluster. For the meaning of r see text. Lower panel: Grand potential Ω as function of the strength of the fictitious magnetic field Eq. (6.16).

$k_b = 0$ one can see signatures of spin-charge separation, where the band is split into a low energy spinon band (at approximately $\omega - \mu \approx -1.5$) and a holon band at slightly higher energy ($\omega - \mu \approx -2.0$). This splitting has not been seen in experiments [105], since they are very narrow in energy and temperature effects did not allow a high enough experimental resolution. However, by studying the temperature dependence of ARPES spectra, it was argued that subtle spectral-weight redistributions can be related to spin-charge separation [106]. Some spectral weight can be found at very high energies of about $(\omega - \mu) \approx 8.5$, which is close to the onsite energy $U = 8$ and can thus be related to doubly occupied sites.

As shown by LDA calculations [104], infrared (IR) experiments probe transitions near the Γ point, that is between even $(0, 0)$ and odd $(0, \pi)$ states in the language of single ladders. From Fig. 6.24 one can extract an excitation energy of roughly $3t_a$, which is in well agreement with the experimentally found 1 eV absorption peak [115, 126].

The lower and upper Hubbard band disperse with period π indicating a doubling of the unit cell in real space, similar to the 1D Hubbard model. In order to determine the origin of this doubling we calculate the real-space spin correlation function $S_r = \langle S_1^z S_{1+r}^z \rangle$ within the cluster by exact diagonalisation, where S_1^z and S_{1+r}^z are the z-

components of a spin on the cluster boundary and on a rung with distance r to the boundary. In the upper panel of Fig. 6.26 this correlation function is shown for two different paths, where the solid line is S_r along one leg of the ladder, and the dashed line is S_r on a zig-zag path through the ladder. Both correlation functions show clear antiferromagnetic correlations along the ladder similar to results obtained by the finite-temperature Lanczos method [34]. By applying a fictitious symmetry-breaking magnetic field via the operator $\mathcal{O}(\boldsymbol{R})$, Eq. (2.24), we can determine whether this order is of long range type or not. Similar to Eq. (4.2) we choose for this field

$$\Delta_{a,b} = h\delta_{a,b}z_\sigma \mathrm{e}^{\mathrm{i}\tilde{\boldsymbol{Q}}\boldsymbol{r}_a}, \tag{6.16}$$

where z_σ is ± 1 for spin projection $\uparrow, \downarrow$, h is the field strength, and $\boldsymbol{r}_a$ is the lattice vector of site a. The wave vector $\tilde{\boldsymbol{Q}}$ is set to $(0, \pi)$ yielding a staggered field along the ladder. The dependence of Ω on this fictitious field is depicted in the lower panel of Fig. 6.26. Similar to the one-dimensional Hubbard model at half filling discussed in Sec. 4.2, there is only one stationary point at $h = 0$, which means that the system does not show long-range antiferromagnetic order, but is rather in a paramagnetic state with short-range antiferromagnetic correlations.

The above considerations show that the system exhibits short-range antiferromagnetic spin correlations along the ladder, which can produce the doubled unit cell. Nevertheless it is also possible that the doubling of the unit cell is due to short-range charge correlations and not due to spin correlations. In order to clarify this point we calculated the spectral function at $V_b = 0$ and finite V_a, where no charge ordering is possible. Also in this case the periodicity of the bands with largest spectral weight was π at $k_a = 0$ and 2π at $k_a = \pi$. This shows that the doubling of the unit cell is mainly due to short-range spin correlations, and charge correlations play only a minor role in this context.

When turning to $k_a = \pi$ the spectral function looks totally different. As on can easily see in Fig. 6.24 there is hardly any spectral weight below the chemical potential, which means that there are no occupied states in the channel $k_a = \pi$. This can be understood, because $k_a = \pi$ corresponds to a antibonding state within a rung, which has energy $2t_a$ relative to the bonding orbital and is therefore not populated in the ground state.

An obvious difference between the spectra for $k_a = 0$ and $k_a = \pi$ is that in the latter case the excitations with largest spectral weight located between $\omega \approx 3$ and $\omega \approx 4.5$ disperse with periodicity 2π instead of π. Qualitatively this can be understood as follows. When inserting a particle with $k_a = 0$, this electron will occupy a state in the bonding orbital. Since one of the two states in this orbital is already occupied, the additional particle must have opposite spin, and thus this particle is connected to the antiferromagnetic background. A particle with $k_a = \pi$ occupies a state in the antibonding orbital, and since this orbital is not occupied, both spin directions are of equal possibility. Therefore an electron with $k_a = \pi$ is not influenced by the antiferromagnetism in the ground state.

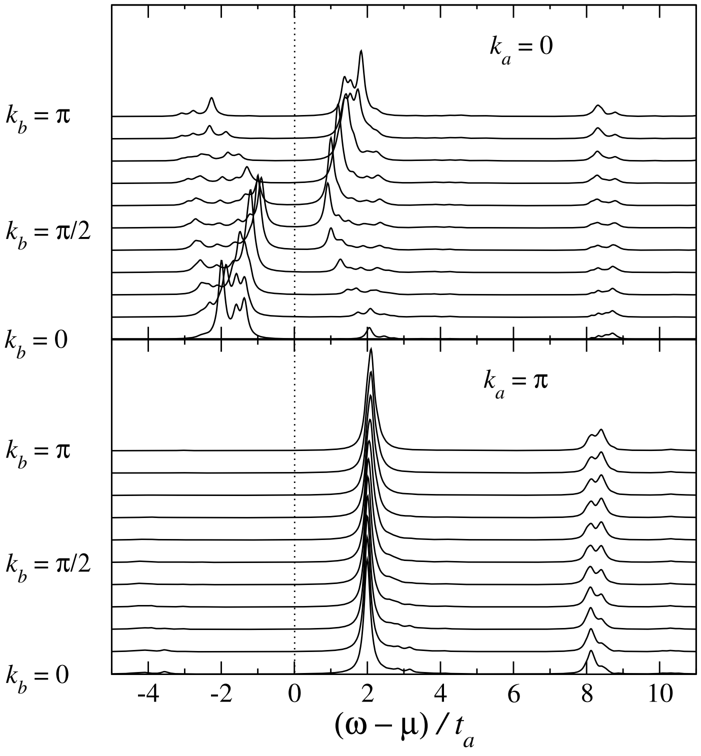

Figure 6.27.: Spectral function $A(\boldsymbol{k}, \omega)$ when the diagonal hopping is included, $t_b = 0.25$, $t_d = 0.25$. The Coulomb interaction was $V_a = V_b = 1.3$. The dotted line marks the chemical potential.

Disordered phase including diagonal hopping

So far we studied single ladders only with hopping parameters t_a and t_b and neglected additional hopping processes. By including the additional hopping term t_d in a massive downfolding procedure Mazurenko *et al.* [127] found $t_a \approx 0.38\,\mathrm{eV}$, which is consistent with the value given in Sec. 6.2, but the values $t_b = 0.084$ and $t_d = 0.083$ differ considerably from previous studies. These hopping processes were important in first-principle calculations in order to fit the LDA bands correctly [128]. Moreover t_d was important in C-DMFT calculations in order to describe the insulating state in the disordered phase correctly [127]. In this section we study the effect of t_d within the V-CPT framework.

In Fig. 6.27 the spectral function is shown for $V_a = V_b = 1.3$, $t_b = 0.25$ and $t_d = 0.25$, where the hopping parameters are chosen similarly to Ref. [127]. Whereas the spectrum at $k_a = 0$ is almost indistinguishable from Fig. 6.24, we see a big difference at $k_a = \pi$. There is still hardly any spectral weight below the Fermi energy, but the band with largest spectral weight above the Fermi level is now located at approximately $\omega - \mu \approx 2.0$ and is almost dispersionless.

From a qualitative point of view this can be explained by the dispersion of non-interacting fermions on a two-leg ladder in the presence of diagonal hopping, which is given by

$$\begin{aligned}\varepsilon(\boldsymbol{k}) = &- t_a \cos k_a - 2t_b \cos k_b \\ &- 2t_d \cos k_a \cos k_b,\end{aligned} \tag{6.17}$$

where the values for k_a are restricted to 0 and π, and in these two cases the dispersion can be written explicitly as

$$\begin{aligned}\varepsilon(k_a = 0, k_b) &= -t_a - 2(t_b + t_d)\cos k_b \\ \varepsilon(k_a = \pi, k_b) &= +t_a - 2(t_b - t_d)\cos k_b.\end{aligned}$$

This means that for $k_a = 0$ the bandwidth is determined by the sum of t_b and t_d, whereas for $k_a = \pi$ it is set by the difference of these two hopping processes. Since we used $t_b = t_d = 0.25$, this fits perfectly to the spectrum shown in Fig. 6.27. The sum is equal to the value of t_b used for the calculations without diagonal hopping (see above), and the difference is equal to zero, which explains the dispersionless band at $k_a = \pi$.

The picture that evolves from our calculations is somewhat different to that obtained in first-principle and C-DMFT calculations. To begin with the bands obtained from the LDA all disperse with periodicity 2π and not π along the b direction, as observed experimentally. Moreover we could not find any signature of a flattening of the upper d_{xy} bands in the direction $\boldsymbol{k} = (0,0) \rightarrow (0,\pi)$ when a diagonal hopping is included. The main difference of our calculations to C-DMFT results is that C-DMFT finds a metal-insulator transition at some finite value of V, and this transition point is shifted downward significantly when t_d is included [127]. In contrast we find an insulating state at reasonable values of U already for $V = 0$ consistent with DMRG calculations, which does not depend on the inclusion of t_d. The discrepancy to C-DMFT calculations are very likely due to the fact, that the cluster used in the C-DMFT calculations consisted only of a single rung, and fluctuations along the ladders, which seem to be very important in this system, have been neglected altogether.

Ordered phase

In the previous sections we studied the spectral function only in the disordered phase. Now we turn our attention to the charge-ordered low-temperature phase. Similar to the calculations in Sec. 6.3 we cannot describe the charge-ordering transition as function of temperature, because some very subtle effects are not included in our simple model Hamiltonian, Eq. (6.1). Similar to Sec. 6.3 we investigate two different driving forces for the occurrence of a charge-order pattern, (i) the coupling of the electrons to lattice degrees of freedom, and (ii) nearest-neighbor Coulomb interaction.

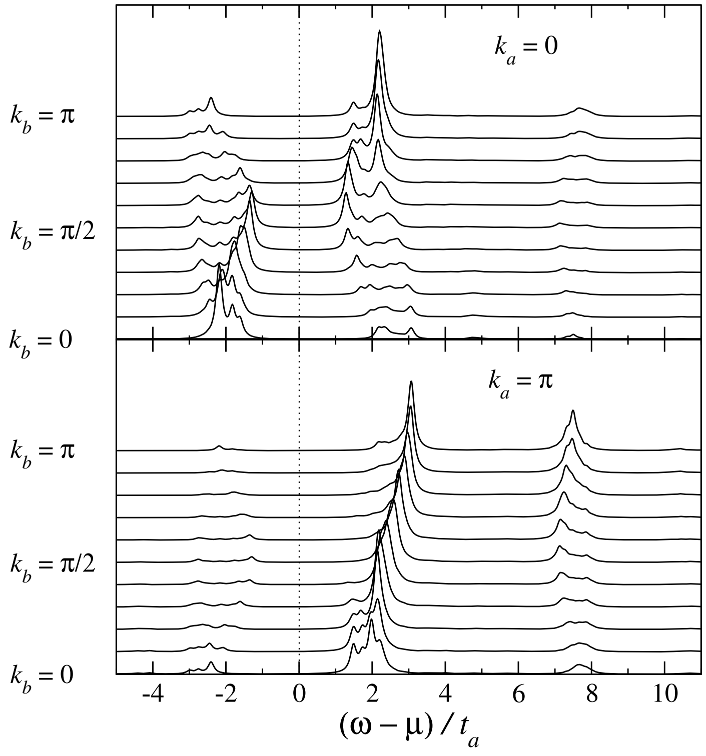

Figure 6.28.: Spectral function $A(\boldsymbol{k}, \omega)$ in the ordered phase driven by coupling to the lattice. The Coulomb interaction was $V_a = V_b = 1.3$. The dotted line marks the chemical potential.

Let us start our investigations with possibility (i), the coupling to the lattice. In order to keep the calculations simple, we consider only static lattice distortions. The incorporation of dynamical phonon effects would results in an infinitely large Hilbert space, similar to Sec. 6.3.3. In order to get well converged results for the spectral function, many phonon states are necessary, and calculations could so far only be done for the polaron [129] and bipolaron problem [130].

A few words have to be mentioned about the determination of the static distortions z_i in the Hamiltonian Eq. (6.1). First we did not treat the distortions on different sites independently, but we assumed a zig-zag charge order pattern, Eq. (6.5). In Sec. 6.3 the optimal value of z was determined by the minimum in the total energy. Here we use a very similar approach, but instead of the total energy we use the SFA grand potential, Eq. (2.15). That means that the grand potential is now a function of two external parameters, the mean-field parameter δ and the static distortion z. The proper choice for these two parameters is given by the minimum of $\Omega(\delta, z)$ on the two-dimensional manifold. In order to keep the calculations simple and the number of independent variables low, we did not consider an additional variational parameter like a staggered chemical potential.

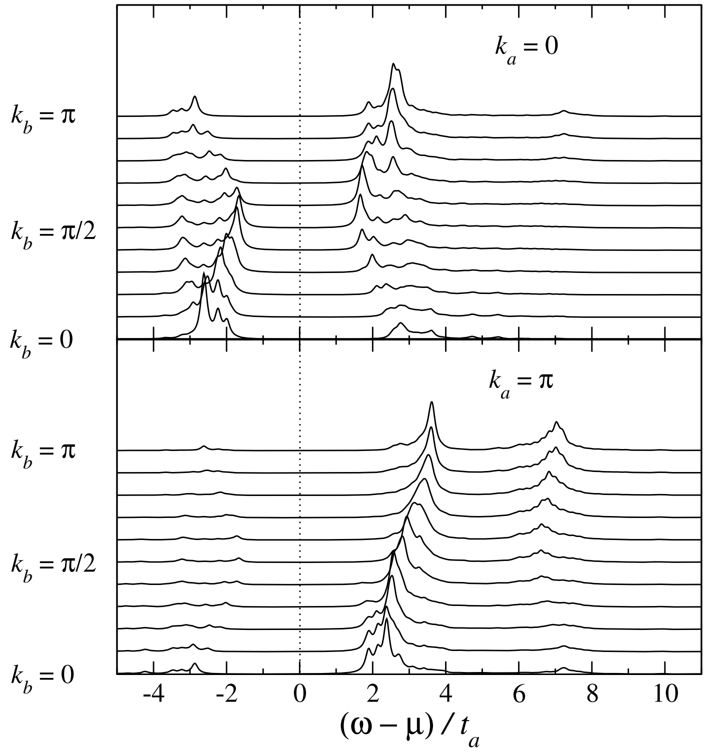

Figure 6.29.: Spectral function $A(\boldsymbol{k}, \omega)$ in the ordered phase driven by intersite Coulomb interaction, which was $V_a = V_b = 2.05$. The dotted line marks the chemical potential.

We set $V_a = V_b = 1.3$, since for this choice we expect the distortions to be close to the experimental value of $z_{\mathrm{exp}} \approx 0.95$, see Fig. 6.8. Indeed we found $z = 0.911$, which is close to z_{exp}, and the mean-field parameter was $\delta = 0.338$. The spectrum calculated with these values is shown in Fig. 6.28.

The spectral function shows similar features as in the undistorted phase. For $k_a = 0$ the bands disperse with periodicity π, whereas for $k_a = \pi$ no evidence for a doubling of the unit cell can be found, and the periodicity is 2π. Nevertheless, the gap at $\boldsymbol{k} = (0, \pi/2)$ is considerably larger than for $V = 1.3$ without distortions, see Fig. 6.24.

An interesting quantity when considering charge-ordering phenomena is the charge order parameter, which we calculate as

$$m_{\mathrm{CDW}} = \frac{1}{N_{\mathrm{c}} \langle n \rangle} \sum_j \left(n_j - \langle n \rangle \right) \mathrm{e}^{\mathrm{i} \boldsymbol{Q} \boldsymbol{r}_j}. \tag{6.18}$$

The above equation differs from Eq. (5.10) by the factor $\langle n \rangle$ in the denominator,which assures that the order parameter is normalized to the interval $[0, 1]$. For $V_a = V_b = 1.3$

and static distortions we got $m_{\mathrm{CDW}} = 0.65$, which means that the disproportion of charges is rather large.

Let us now consider possibility (ii), where the coupling to the lattice is switched off, $C = 0, \kappa = 0$, and the charge ordering is driven by the nearest-neighbor Coulomb interaction. In order to make a connection to the results obtained with lattice distortions, we calculate the spectral function at a similar value of the charge order parameter. We found that for $V_a = V_b = 2.05$ the order parameter is $m_{\mathrm{CDW}} = 0.66$, which is close to $m_{\mathrm{CDW}} = 0.65$, as given above.

The spectral function is shown in Fig. 6.29. The spectral features again look very similar to Fig. 6.24. One can see that in both cases, Fig. 6.28 and Fig. 6.29, the gap at $\boldsymbol{k} = (0, \pi/2)$ is larger than in the disordered phase, see Fig. 6.24. To be specific we found a gap size of approximately $2.6t_a$ in the presence of lattice distortions and $3.4t_a$ without lattice distortions, whereas in the disordered phase the gap was $1.8t_a$. It is interesting that the momentum-resolved spectral features do depend on the driving force of the transition, which was much less pronounced for, e.g., spin and charge susceptibilities.

The excitation energy near the Γ point, relevant for IR experiments, can be read off from Fig. 6.28 to be roughly $4t_a$ with lattice distortions and $5t_a$ without distortions. Although this excitation energies are not constant compared to the disordered phase, calculations including the lattice degrees of freedom give a better agreement to experimental IR absorption data [126], which show neither a shift of the 1 eV peak nor the appearance of new peaks related to electronic transitions.

6.4.2. Results for coupled ladders

So far we studied only single ladders and neglected the inter-ladder coupling, since they are frustrated and one might assume that they are only of minor importance. Nevertheless our approach allows to include these inter-ladder couplings by choosing an appropriate cluster geometry, as indicated at the right side of Fig. 6.21. Note that it is necessary to use a 2×12 super-cluster which allows for a commensurate charge-order pattern across the cluster boundaries.

The parameter values for the inter-cluster coupling were chosen in the following way. First-principle calculations [79, 104] have shown that the effective hopping between different ladders is very small, so we set $t_{xy} = 0.1t_a$, and longer-ranging hopping processes have been neglected since the linear dimensions of the cluster are rather small. The values for the other parameters were the same as used for the calculations in Sec. 6.4.1 (with $t_d = 0$).

In Fig. 6.30 the spectral function for $V_a = V_b = V_{xy} = 1.3$ is shown for to special paths trough the Brillouin zone. In the upper panel the momentum vector $\boldsymbol{k}$ is oriented parallel to the b axis, corresponding to momentum transfer in ladder direction, and in the lower panel $\boldsymbol{k}$ is parallel to the a direction.

For $\boldsymbol{k}$ parallel to the b axis one can easily see that the spectrum looks very similar

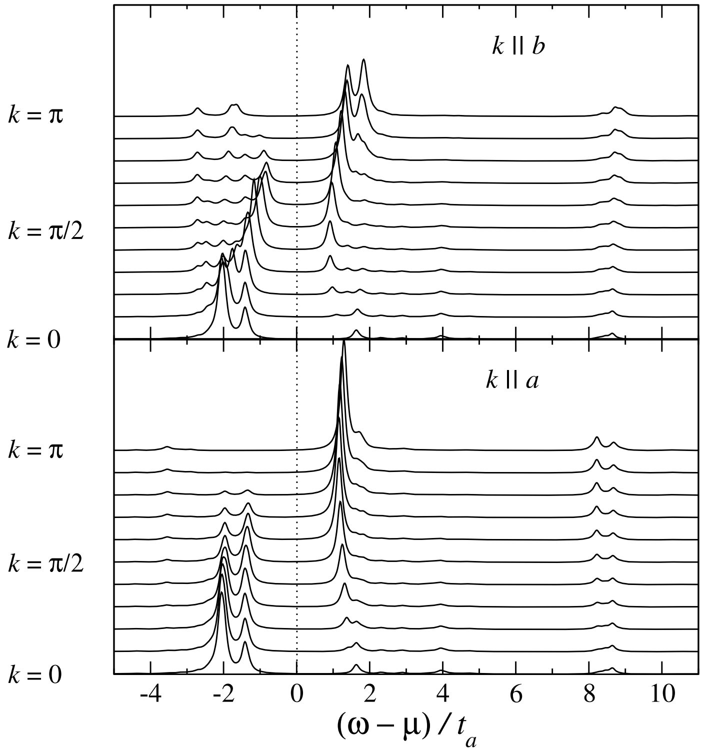

Figure 6.30.: Spectral function $A(\boldsymbol{k},\omega)$ in the disordered phase at $V_a = V_b = V_{xy} = 1.3$ calculated on the 2×12 super-cluster. Top: Momentum k along b direction. Bottom: k along a direction.

to the spectrum of a single ladder, see upper panel of Fig. 6.24. The main difference between single and coupled ladders is that the chemical potential is much larger in the latter case ($\mu \approx 3.0$), which is due to the frustrated inter-ladder bonds.

When turning to $\boldsymbol{k}$ parallel to the a axis the spectral function looks very different. The most striking feature is that there is hardly any dispersion of the bands, and the filled low-energy band can actually be considered as dispersionless. The spectral weight of this excitation, however, decreases significantly away from $k = 0$ and is obviously transfered to unoccupied states above the Fermi level at approximately $\omega - \mu \approx 1.5$.

Let us now compare our numerical results to experimental data. Kobayashi *et al.* [105] performed angle-resolved photo-emission spectroscopy (ARPES) at room temperature, where the system is in the disordered phase. They did measurements for momentum transfer along the a axis and the b axis, respectively, and for transfer parallel to a they found no dispersion of the V $3d$ bands, which fits perfectly well to our results. For k along the b axis a band dispersion of a 1D antiferromagnetic quantum system has been found with experimental band with of approximately 0.06–0.12 eV. This value is rather large compared to the band width in our calculation of approximately 0.35 eV, see Fig. 6.30. We checked that the band width scales with the hopping along the ladder t_b (not shown), and therefore this discrepancy between calculations and experiment can be shortened by choosing a smaller value for t_b, which does not significantly affect the charge ordering of the system. Nevertheless the strong difference between spectra along a and b direction are well described by our calculations.

7. Conclusions

Strongly-correlated electron systems show a variety of fascinating properties and rich phase diagrams, which arise due to the interplay of kinetic and interaction energy. Since these two energy scales are in general of the same order of magnitude, strong short-range correlations occur, accompanied by several competing long-range ordered phases. Since many standard methods known from theoretical solid-state physics fail for these systems, we further developed and applied cluster perturbation theory approaches, in order to study ordering phenomena in strongly-correlated systems.

Since the cluster perturbation theory proposed by Sénéchal *et al.* is a one-step method and is, thus, not based on a self-consistent procedure, it is not able to describe symmetry-broken phases. Nevertheless, it takes into account short-range correlations on the length scale of the clusters. On the other hand, the dynamical mean-field theory is a self-consistent method, but neglects spacial correlations altogether. For this reason, some intermediate approaches are the methods of choice for low-dimensional systems, where spatial correlations are supposed to be important.

In chapter 2 we introduced such an intermediate approach, which is termed variational cluster perturbation theory (V-CPT). It can be seen as a combination of the CPT and the self-energy-functional approach (SFA). In terms of the SFA the cluster of finite size serves as reference system, and the single-particle parameters of this system are determined by a general variational principle. We showed that such an optimization does indeed improve the results, although the changes between V-CPT and CPT results decrease fast with increasing cluster size. In addition to the optimization of the intra-cluster single-particle parameters given by the original Hamiltonian, one can introduce additional fictitious parameters, such as symmetry-breaking fields, which allows to construct very flexible cluster approaches.

The second part of chapter 2 dealt with the exact diagonalisation methods, which are used for the calculation of the finite cluster properties necessary for V-CPT. For the ground-state calculations the standard Lanczos algorithm has been used, and for finite temperatures we proposed a combination of the finite-temperature Lanczos method (FTLM) and the recently developed low-temperature Lanczos methods (LTLM). The latter methods is constructed for low temperatures, where the application of the FTLM is numerically very time-consuming, and it converges naturally to the ground-state method for zero temperature.

Chapter 3 gave a very short discussion of the application of the CPT to finite temperatures. By combining FTLM and LTLM we could calculate the spectral function of the Hubbard model in one and two dimensions with reasonable effort. The results for one dimension showed that the occurrence of the shadow bands, related to the doubling of the unit cell, disappears at a characteristic temperature equal to the magnetic super exchange, although the lower and upper Hubbard bands are still present.

In chapter 4 we applied the V-CPT to the Hubbard model at half filling to study the antiferromagnetic phase at zero temperature. The diagonalization of the clusters of finite size (typically $N_\mathrm{c} = 10$) was performed using the ground-state Lanczos algorithm. In comparison with results from variational Monte Carlo and quantum Monte Carlo studies, the V-CPT predicted the ground-state energy and related static quantities with high accuracy. While long-range antiferromagnetic order has been obtained for the 2D model, the V-CPT yielded a paramagnetic state for 1D. This indicates that quantum spin fluctuations which inhibit an ordered phase in the 1D case have been included properly. For one-dimensional Hubbard ladders the method in principle predicted incorrectly antiferromagnetic order; however, the staggered magnetization was small and tended to vanish when increasing the number of rungs in the cluster (up to 2×6). The finite but small m for the ladder system should be considered as a mild reminiscence of a typical mean-field artifact which shows up because longer-range spin correlations exceeding the cluster dimensions have been neglected. A similar effect was seen for the 2D system: Here the approximation was even stronger because the linear dimension of the cluster had to be reduced even more to keep the number of cluster sites N_c constant. For the 2D system, antiferromagnetic order is expected physically and has also been found in the calculations. However, longer-ranged spin correlations give rise to a considerable reduction of the order parameter which has not been seen in the V-CPT for the maximum cluster size that has been considered.

As mentioned above an important advantage of the V-CPT method is that local and off-site short-range correlations within the ordered phase can be treated exactly. This showed up when looking at dynamical quantities, such as the spin-dependent local density of states or the spectral function $A(\mathbf{k}, \omega)$. The spectral function calculated from our self-consistent cluster approach agreed extremely well with the QMC (maximum-entropy) result for an 8×8 Hubbard lattice at finite but low temperatures. In particular, it was possible to reproduce the dispersions, widths and weights of the different spectral features. This is due to the fact that the typical four-band structure arises not only from local correlations which are captured in dynamical mean-field theory, for example, but also from a strong coupling to off-site spin correlations. The formation of a spin-bag quasi-particle as a hole which is dressed by the distortions of the antiferromagnetic spin structure that are introduced due its motion, has been contained in the exact treatment of the cluster. In addition, the mean-field coupling of the individual clusters mediates the information on the spin order across the cluster boundaries and thereby gave a qualitatively correct description of the coherent propagation of the quasi particle. This was essential to reproduce the low-energy quasi-particle band in the spectrum.

A generalization of the V-CPT method to extended Hubbard models at half filling has been presented in chapter 5. For this purpose, a mean-field decoupling of the inter-cluster part of the nearest-neighbor Coulomb interaction was performed first. After this step, one is left with a Hamiltonian which couples the different clusters via the hopping only and which can be treated by the known V-CPT procedure. The mean-field decoupling yielded effective onsite potentials on the cluster boundaries as external parameters of the Hamiltonian. These parameters have been determined either self-consistently on an isolated cluster (sufficient for the study of first order phase transitions) or by determination of the minimum of the SFA grand potential.

In order to test the accuracy of our approach we applied the method to the extended Hubbard model in one dimension, because results from other methods like QMC and DMRG are available for comparison. At $U = 8$ the results for the critical interaction V_c, the ground-state energy, kinetic energy, and charge order parameter showed excellent quantitative agreement with previous QMC studies. At $U = 3$ our method predicted a second-order phase transition with transition point $V_c = 1.665(5)$ again in good agreement with previous studies. In addition we calculated the spectral function for several values of the interaction V, which has not been done previously. At both $U = 8$ and $U = 3$, we found evidence for spin-charge separation in the SDW phase, but not in the CDW phase. By fitting the bands by Hartree-Fock dispersions we found that the hopping parameter is strongly renormalized. The agreement between the fitted value of the gap and the value within the Hartree-Fock approximation was much better in the CDW phase than in the SDW phase giving rise to the conclusion that charge fluctuations play a minor role in the CDW phase.

Whereas the application of sophisticated methods like DMRG or fermionic loop-update QMC to more than one dimension is difficult, this extension is straightforward within the V-CPT approach. We found first-order transitions at both $U = 8$ and $U = 3$ with transition points $V_c = 2.023(1)$ and $V_c = 0.770(3)$ for an $N_c = 48$ super cluster, respectively. The spectral function in the SDW phase showed coherent low-energy quasi-particle excitations with band width set by the magnetic exchange constant J, and an incoherent background, consistent with previous QMC studies for the Hubbard model at $V = 0$. The Hartree-Fock prediction differed significantly from the low-energy feature and did not describe the splitting into coherent quasi-particle bands and incoherent background. In the CDW phase the Hartree-Fock dispersions accounted much better for the excitations, and no additional low-energy features caused by a magnetic origin could be found. Similar to one dimension the agreement between the Hartree-Fock approximation and the low-energy excitations obtained by the present method was much better in the CDW phase, confirming that charge fluctuations are less important in the charge-ordered phase than in the SDW phase.

The charge-ordering transition in the transition-metal compound NaV_2O_5 was subject of chapter 6. In the first part, Sec. 2.3, the influence of lattice effects on the charge-ordering transition, the spectrum of kink excitations and dynamical charge and spin susceptibilities of this quarter-filled ladder system have been studied by the ground-state Lanczos algorithm. For this purpose we modified the Hamiltonian of the extended Hubbard model by terms which take into account the coupling of electrons to lattice distortions. The lattice rigidity κ and the Holstein coupling constant C used in our model were determined by first-principles band-structure calculations. The results for the ground-state energy and the order parameter showed that by including static distortions, the phase transition is shifted significantly downward to lower values of the nearest-neighbor Coulomb interaction V. The calculated displacements of the vanadium ions due to the electron-lattice coupling in the charge-ordered phase were in good agreement with experimental measurements. We also found a virial theorem to be fulfilled to high precision for the terms in the Hamiltonian that couple to the lattice.

As low-energy excitations of the distorted ground state we considered kink excitations, where the charge-order pattern changes smoothly along the ladder between two degenerate configurations. These kinks are long when m_{CO}^2 is small, and become shorter with increasing order. The kink lengths and energies at small m_{CO}^2 were comparable with those of a classical ϕ^4 model.

Moreover, we studied the extended Hubbard-Holstein model to investigate the effect of dynamical phonons. Results showed that they have a strong influence on the charge order parameter in the vicinity of the phase transition. An analysis of the correlations of the dynamically induced distortions revealed that phonons indeed favor zig-zag lattice distortions. We showed that using just static distortions somewhat overestimates the actual value of the lattice distortion, but well away from the transition point this dynamical effect is very small and a description by static distortions gave already accurate results.

In addition to these static properties we also calculated the dynamic charge and spin susceptibilities. The main features of these quantities are determined by the value of the order parameter and not by the way this value is achieved. From the spin susceptibility we extracted the effective magnetic exchange interaction along the ladder, which exhibited a pronounced decrease with increasing charge order. The magnitude of this parameter taken at $V = 1.3, C = 0.35$ was in good agreement with the experimental inelastic neutron scattering data.

The second part of chapter 6, Sec. 6.4, dealt with the spectral features of $\mathrm{NaV_2O_5}$. For single ladders in the disordered high-temperature phase we found that in the channel $k_a = 0$ the system behaves like a one-dimensional antiferromagnetic insulator, and the gap is mainly determined by the nearest-neighbor Coulomb interaction on a rung. In addition our calculations suggested that the system is in an insulating phase for all values of V, and no metallic phase could be found.

This picture still holds, when a diagonal hopping t_d is included in the Hamiltonian, which was suggested to be important by LDA and C-DMFT studies. We could show that for $k_a = 0$ hardly any changes can be seen in the spectral function, whereas for $k_a = \pi$ the bands become flat. These findings do not agree with LDA considerations, where a finite value of t_d resulted in a flattening of the upper Hubbard band for $k_a = 0$, but on the other hand this LDA study was not able to describe the antiferromagnetic order along the ladder, and discrepancies are therefore not surprising.

For the transition into the charge-ordered low-temperature phase we again suggested two possible driving mechanisms, the coupling to the lattice and the nearest neighbor Coulomb interaction, similar to the first part of chapter 6. With lattice coupling we found that for $V = 1.3$ on all bonds the distortion is close to the experimentally found value, in agreement with the exact-diagonalisation study done in Sec. 6.3. The order parameter showed that the disproportion of charges is rather large in this regime. In order to get the same value of the order parameter by Coulomb interactions we had to use a rather large value of $V = 2.05$, which resulted in a large gap in the spectral function, considerably larger than in the disordered phase and in the ordered phase with lattice distortions. Therefore we suggest that for the description of the ordered phase lattice distortions cannot be neglected.

Within the V-CPT approach it was straightforward to study the effects of interladder coupling on the spectral function. We found that the spectra along ladder direction are not significantly affected by these couplings. Perpendicular to the ladders the calculated bands were almost dispersionless, in good agreement with experimental data.

Outlook

We have applied V-CPT for the investigation of several models for strongly-correlated sytems, but there are still some open ways to explore. First of all the problem of continuous filling, important for the investigation of, e.g., high-temperature superconductivity, has not been adressed in an accurate way. It is a task for the future to apply, and possibly modify, V-CPT in this context.

Our method is in general able to deal with any symmetry-broken ground state. Therefore it would be interesting to study other ordered phases, such as the superconducting phase, by means of V-CPT.

Last but not least the V-CPT can be used for many model Hamiltonians for realistic materials, from now on also for models including inter-site interactions. From the experimental point of view, many compounds are waiting for a proper theoretical understanding, and V-CPT can be a very powerful method for these purposes.

A. Strong-Coupling Perturbation Theory

In this section we briefly present the strong-coupling perturbation theory for the Hubbard model [131, 132], from which the (V-)CPT methods can be derived. Starting point is the formulation of the partition function using coherent states and Grassmann numbers yielding

$$Z = \mathrm{Tr}\, \mathrm{e}^{-\beta H} = \int \prod_{\alpha} \mathrm{d}\xi^*_\alpha \mathrm{d}\xi_\alpha \mathrm{e}^{-\sum_\alpha \xi^*_\alpha \xi_\alpha} \langle -\xi | \mathrm{e}^{-\beta(H-\mu N)} | \xi \rangle. \tag{A.1}$$

For convenience we set $\mu = 0$ in the following. Defining $\tau_f - \tau_i := \beta$ and introducing M Trotter time slices

$$\varepsilon = \frac{\tau_f - \tau_i}{M}$$

we can write for the matrix element in Eq. (A.1)

$$\begin{aligned} \langle -\xi | e^{-\beta H} | \xi \rangle &= \langle -\xi | e^{-\varepsilon H} e^{-\varepsilon H} \cdots e^{-\varepsilon H} | \xi \rangle \\ &= \langle -\xi | e^{-\varepsilon H} \mathbb{1} e^{-\varepsilon H} \mathbb{1} \cdots \mathbb{1} e^{-\varepsilon H} | \xi \rangle \end{aligned} \tag{A.2}$$

Using coherent states the unity operator in above equation can be written as

$$\mathbb{1} = \int \prod_{\alpha} \mathrm{d}\xi^*_\alpha \mathrm{d}\xi_\alpha e^{-\sum_\alpha \xi^*_\alpha \xi_\alpha} |\xi\rangle\langle\xi|.$$

Inserting this operator in Eq. (A.2) yields

$$\langle -\xi | e^{-\beta H} | \xi \rangle = \int \prod_{k=1}^{M-1} \prod_{\alpha} \mathrm{d}\xi^*_{\alpha,k} \mathrm{d}\xi_{\alpha,k} e^{-\sum_{k=1}^{M-1} \sum_\alpha \xi^*_\alpha \xi_\alpha} \prod_{k=1}^{M} \langle \xi_k | e^{-\varepsilon H} | \xi_{k-1} \rangle$$

Collecting all terms in the exponential and considering the boundary condition $\xi_{\alpha,0} = -\xi_{\alpha,M}$ we get after a short computation

$$Z = \int \prod_{k=1}^{M-1} \prod_{\alpha} \mathrm{d}\xi^*_{\alpha,k} \mathrm{d}\xi_{\alpha,k} \exp\left(S(\xi^*, \xi)\right)$$

with the action $S(\xi^*, \xi)$ given by

$$\begin{aligned} S(\xi^*, \xi) = -\varepsilon \sum_{k=2}^{M} & \left[\sum_{\alpha} \xi^*_{\alpha,k} \frac{\xi_{\alpha,k} - \xi_{\alpha,k-1}}{\varepsilon} + H(\xi^*_{\alpha,k}, \xi_{\alpha,k-1}) \right] \\ & - \varepsilon \left[\sum_{\alpha} \xi^*_{\alpha,1} \frac{\xi_{\alpha,1} + \xi_{\alpha,M}}{\varepsilon} + H(\xi^*_{\alpha,k}, -\xi_{\alpha,k-1}) \right] \end{aligned}$$

Defining trajectories $\xi(\tau)$ by interpolating the set $\{\xi_1, \ldots, \xi_M\}$, the action can also be written as

$$S(\xi^*, \xi) = -\int_0^\beta \mathrm{d}\tau \sum_\alpha \xi^*_\alpha(\tau) \left(\frac{\partial}{\partial \tau} - \mu \right) \xi_\alpha(\tau) + H\left(\xi^*_\alpha(\tau), \xi_\alpha(\tau) \right) \tag{A.3}$$

For completeness we inserted again the chemical potential μ. With this notation the partition function reads as

$$Z = \int\limits_{\xi_\alpha(\beta) = -\xi_\alpha(0)} \mathcal{D}\left[\xi^* \xi\right] e^{S(\xi^*, \xi)} \tag{A.4}$$

For the evaluation of the partition function Eq. (A.4) we split the Hamiltonian into two parts, $H = H_0 + H_1$, where H_0 is diagonal in a certain variable (for instance the site variable) and has the general form

$$H_0 = \sum_i h_i(c^\dagger_{i\sigma} c_{i\sigma}) = U c^\dagger_{i\uparrow} c_{i\uparrow} c^\dagger_{i\downarrow} c_{i\downarrow},$$

where the last term is the according expression for the Hubbard Hamiltonian. We suppose that the perturbation H_1 is a one-particle operator:

$$H_1 = \sum_{ij,\sigma} T_{ij} c^\dagger_{i\sigma} c_{j\sigma},$$

with T a Hermitian matrix. With this Hamiltonian the action Eq. (A.3) takes the form

$$\begin{aligned} S(\xi^*, \xi) = -\int_0^\beta \mathrm{d}\tau \Big[& \sum_a \xi^*_a(\tau) \left(\frac{\partial}{\partial \tau} - \mu \right) \xi_a(\tau) \\ & + \sum_i h_i\left(\xi^*_a(\tau), \xi_a(\tau) \right) + \sum_{ab} T_{ab} \xi^*_a(\tau) \xi_b(\tau) \Big]. \end{aligned} \tag{A.5}$$

From now on the indices a and b include site and spin indices, respectively. In order to lighten the notation we use the bra-ket notation

$$\int_0^\beta \mathrm{d}\tau \sum_{ab} T_{ab} \xi^*_a(\tau) \xi_b = \langle \xi | T | \xi \rangle.$$

Introducing auxiliary Grassmann fields $\psi_a^{(*)}(\tau)$ one can write the exponential of the perturbation as a result of a Gaussian integral over these auxiliary fields

$$\det(T^{-1})\mathrm{e}^{-\langle\xi|T|\xi\rangle} = \int \mathcal{D}\left[\psi^*\psi\right] \mathrm{e}^{\left[\langle\psi|T^{-1}|\psi\rangle+\langle\psi|\xi\rangle+\langle\xi|\psi\rangle\right]}$$

In terms of the auxiliary field the partition function becomes, up to a normalization factor:

$$Z = \int \mathcal{D}\left[\xi^*\xi\right] \mathcal{D}\left[\psi^*\psi\right] \exp\left\{-\int_0^\beta \mathrm{d}\tau \left[\sum_a \xi_a^*(\tau)(\partial_\tau - \mu)\xi_a + H_0\right]\right\}$$
$$\times \exp\left[\langle\psi|T^{-1}|\psi\rangle + \langle\psi|\xi\rangle + \langle\xi|\psi\rangle\right].$$

The first exponential involves only H_0, and therefore the path integral over the original Grassmann fields $\xi^{(*)}$ can be written as expectation value

$$Z = Z_0 \int \mathcal{D}\left[\psi^*\psi\right] e^{\langle\psi|T^{-1}|\psi\rangle} \left\langle e^{\langle\psi|\xi\rangle+\langle\xi|\psi\rangle}\right\rangle_0$$

where $\langle\cdot\rangle_0$ is the expectation value of the unperturbed Hamiltonian H_0 and Z_0 is the according partition function. This expectation value can be expanded in terms of Green's functions in the cluster calculated using the unperturbed Hamiltonian. Thus, the final form of the partition function reads as

$$Z \propto \int \mathcal{D}\left[\psi^*\psi\right] \exp\left\{-S_0(\psi^*,\psi) - \sum_{R=1}^{\infty} S_{\mathrm{int}}^R(\psi^*,\psi)\right\},$$

where the action has a free (Gaussian) part $S_0(\psi^*,\psi) = -\langle\psi|T^{-1}|\psi\rangle$ and an infinite number of interaction terms

$$S_{\mathrm{int}}^R(\psi^*,\psi) = \frac{-1}{(R!)^2} \sum_{\mu_l\nu_l} \psi_{\mu_1}\cdots\psi_{\mu_R}\psi_{\nu_R}^*\cdots\psi_{\nu_1}^* G^{(R)}_{\substack{\nu_1\cdots\nu_R \\ \mu_1\cdots\mu_r}}$$

where $G^{(R)}_{\substack{\nu_1\cdots\nu_R \\ \mu_1\cdots\mu_r}}$ is the R-particle Green's function. For more details and the derivation of diagrammatic rules see Ref. [132]. Standard CPT is now restricted to $R = 1$, the first non-trivial term in the perturbation expansion. In other words, the self energy of the auxiliary fermion field is equal to $G^{(1)}_{\nu\mu}$, the single-particle Green's function. The one-particle Green's function $\mathcal{G}$ of the original fermions is related to the self energy of the auxiliary fermions Ξ by the simple relation

$$\mathcal{G}^{-1} = \Xi^{-1} - T. \tag{A.6}$$

For $R = 1$ the self energy is given by only one term, $\Xi = G$, with G the one-particle Green's function in the cluster.

B. Causality of the SFA

This proof of causality closely follows the proof in Ref. [6]. For any $\boldsymbol{t}'$ the self-energy $\boldsymbol{\Sigma} = \boldsymbol{\Sigma}(\boldsymbol{t}')$ is causal since it is defined to be the exact self-energy of $H' = H_0(\boldsymbol{t}') + H_1(\boldsymbol{U})$. The same holds for $\boldsymbol{G}'$. Thus, causality problems could only be caused by the term

$$\mathrm{Tr}\ \ln(-(\boldsymbol{G}_0^{-1} - \boldsymbol{\Sigma}(\boldsymbol{t}'))^{-1}).$$

It has to be shown that $\boldsymbol{G} \equiv (\boldsymbol{G}_0^{-1} - \boldsymbol{\Sigma})^{-1}$ is causal provided that $\boldsymbol{\Sigma}(\boldsymbol{t}')$ and $\boldsymbol{G}_0$ are causal. Causality of $\boldsymbol{G}$ means that

(i) $G_{ij}(\omega)$ is analytical in the entire complex ω plane except of the real axis.

(ii) $\boldsymbol{G}_{\mathrm{ret}}(\omega) \equiv \boldsymbol{G}(\omega + \mathrm{i}0^+) = \boldsymbol{G}_{\mathrm{R}} - \mathrm{i}\boldsymbol{G}_{\mathrm{I}}$ for real ω with $\boldsymbol{G}_{\mathrm{R}}$ and $\boldsymbol{G}_{\mathrm{I}}$ Hermitian and $\boldsymbol{G}_{\mathrm{I}}$ positive definite.

Condition (i) is easily verified. To show (ii) we need the following Lemma: For Hermitian matrices $\boldsymbol{A}$, $\boldsymbol{B}$ with $\boldsymbol{B}$ positive definite, one has $(\boldsymbol{A} \pm \mathrm{i}\boldsymbol{B})^{-1} = \boldsymbol{X} \mp \mathrm{i}\boldsymbol{Y}$ with $\boldsymbol{Y}$ positive definite. Then, since $\boldsymbol{G}_0$ is causal, we have $\boldsymbol{G}_{0,\mathrm{ret}}^{-1} = \boldsymbol{P}_{\mathrm{r}} + \mathrm{i}\boldsymbol{P}_{\mathrm{I}}$ with P_{R}, P_{I} Hermitian and P_{I} positive definite. Since $\boldsymbol{\Sigma}$ is causal, $\boldsymbol{\Sigma}_{\mathrm{ret}} = \boldsymbol{\Sigma}_{\mathrm{R}} - \mathrm{i}\boldsymbol{\Sigma}_{\mathrm{I}}$ with $\boldsymbol{\Sigma}_{\mathrm{R}}$, $\boldsymbol{\Sigma}_{\mathrm{I}}$ Hermitian and $\boldsymbol{\Sigma}_{\mathrm{I}}$ positive definite. Therefore,

$$\boldsymbol{G}_{\mathrm{ret}} = (\boldsymbol{P}_{\mathrm{R}} + \mathrm{i}\boldsymbol{P}_{\mathrm{I}} - \boldsymbol{\Sigma}_{\mathrm{R}} + \mathrm{i}\boldsymbol{\Sigma}_{\mathrm{I}})^{-1} = (\boldsymbol{Q}_{\mathrm{R}} + \mathrm{i}\boldsymbol{Q}_{\mathrm{I}})^{-1},$$

with $\boldsymbol{Q}_{\mathrm{R}}$ Hermitian and $\boldsymbol{Q}_{\mathrm{I}}$ Hermitian and positive definite. Using the lemma once more shows $\boldsymbol{G}$ to be causal.

C. Mean-field Solution and Free Energy

In this section we show that a mean-field solution obtained self consistently is directly connected to a minimum in the free energy. For simplicity let us assume that we have only two different mean-field parameters $\lambda_A = 1 - \delta$ and $\lambda_B = 1 + \delta$, see also Sec. 5.1. We can write the mean-field decoupled Hamiltonian Eq. (5.8) as

$$H_{\mathrm{MF}}(\delta) = H_{\mathrm{MF}}^{(0)} + \sum_{\boldsymbol{R}} H_{\mathrm{MF}}^{(1)}(\boldsymbol{R}, \delta), \tag{C.1}$$

where $H_{\mathrm{MF}}^{(0)}$ includes all terms independent of the mean-field parameters. According to the third line in Eq. (5.5), $H_{\mathrm{MF}}^{(1)}(\boldsymbol{R}, \delta)$ is given by

$$\begin{aligned} H_{\mathrm{MF}}^{(1)}(\boldsymbol{R}, \delta) &= V \sum_{[ij]} \left[n_{\boldsymbol{R}i} \lambda_B + n_{\boldsymbol{R}j} \lambda_A - \lambda_A \lambda_B \right] \\ &= V \sum_{[ij]} \left[n_{\boldsymbol{R}i}(1+\delta) + n_{\boldsymbol{R}j}(1-\delta) - (1-\delta^2) \right] \end{aligned} \tag{C.2}$$

where we assumed without loss of generality that the bonds $[ij]$ connect sites i on sublattice A with sites j on sublattice B. The free energy of the system is given by

$$\begin{aligned} F &= -\frac{1}{\beta} \ln Z = -\frac{1}{\beta} \ln \operatorname{Tr} e^{-\beta H_{\mathrm{MF}}(\delta)} \\ &= -\frac{1}{\beta} \ln \operatorname{Tr} \exp \left[-\beta H_{\mathrm{MF}}^{(0)} - \beta \sum_{\boldsymbol{R}} H_{\mathrm{MF}}^{(1)}(\boldsymbol{R}, \delta) \right]. \end{aligned} \tag{C.3}$$

Taking the derivative with respect to δ yields

$$\frac{\partial F}{\partial \delta} = V \sum_{\boldsymbol{R}} \left\langle \sum_{[ij]} \left[n_{\boldsymbol{R}i} - n_{\boldsymbol{R}j} + 2\delta \right] \right\rangle. \tag{C.4}$$

All clusters are equivalent, therefore we suppress the index $\boldsymbol{R}$ in the following. Setting this derivative to zero we get the self-consistency condition

$$\sum_{[ij]} \left[\langle n_i \rangle - \langle n_j \rangle + 2\delta \right] = 0. \tag{C.5}$$

For one dimension, Eq. (C.5) is given by

$$\langle n_N \rangle - \langle n_1 \rangle = 2\delta, \tag{C.6}$$

because in this case we have only one decoupled bond $[1N]$ with site 1(N) belonging to sublattice $A(B)$, respectively. To conclude, one can state that if self consistency, Eq. (C.5), is fulfilled, then the free energy has an extremum with respect to the mean-field parameter δ. By thermodynamic stability arguments this extremum always has to be a minimum.

Bibliography

[1] E. H. Lieb and F. Y. Wu, Phys. Rev. Lett. **20**, 1445 (1968).

[2] M. Potthoff, M. Aichhorn, and C. Dahnken, Phys. Rev. Lett. **91**, 206402 (2003).

[3] D. Sénéchal, D. Perez, and M. Pioro-Ladrière, Phys. Rev. Lett. **84**, 522 (2000).

[4] D. Sénéchal, D. Perez, and D. Plouffe, Phys. Rev. B **66**, 075129 (2002).

[5] M. Potthoff, Eur. Phys. J. B **32**, 429 (2003).

[6] M. Potthoff, Eur. Phys. J. B **36**, 335 (2003).

[7] J. Jaklič and P. Prelovšek, Phys. Rev. B **49**, 5065 (1994).

[8] M. Aichhorn, M. Daghofer, H. G. Evertz, and W. von der Linden, Phys. Rev. B **67**, 161103R (2003).

[9] E. Dagotto, Rev. Mod. Phys. **66**, 763 (1994).

[10] S. R. White, Phys. Rev. Lett. **69**, 2863 (1992).

[11] S. R. White, Phys. Rev. B **48**, 10345 (1993).

[12] A. Georges, G. Kotliar, W. Krauth, and M. J. Rozenberg, Rev. Mod. Phys. **68**, 13 (1996).

[13] M. H. Hettler *et al.*, Phys. Rev. B **58**, 7475 (1998).

[14] G. Kotliar, S. Y. Savrasov, G. Palsson, and G. Biroli, Phys. Rev. Lett. **87**, 186401 (2001).

[15] G. Biroli and G. Kotliar, Phys. Rev. B **65**, 155112 (2002).

[16] C. J. Bolech, S. S. Kancharla, and G. Kotliar, Phys. Rev. B **67**, 075110 (2003).

[17] C. Gros and R. Valenti, Phys. Rev. B **48**, 418 (1993).

[18] M. G. Zacher, R. Eder, E. Arrigoni, and W. Hanke, Phys. Rev. Lett. **85**, 2585 (2000).

[19] M. G. Zacher, R. Eder, E. Arrigoni, and W. Hanke, Phys. Rev. B **65**, 045109 (2002).

[20] C. Dahnken, E. Arrigoni, and W. Hanke, J. of Low Temp. Phys. **126**, 949 (2002).

[21] D. Sénéchal and A.-M. S. Tremblay, Phys. Rev. Lett. **92**, 126401 (2004).

[22] J. M. Luttinger and J. C. Ward, Phys. Rev. **118**, 1417 (1960).

[23] J. E. Hirsch and R. M. Fye, Phys. Rev. Lett. **56**, 2521 (1986).

[24] C. Lanczos, J. Res. Nat. Bur. Stand. **45**, 255 (1950).

[25] G. D. Mahan, *Many-Particle Physics*, 3 ed. (Kluwer Academic/Plenum Publishers, New York, 2000).

[26] J. Jaklič and P. Prelovšek, Phys. Rev. Lett. **74**, 3411 (1995).

[27] J. Jaklič and P. Prelovšek, Phys. Rev. Lett. **75**, 1340 (1995).

[28] J. Jaklič and P. Prelovšek, Phys. Rev. Lett. **77**, 892 (1996).

[29] P. Prelovšek and A. Ramšak, Physica C **341**, 893 (2000).

[30] D. Veberič, P. Prelovšek, and H. G. Evertz, Phys. Rev. B **62**, 6745 (2000).

[31] Y. Shibata, T. Tohyana, and S. Maekawa, Phys. Rev. B **64**, 054519 (2001).

[32] D. Veberič and P. Prelovšek, Phys. Rev. B **66**, 020408 (2002).

[33] M. Cuoco, P. Horsch, and F. Mack, Phys. Rev. B **60**, R8438 (1999).

[34] M. Aichhorn, P. Horsch, W. von der Linden, and M. Cuoco, Phys. Rev. B **65**, 201101(R) (2002).

[35] P. Horsch, J. Jaklič, and F. Mack, Phys. Rev. B **59**, 6217 (1999).

[36] K. Haule, J. Bonča, and P. Prelovšek, Phys. Rev. B **61**, 2482 (2000).

[37] B. Schmidt, V. Yushankhai, L. Siurakshina, and P. Thalmeier, Eur. Phys. J. B **32**, 43047 (2003).

[38] C. S. Hellberg, J. Appl. Phys. **89**, 6627 (2001).

[39] A. C. Davidson and D. V. Hinkley, *Bootstrap Methods and their Application* (Cambridge University Press, ADDRESS, 1997).

[40] R. M. Fye *et al.*, Phys. Rev. B **44**, 6909 (1991).

[41] E. Jeckelmann, F. Gebhard, and F. H. L. Essler, Phys. Rev. Lett. **85**, 3910 (2000).

[42] N. D. Mermin and H. Wagner, Phys. Rev. Lett. **17**, 1133 (1966).

[43] C. Dahnken *et al.*, cond-mat/0309407 (unpublished).

[44] H. Yokoyama and H. Shiba, .

[45] J. E. Hirsch, Phys. Rev. B **31**, 6022 (1985).

[46] J. E. Hirsch and S. Tang, Phys. Rev. Lett. **62**, 591 (1989).

[47] P. W. Anderson, Phys. Rev. **86**, 694 (1952).

[48] P. W. Trivedi and D. M. Ceperley, Phys. Rev. B **40**, 2737 (1989).

[49] E. Manousakis, Rev. Mod. Phys. **63**, 1 (1991).

[50] R. Zitzler, T. Pruschke, and R. Bulla, Eur. Phys. J. B **27**, 473 (2002).

[51] T. Maier, M. Jarrell, T. Pruschke, and J. Keller, Eur. Phys. J. B **13**, 613 (2000).

[52] C. Gröber, R. Eder, and W. Hanke, Phys. Rev. B **62**, 4336 (2000).

[53] M. Aichhorn, H. G. Evertz, W. von der Linden, and M. Potthoff, cond-mat/0402580 (unpublished).

[54] P. Sengupta, A. W. Sandvik, and D. K. Campbell, Phys. Rev. B **65**, 155113 (2002).

[55] A. W. Sandvik, L. Balents, and D. K. Campbell, Phys. Rev. Lett. **92**, 236401 (2004).

[56] E. J. Hirsch, Phys. Rev. Lett. **53**, 2327 (1984).

[57] M. Nakamura, J. Phys. Soc. J. **68**, 3123 (1999).

[58] M. Nakamura, Phys. Rev. B **61**, 16377 (2000).

[59] M. Tsuchiizu and A. Furusaki, Phys. Rev. Lett. **88**, 056402 (2002).

[60] E. Jeckelmann, Phys. Rev. Lett. **89**, 236401 (2002).

[61] M. Tsuchiizu and A. Furusaki, Phys. Rev. B **69**, 035103 (2004).

[62] V. J. Emery, in *Highly Conducting One-Dimensional Solids*, edited by J. T. Devreese, R. Evrand, and V. van Doren (Plenum, New York, 1979).

[63] J. Sólyom, Adv. Phys. **28**, 201 (1979).

[64] R. A. Bari, Phys. Rev. B **3**, 2662 (1971).

[65] P. G. J. van Dongen, Phys. Rev. B **49**, 7904 (1994).

[66] J. W. Cannon and E. Fradkin, Phys. Rev. B **41**, 9435 (1990).

[67] J. Voit, Phys. Rev. B **45**, 4027 (1992).

[68] J. W. Cannon and E. Fradkin, Phys. Rev. B **44**, 5995 (1991).

[69] M. Nakamura and J. Voit, Phys. Rev. B **65**, 153110 (2002).

[70] Y. Z. Zhang, Phys. Rev. Lett. **92**, 246404 (2004).

[71] Y. Zhang and J. Callaway, Phys. Rev. B **39**, 9397 (1989).

[72] R. Micnas, J. Ranninger, S. Robaszkiewicz, and S. Tabor, Phys. Rev. B **37**, 9410 (1988).

[73] E. Dagotto *et al.*, Phys. Rev. B **49**, 3548 (1994).

[74] B. Chattopadhyay and D. M. Gaitonde, Phys. Rev. B **55**, 15364 (1997).

[75] S. Onari, R. Arita, K. Kuroki, and H. Aoki, cond-mat/0312314 (unpublished).

[76] R. P. W. Hanke and W. von der Linden, Phys. Rev. Lett. **75**, 1344 (1995).

[77] C. Gröber, M. G. Zacher, and R. Eder, cond-mat/9810246 (unpublished).

[78] E. J. W. Verwey, Nature **144**, 327 (1939).

[79] H. Smolinski *et al.*, Phys. Rev. Lett. **80**, 5164 (1998).

[80] A. Carpy and J. Galy, Acta Crystallogr., Sect. B: Struct. Crystallogr. Cryst. Chem. **31**, 1481 (1975).

[81] M. Isobe and Y. Ueda, J. Phys. Soc. Jpn. **65**, 1178 (1996).

[82] H. G. Schnering *et al.*, Z. Kristallogr. **213**, 246 (1998).

[83] A. Meetsma *et al.*, Acta Crystallogr., Sect. C: Cryst. Struct. Commun. **54**, 1558 (1998).

[84] P. Horsch and F. Mack, Eur. Phys. J. B **5**, 367 (1998).

[85] T. Ohama, H. Yasuoka, M. Isobe, and Y. Ueda, Phys. Rev. B **59**, 3299 (1999).

[86] M. N. Popova *et al.*, Phys. Rev. B **65**, 144303 (2002).

[87] E. Y. Sherman *et al.*, Europhys. Lett. **48**, 648 (1999).

[88] J. Lüdecke *et al.*, Phys. Rev. Lett. **82**, 3663 (1999).

[89] M. N. Popova *et al.*, Pis'ma Zh. Eksp. Teor. Fiz. **65**, 711 (1997).

[90] M. Fischer *et al.*, Phys. Rev. B **60**, 7284 (1999).

[91] J. Riera and A. Poilblanc, Phys. Rev. B **59**, 2667 (1999).

[92] R. T. Clay and S. Mazumdar, cond-mat/0305479 (unpublished).

[93] E. Y. Sherman *et al.*, Phys. Rev. B **63**, 224305 (2001).

[94] H. Seo and H. Fukuyama, J. Phys. Soc. J. **67**, 2602 (1998).

[95] P. Thalmeier and P. Fulde, Europhys. Lett. **44**, 242 (1998).

[96] M. V. Mostovoy and D. I. Khomskii, Solid State Commun. **113**, 159 (2000).

[97] M. V. Mostovoy, D. I. Khomskii, and J. Knoester, Phys. Rev. B **65**, 064412 (2002).

[98] M. Vojta, R. E. Hetzel, and R. M. Noack, Phys. Rev. B **60**, R8417 (1999).

[99] M. Vojta, A. Hübsch, and R. M. Noack, Phys. Rev. B **63**, 045105 (2001).

[100] R. M. Noack, S. R. White, and D. J. Scalapino, Physica C **270**, 281 (1996).

[101] E. Orignac and R. Citro, Eur. Phys. J. B **33**, 419 (2003).

[102] A. Hübsch, C. Waidacher, K. W. Becker, and W. von der Linden, Phys. Rev. B **64**, 075107 (2001).

[103] J. Riera, D. Poilblanc, and E. Dagotto, Eur. Phys. J. B **7**, 53 (1999).

[104] J. Spitaler, E. Y. Sherman, C. Ambrosch-Draxl, and H. G. Evertz, Physica Scripta **T109**, 159 (2004).

[105] K. Kobayashi *et al.*, Phys. Rev. Lett. **80**, 3121 (1998).

[106] K. Kobayashi *et al.*, Phys. Rev. Lett. **82**, 803 (1999).

[107] M. Aichhorn *et al.*, Phys. Rev. B **69**, 245108 (2004).

[108] E. I. Rashba, in *Excitons*, edited by E. I. Rashba and M. D. Sturge (North-Holland, Amsterdam, 1982).

[109] K. Okunishi and N. Maeshima, Phys. Rev. B **64**, 212406 (2001).

[110] J. des Cloizeaux and J. J. Pearson, Phys. Rev. **128**, 2131 (1962).

[111] M. Weiden *et al.*, Z. Phys. B: Condens. Matter **103**, 1 (1997).

[112] C. Gros and R. Valenti, Phys. Rev. Lett. **82**, 976 (1999).

[113] A. Hübsch, M. Vojta, and K. W. Becker, J. Phys.: Condens. Matter **11**, 8523 (1999).

[114] B. Grenier *et al.*, Phys. Rev. Lett. **86**, 5966 (2001).

[115] A. Damscelli *et al.*, Phys. Rev. Lett. **81**, 918 (1998).

[116] A. Damscelli *et al.*, Phys. Rev. B **61**, 2535 (2000).

[117] D. M. Edwards, Adv. Phys. **51**, 1259 (2002).

[118] F. Marsiglio, Phys. Lett. A **180**, 280 (1993).

[119] G. Wellein, H. Röder, and H. Fehske, Phys. Rev. B **53**, 9666 (1996).

[120] F. Marsiglio, Physica C **244**, 21 (1995).

[121] M. Aichhorn, E. Y. Sherman, and H. G. Evertz, cond-mat/0409162 (unpublished).

[122] E. Lieb, T. Schultz and D. Mattis, Ann. Phys. **16**, 407 (1961).

[123] T. H. Niemeijer, Physica **36**, 377 (1967).

[124] P. Pfeuty, Ann. Phys. **57**, 79 (1970).

[125] M. Kohno, Phys. Rev. B **56**, 15015 (1997).

[126] C. Presura, D. van der Marel, A. Damscelli and R. K. Kremer, Phys. Rev. B **61**, 15762 (2000).

[127] V. V. Mazurenko *et al.*, Phys. Rev. B **66**, 081104 (2002).

[128] A. N. Yaresko *et al.*, Phys. Rev. B **62**, 15538 (2000).

[129] M. Hohenadler, M. Aichhorn, and W. von der Linden, Phys. Rev. B **68**, 184304 (2003).

[130] M. Hohenadler, M. Aichhorn, and W. von der Linden, cond-mat/0405391 (unpublished).

[131] S. Pairault, D. Sénéchal, and A. M. S. Tremblay, Phys. Rev. Lett. **80**, 5389 (1998).

[132] S. Pairault, D. Sénéchal, and A. M. S. Tremblay, Eur. Phys. J. B **16**, 85 (2000).

Acknowledgments

A lot of time has gone by, since Prof. von der Linden gave me a four-pages paper on cluster perturbation theory and asked me if I want to work on this subject. In an instant I was fascinated by this simple and even so powerful method, so most times working on this PhD project was nothing but a pleasure. However, sometimes it was simply back-breaking work, but since there were lots of people who supported and encouraged me in my studies, it was easy to keep my spirits up.

First of all I want to thank my supervisor, Dr. Wolfgang von der Linden, who had the idea for this project. There were many fruitful discussions and suggestions that helped me when I did not see the wood for the trees. I am also grateful to Dr. Ewald Schachinger, who made the theoretical background of strong-coupling perturbation theory plain to me. And even more important were the very constructive comments on my scholarship proposal.

A big thanks goes to all the people at the Institute of Theoretical Physics and Astrophysics at the University of Würzburg, who managed to give a taste of holidays to all my visits there. Above all I want to mention Dr. Michael Potthoff, Dipl.-Phys. Christopher Dahnken, and Dr. Enrico Arrigoni for many discussions and practical hints. Without Michael and his SFA, all this V-CPT stuff would not be as nice as it is right now.

Particularly noteworthy is the research group for strongly-correlated many-body systems at the Institute for Theoretical and Computational Physics at the TU Graz. The group members Dipl.-Ing. Maria Daghofer, Dipl.-Ing. Franz Michel, Thomas Lang, Dipl.-Ing. Bernhard Edegger, Dipl.-Ing. Danilo Neuber, and my 'room mate' Dipl.-Ing. Martin Hohenadler made working in Graz a great pleasure. In particular I want to thank Dr. Hans Gerd Evertz and Dr. Eugene Sherman for the excellent working atmosphere and the interesting discussions on the vanadate compounds.

I am grateful to the Austrian Academy of Sciences who supported my PhD project by DOC, the doctoral scholarship program, and to the Fund for Scientific Research (FWF), projects No. P15834 and P15520, for financial support.

At last I want to thank my parents for giving me the possibility to make my own mistakes.

And most important, the biggest thanks of all to Julia. This is for you.

Typeset by $\LaTeX\,2_\varepsilon$, the **KOMA**-script and
$\mathcal{A}\!\mathcal{M}\!\mathcal{S}$-TeX the TeX macro system of the American Mathematical Society.